Novel Metrology Techniques Resolve Strong-Field-Driven Electron Dynamics in Solids

Sabine Keiber

München 2016

Novel Metrology Techniques Resolve Strong-Field-Driven Electron Dynamics in Solids

Sabine Keiber

Dissertation
an der Fakultät für Physik
der Ludwig–Maximilians–Universität
München

vorgelegt von
Sabine Keiber
aus Landau in der Pfalz

München, den 11. Mai 2016

Erstgutachter: Prof. Dr. Ferenc Krausz
Zweitgutachter: Prof. Dr. Alexander Holleitner
Tag der mündlichen Prüfung: 28. September 2016

Zusammenfassung

Laserpulse können die elektronischen Eigenschaften von Festkörpern auf der Zeitskala der optischen Feldzyklen beobachten und manipulieren [1]. Liegt die transiente, optische Feldstärke knapp unterhalb der Zerstörschwelle des Materials, so hängt die Polarisationsantwort des angeregten Systems nicht mehr von der Einhüllenden des Lichtpulses ab, sondern von den Schwingungsperioden des elektrischen Feldes. Potentiell kann diese schnelle, lichtgesteuerte Kontrolle der Ladungsträger für die Signalverarbeitung mit Frequenzen im Petahertz-Bereich (1×10^{15} Hz) genutzt werden [2]. Die präzise Anregung der elektronischen Systeme und die zeitaufgelöste Analyse ihrer Polarisationsantwort erfordern Messmethoden, die diese optischen Wellenformen charakterisieren können. Diese Anforderung stellt uns vor eine experimentelle Herausforderung: *Wie können wir Wellenformen messen, die zu den schnellsten, reproduzierbaren Signalen gehören, die uns im Labor zur Verfügung stehen?*

Diese Dissertation widmet sich der Verbesserung und Entwicklung neuer Messmethoden zur vollständigen Bestimmung des elektrischen Feldes kurzer Laserpulse und deren Anwendung zur Untersuchung starkfeldinduzierter Elektronendynamiken in Festkörpern.

Beim *elektro-optischen Abtasten* wechselwirkt die zu charakterisierende Test-Wellenform mit einem kurzen Abtastpuls in einem elektro-optischen Kristall. Dort wird die Polarisation des Abtastpulses proportional zur instantanen Feldstärke der Test-Wellenform gedreht. Variiert man den zeitlichen Abstand zwischen Abtast- und Testpuls, so können die elektrischen Feldoszillationen durch Detektion der zeitabhängigen Polarisationsdrehung aufgezeichnet werden [3]. Diese Arbeit zeigt, dass diese ursprünglich aus dem Terahertz-Bereich stammende Technik auch zur Auflösung von Frequenzen im nahen Infrarot bis zu 235 THz eingesetzt werden kann, was einer Wellenlänge von 1.27 µm entspricht. Somit wird elektro-optisches Abtasten auch für breitbandige optisch-parametrische Verstärker, sowie für Erbium-basierte Lasersysteme anwendbar, die im Wellenlängenbereich von 1.5 µm arbeiten. Eine erste Demonstration dieser Technik zeigt, wie Variationen in der Pump-Leistung zu starken Änderungen einer Wellenform während der optisch-parametrischen Verstärkung führen.

Des Weiteren werden in dieser Arbeit starkfeldinduzierte Ströme in Dielektrika untersucht [4]. Ein kurzer Laserpuls regt Ladungsträger ins Leitungsband an und beschleunigt sie dort. Die dabei entstehende Ladungstrennung führt zu einem messbaren elektrischen Strom. Da die Photonenenergie in unserem Fall nur einem Bruchteil der Bandlücke entspricht, ist diese Anregung nicht resonant, sondern nur durch Multi-Photonen-

Absorption oder Tunneln möglich. Diese Nichtlinearität der Ladungsträgeranregung führt dazu, dass das Anschalten des resultierenden Stroms auf einer Zeitskala erfolgt, die der halben Oszillationsperiode des optischen Anregungsfelds entspricht. Die vorgestellten Experimente untersuchen die Abhängigkeit der gemessenen Ströme von der Probengeometrie sowie den Probenmaterialien und demonstrieren ihre Anwendung in der optischen Metrologie.

Die Leitungsbandanregung und die Beschleunigung der Ladungsträger können durch die Verwendung von zwei getrennten Laserpulsen, des Injektions- und des Beschleunigungspulses, entkoppelt werden. Die Ladungsträgeranregung durch den Injektionspuls wirkt hierbei als zeitlich begrenztes Fenster, das den Beschleunigungspuls abrastern kann. Da dieses Fenster auf den Bereich von einer Femtosekunde ($1 \times 10^{-15}\,\mathrm{s}$) beschränkt ist, liegen die potentiell auflösbaren Testfrequenzen im Petahertzbereich. Der Abgleich des Stromsignals mit der elektro-optisch vermessenen Wellenform zeigt, dass sich die ultraschnellen Ströme zur Pulscharakterisierung eignen. Diese neuartige Methode, das *Starkfeld-Abtasten*, verfügt wie das elektro-optische Abtasten über eine breite spektrale Antwort und kann dank eines kompakten Versuchsaufbaus, der ohne Vakuumapparaturen auskommt, einfach in bestehende Experimente integriert werden.

Die in dieser Dissertation vorgestellten Messtechniken ermöglichen die Untersuchung feldinduzierter Elektronendynamiken und bereiten somit den Weg hin zu lichtfeldbasierter Signalverarbeitung.

Summary

Laser pulses can observe and control electronic properties of matter on the time scale of the optical field cycle [1]. In case the transient field strength reaches values just below the damage threshold of the material, the polarization response of the excited system depends on the field oscillations of the driving light wave rather than on its envelope. These ultrafast, light-field-driven dynamics of charge carriers can potentially be employed in petahertz (1×10^{15} Hz) signal processing [2]. In order to excite the electronic system in a well-controlled way and to analyze its dynamic response, we need metrology schemes capable of resolving the electric field of optical waveforms. However, this poses an experimental challenge: *How can we resolve light-field oscillations which are among the fastest reproducible signals we can generate in a laboratory?*

This dissertation aims at the improvement and development of novel metrology techniques for complete field characterization of few-cycle pulses and their application in the study of strong-field-induced charge carrier dynamics in solids.

In *electro-optic sampling*, an unknown test waveform overlaps with a short sampling pulse in an electro-optic crystal. The nonlinear interaction results in a polarization rotation of the sampling pulse which is proportional to the instantaneous field strength of the test waveform. Scanning the temporal delay between test and sampling pulse, the electric field oscillations of the test waveform are resolved by recording the delay-dependent polarization rotation [3]. This work extents the cutoff of this techniques, which was originally demonstrated in the terahertz domain, to frequencies in the near-infrared up to 235 THz, which corresponds to a wavelength of 1.27 µm. With this spectral cutoff, electro-optic sampling can serve as a diagnostic tool for broadband optical parametric amplifiers as well as for erbium-based laser systems operating in the 1.5 µm wavelength region. In a first demonstration, the waveform evolution for varying pump powers during optical parametric amplification is measured.

Furthermore, this work studies strong-field-induced currents in dielectric materials [4]. A short laser pulse injects charge carriers into the conduction band where they get accelerated by the optical field. Since the photon energies in our case are too small to bridge the band gap directly, the excitation occurs via multi-photon absorption or tunneling. This nonlinearity leads to the strong temporal confinement of the charge carrier excitation to about one half-cycle of the optical injection field. The presented experiments investigate the dependence of the measured current on different sample geometries and materials.

Ultrafast currents can be employed in optical metrology when the excitation and ac-

celeration of charge carriers are disentangled by using two separate laser pulses, denoted as injection and drive pulse. Thus, the carrier injection can act as a temporally confined gate which samples the drive waveform. Since the gate duration is on the order of one femtosecond (1×10^{-15} s), frequencies up to petahertz range can potentially be resolved. Comparing the measured current to the drive field, characterized by electro-optic sampling, shows that this measurement can be used as a pulse characterization technique, which we call *strong-field solid-state sampling*. Like electro-optic sampling, strong-field solid-state sampling features a broadband spectral response and a compact footprint in ambient conditions, which facilitates easy integration with existing experiments.

The metrology techniques presented in this dissertation permit the study of field-induced electron dynamics and thus pave the way towards light-field-based signal processing.

Contents

List of Author's Publications

Publications directly related to this thesis

- **Keiber, S.**, Sederberg, S., Schwarz, A., Trubetskov, M., Pervak, V., Krausz, F., Karpowicz, N., *Electro-optic sampling of near-infrared waveforms.* Nature Photonics 10, 159–162 (2016)
  The author built the setup, performed the measurements, analyzed the data, and prepared the manuscript together with S.S. and N.K.

- **Keiber, S.**, Paasch-Colberg, T., Schwarz, A., Razskazovskaya, O., Fedulova, E., Sağlam, Ö., Jakubeit, C., Sederberg, S., Dombi, P., Karpowicz, N., Krausz, F., *Investigation of laser-induced currents in large-band-gap dielectrics*, in: Ultrafast Phenomena XIX, Springer Proceedings in Physics. Springer International Publishing, 237–240 (2015)
  The author conceived the experiment together with N.K. and F.K., performed the measurements, analyzed the data, and prepared the manuscript.

- Paasch-Colberg, T., Schiffrin, A., Karpowicz, N., Kruchinin, S., Sağlam, Ö., **Keiber, S.**, Razskazovskaya, O., Mühlbrandt, S., Alnaser, A., Kübel, M., Apalkov, V., Gerster, D., Reichert, J., Wittmann, T., Barth, J.V., Stockman, M.I., Ernstorfer, R., Yakovlev, V.S., Kienberger, R., Krausz, F., *Solid-state light-phase detector.* Nature Photonics 8, 214–218 (2014)
  The author assisted in the measurements.

Publications related to the optimization of the experimental infrastructure used in this thesis

- Fattahi, H., Schwarz, A., Geng, X.T., **Keiber, S.**, Kim, D.E., Krausz, F., Karpowicz, N., *Decoupling chaotic amplification and nonlinear phase in high-energy thin-disk amplifiers for stable OPCPA pumping.* Optics Express 22, 31440 (2014)

- Fattahi, H., Schwarz, A., **Keiber, S.**, Karpowicz, N., *Efficient, octave-spanning difference-frequency generation using few-cycle pulses in simple collinear geometry.* Optics Letters 38, 4216–4219 (2013)
  In these two publications, the author assisted in optimizing the laser system used in the experiments.

Further publications by the author

- Kanal, F., **Keiber, S.**, Eck, R., Brixner, T., 100-kHz shot-to-shot broadband data acquisition for high-repetition-rate pump-probe spectroscopy. Optics Express 22, 16965–16975 (2014)
  The author participated in the planning and preliminary implementation of the acquisition setup in the framework of her Master's thesis.

List of Abbreviations

AC	alternating current
AOPDF	acousto-optic programmable dispersive filter
ATI	above-threshold ionization
BBO	β-barium borate
CCD	charge-coupled device
CEP	carrier envelope phase
CPA	chirped-pulse amplifier
DC	direct current
DFG	difference-frequency generation
EOS	electro-optic sampling
FISH	field-induced second harmonic
FROG	frequency-resolved optical gating
FWHM	full width at half maximum
GD	group delay
GDD	group-delay dispersion
HCF	hollow-core fiber
HEMT	high-electron-mobility transistor
HHG	high-harmonic generation
MIR	mid-infrared
MOSFET	metal-oxide-semiconductor field-effect transistor
NIR	near-infrared
OPA	optical parametric amplification
OPCPA	optical parametric chirped pulse amplifier
OR	optical rectification
PPLN	periodically poled lithium niobate
SFG	sum-frequency generation
SFS	strong-field solid-state sampling
SHG	second-harmonic generation
SPIDER	spectral phase interferometry for direct electric-field reconstruction
SPM	self-phase modulation
SWIR	short-wavelength infrared
TDSE	time-dependent Schrödinger equation
TG	transient grating

THG	third-harmonic generation
Ti:Sa	titanium-doped sapphire
VUV	vacuum ultraviolet
XFROG	cross-correlation frequency-resolved optical gating
Yb:YAG	ytterbium-doped yttrium aluminum garnet

List of Figures

Introduction

There is a time for some things, and a time for all things; a time for great things, and a time for small things.
Miguel de Cervantes, Don Quixote de la Mancha (1605-1615)

The small things which ultimately determine the nature of light-matter interaction in atoms, molecules, nanosystems, and solids are electrons. The time scale associated with electronic excitations lies on the order of a few femtoseconds (1×10^{-15} s) and below [5]. Since electronic metrology devices are far too slow to capture or even steer these fast processes, optical schemes are needed for this purpose. Continuous advances in laser technology over the last five decades have lead to the availability of phase-stable few-cycle pulses in the infrared to visible spectral range [6]. These pulses can act both as a diagnostic and as a control tool for electronic processes on the order of an optical half cycle.

After the attention of the ultrafast community has successfully focused on atomic and molecular systems [5], recent studies of dynamic processes in solids have broken new ground. Few-cycle phase-stable waveforms permit the observation of electron dynamics on unprecedented time scales, while their limited duration makes it possible to apply high electric fields on the order of 1×10^{10} V/m without damaging the target [7]. This parameter regime far above the DC damage threshold of the solid-state materials has enabled the investigation of new phenomena like the strong-field manipulation of dielectrics [1], the emission of bulk high harmonics [8, 9, 10], and the generation of optical-field-induced currents [4]. Light-field-driven electron dynamics furthermore offer exciting opportunities for the reversible manipulation of electronic signals on the petahertz scale [2].

While ultrafast strong-field physics in solids paves the way towards discovering novel physical phenomena in electron dynamics and advancing signal processing applications at the speed of optical frequencies, it also entails great challenges for optical metrology. Whenever studying the optically induced response of a dynamic system, knowledge of the temporal structure of the exciting waveform is essential. Despite the wealth of existing pulse characterization techniques (see for example [11]), their applicability in the strong-field regime is limited. This is due to the fact that the electronic response of the excited system is governed by the instantaneous electric field, not its envelope. In order to resolve electric field oscillations with frequencies up to the petahertz regime, improved and novel pulse characterization schemes are needed. This work introduces two powerful methods of measuring phase-stable waveforms: electro-optic and strong-field solid-state sampling.

Electro-optic sampling has successfully been applied in the terahertz to mid-infrared regime but its spectral cutoff has been restricted to 135 THz, which corresponds to a wavelength of 2.22 µm [12]. The advancements introduced in this thesis improve this cutoff to 235 THz (1.27 µm). For the first time, this enables characterizing the dynamic evolution of waveforms in the near- to short-wavelength-infrared. With its large dynamic range of 1×10^5, a sensitivity down to pulse energies of a few nanojoules, and its compact setup, electro-optic sampling is a beneficial diagnostic tool for phase-stable sources which have successfully been developed and applied to a multitude of strong-field experiments in a variety of systems over the last years [13, 14, 15].

Strong-field solid-state sampling is a novel metrology concept, which is demonstrated in this work for the first time. It employs the injection of ultrafast currents [4] as a gate in the sampling process. Whereas the well-established attosecond streak camera [16] uses a highly nonlinear process in a gaseous medium to generate the attosecond pulse employed as a gate, strong-field solid-state sampling uses a nonlinear process in a solid for the same purpose. In contrast to the streaking experiment, this facilitates a compact setup in ambient conditions without the need for complicated vacuum apparatuses and photoelectron diagnostics. Since this technique exploits a higher order nonlinearity than the electro-optic sampling, the gate can be much shorter than the fundamental sampling pulse. Thus, strong-field solid-state sampling holds promise to be applicable up to visible or ultraviolet frequencies.

This thesis is structured as follows:

Chapter 1 equips the reader with the basic theoretical framework for understanding the experimental results and discussions. After introducing the mathematical description of ultrashort pulses and their propagation, their interaction with matter beyond the linear regime is described. We then turn our attention to dynamic processes in solids, namely the transport of photoexcited charge carriers. The last section of the first chapter deals with optical-field-induced currents. It discusses the pioneering experimental results and their explanation within complementary theoretical models.

Chapter 2 introduces experimental tools which form the backbone of ultrafast experiments in general and this work in particular. The section on pulse characterization techniques discusses the state-of-the-art in optical metrology. The follow-up section describes the phase-stable light sources in the near- and short-wavelength-infrared regime used in the experiments presented in later chapters. A newly commissioned two-color interferometer facilitates the combined use of two phase-stable few-cycle pulses in different spectral regimes. These pulses are later employed as sampling and test waveform to demonstrate the pulse characterization techniques discussed below.

In Chapter 3, electro-optic sampling is introduced as a precise and versatile metrology tool for the characterization of the short-wavelength-infrared light source. After discussing the general concept, the experimental setup section provides an insight into the improvements that allow for a demonstration of broadband sampling and subsequent compression of the phase-stable pulse. In a first application, electro-optic sampling resolves waveform changes induced by pump energy variations in optical parametric amplification. The record-breaking spectral cutoff of 235 THz is presented before discussing the future

applications and potential advancements of this measurement scheme.

Chapter 4 lays the foundation for the upcoming chapter on strong-field solid-state sampling by investigating optical-field-induced currents in the single-pulse regime. In this simplified setup, the influence of the sample geometry and material on the measured current is studied. The outlook section provides ideas for further investigations of ultrafast carrier dynamics by combining the current measurements with other time-resolved techniques.

Chapter 5 treats the applicability of ultrafast carrier injection as a gate in strong-field solid-state sampling. After introducing the general concept and the employed experimental setup, the high drive intensity regime is investigated, where drive-field assisted tunneling occurs. The novel pulse characterization technique is demonstrated at low drive fields by comparing the current measurements to electro-optic sampling. Finally, its spectral cutoff, starting points for further research, and potential applications are discussed.

Finally, the results are summed up and assessed in Chapter 6. This includes the recapitulation of the motivation and challenges connected to the characterization of phase-stable waveforms as well as a discussion of the scope to which these challenges can be met by the presented metrology techniques. Final remarks on their applications, future developments, and improvements conclude this thesis.

Chapter 1

Theoretical Background

The purpose of this chapter is to equip the reader with the necessary background on ultrashort pulses and their interaction with matter. The laser pulses employed in this work are few-cycle pulses spanning over a broadband spectral range in the visible and infrared regime with a duration of merely a few femtoseconds.

The first section introduces the basic concepts of the mathematical description of ultrashort laser pulses in the time and frequency domain and their propagation in a dispersive medium. Section 1.2 focuses on the interaction of these laser pulses with matter at high intensities, in the so-called nonlinear and the nonperturbative regime, where the polarization response of the material is no longer directly proportional to the electric field. Section 1.3 describes the fundamental transport mechanisms of photoexcited charge carriers in a solid. The final section of this chapter presents theoretical concepts for explaining various aspects of the generation of optical-field-induced currents. This ultrafast charge transfer mechanism plays a central role in the experiments in Chapter 4 and Chapter 5.

Since an exhaustive treatment of all aspects of ultrafast optics is outside the scope of this work, textbook references are given for further reading.

1.1 Ultrashort Pulse Fundamentals

For this thesis, it is sufficient to treat the electric field classically. The description of the magnetic field is equivalent and can be derived directly from the presented results with the help of Maxwell's equations [17]. The discussion is therefore limited to the electric field, adhering to the SI system of units. Relativistic effects do not play a role at the experimental parameters discussed here and are neglected. There are excellent textbooks dealing with the description of ultrashort pulses, among them [18, 11, 19]. The following paragraphs will to a large extent follow the notation as introduced by Diels and Rudolph [18].

1.1.1 Mathematical Description of Ultrashort Pulses

The oscillating electric field E of a laser pulse can be equivalently described in time and frequency domain since both descriptions are linked via the Fourier transform:

$$E(\omega) = \int_{-\infty}^{\infty} E(t) e^{-i\omega t} \mathrm{d}t = \mathcal{F}[E(t)] \ , \tag{1.1}$$

$$E(t) = \frac{1}{2\pi} \int_{-\infty}^{\infty} E(\omega) e^{i\omega t} \mathrm{d}\omega = \mathcal{F}^{-1}[E(\omega)] \ . \tag{1.2}$$

Although the electric field in the time domain is a real quantity, it is more convenient for the mathematical description to work with the complex analytic signal [18]

$$E^+(t) = E(t) + i\mathscr{H}[E(t)] \ , \tag{1.3}$$

where $\mathscr{H}$ stands for the Hilbert transform. This way, the electric field can conveniently be factorized into an envelope and a phase term:

$$E^+(t) = |E^+(t)| e^{i\Gamma(t)} = |E^+(t)| e^{i(\omega_0 t + \varphi(t) + \varphi_0)} \ , \tag{1.4}$$

where the phase $\Gamma(t)$ can be decomposed into a term featuring fast oscillations at the laser frequency ω_0, a time-dependent phase $\varphi(t)$, and a constant phase offset, the so-called carrier envelope phase (CEP) φ_0. While for longer pulses the effect of the CEP on the pulse shape is negligible, it has a strong influence on few-cycle pulses as shown in Fig. 1.1. In this work, the CEP of a few-cycle pulse plays an important role as a control knob for the field-controlled — not intensity-controlled — processes which are explored in later chapters.

If we can assume that the changes in the phase $\varphi(t)$ are slow compared to the fast oscillations at the laser frequency, it is useful to introduce the complex envelope $\mathcal{E}(t) = |E^+(t)| e^{i(\varphi(t)+\varphi_0)}$ of the pulse such that

$$E^+(t) = \mathcal{E}(t) \mathrm{e}^{i\omega_0 t} \ . \tag{1.5}$$

This allows us to define $E^+(\omega)$ which is the Fourier transform of the complex analytic signal $E^+(t)$ and contains only positive frequencies [18]:

$$E^+(\omega) = \mathcal{F}[E^+(t)] = \begin{cases} E(\omega) & \text{for } \omega \geq 0 \\ 0 & \text{for } \omega < 0 \end{cases} \ . \tag{1.6}$$

Equivalently to the temporal field, $E^+(\omega)$ can also be expressed in terms of amplitude and phase:

$$E^+(\omega) = |E^+(\omega)| \, e^{-i\Phi(\omega)} \ , \tag{1.7}$$

where $\Phi(\omega)$ carries important information on the spectral and temporal shape of the electric field. It is instructive to expand $\Phi(\omega)$ in a Taylor series around ω_0 [19].

$$\Phi(\omega) = \sum_{j=0}^{\infty} \frac{b_j}{j!} (\omega - \omega_0)^j \ , \tag{1.8}$$

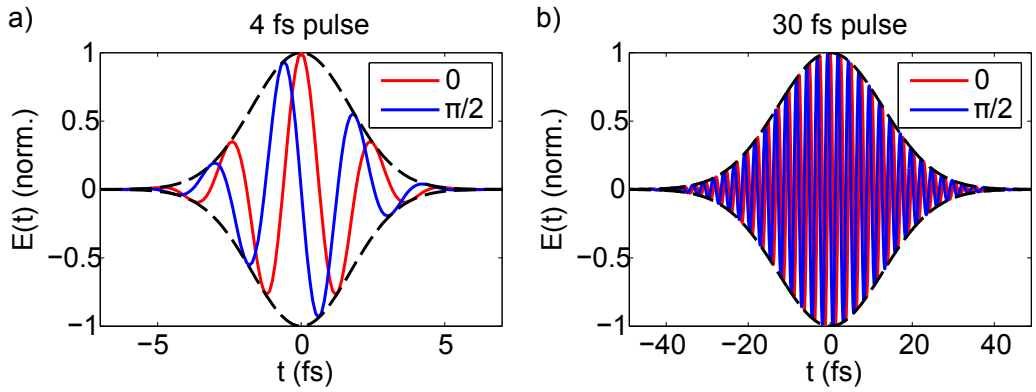

Figure 1.1: CEP of Few-Cycle Pulse. a) shows the strong CEP dependence of the pulse shape for a 4 fs pulse while b) illustrates the negligible effect in case of a 30 fs pulse which is a typical output duration for a commercial ultrashort pulse amplifier. Red: cosine-like pulse with $\varphi_0 = 0$. Blue: sine-like pulse with $\varphi_0 = \pi/2$. Dashed black: pulse envelope

with the Taylor coefficients

$$b_j = \left.\frac{\mathrm{d}^j \Phi(\omega)}{\mathrm{d}\omega^j}\right|_{\omega_0} . \tag{1.9}$$

The zeroth order is equivalent to the aforementioned CEP ($\varphi_0 = -\Phi(\omega_0)$). The first order is known as group delay (GD). It leads to an overall retardation of the electric field. The second order is the group-delay dispersion (GDD) which influences the relative timing between different frequency components and leads to an elongation of the pulse in the time domain, see Fig. 1.2. A pulse, whose different spectral components arrive at different times, is called chirped. Higher order phases like the third- and fourth-order dispersion also influence the shape of the pulse strongly by introducing satellite pulses and pedestals. For a more detailed overview on the influence of different phase terms on the pulse shape, consult [19] or [20].

Important experimental quantities are the temporal intensity $I(t)$, which results from the time average of the modulus square of the electric field over one oscillation period, and its equivalent in the frequency domain $I(\omega)$ [19].

$$I(t) = c\,\epsilon_0\,n\,\frac{1}{T}\int_{t-\frac{T}{2}}^{t+\frac{T}{2}} E^2(t')\mathrm{d}t' = 2\,c\epsilon_0 n|E^+(t)|^2 , \tag{1.10}$$

$$I(\omega) = \frac{c\,\epsilon_0\,n}{\pi}|E^+(\omega)|^2, \tag{1.11}$$

where c is the speed of light in vacuum, ϵ_0 the vacuum permittivity, n the real part of the index of refraction in the medium, and $T = \frac{2\pi}{\omega}$ the oscillation period.

Two important characteristics of a laser pulse can be derived from this intensity definition. Its temporal duration τ_p and spectral width $\Delta\omega$ are given by the full width at half maximum (FWHM) of the respective intensity profiles [18]:

$$\tau_\mathrm{p} = \mathrm{FWHM}\left[I(t)\right] , \tag{1.12}$$

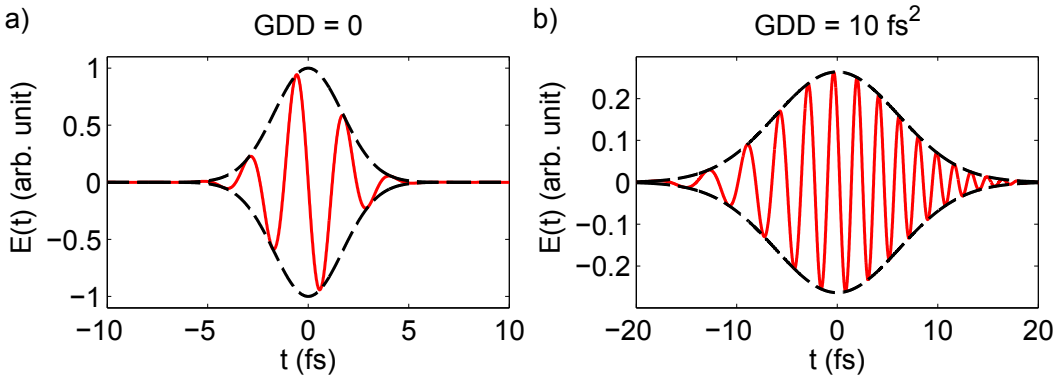

Figure 1.2: Transform-Limited versus Chirped Pulse. The pulse in a) has a flat spectral phase and is transform-limited. The spectral phase of the pulse in b) is quadratic with a GDD of $10\,\mathrm{fs}^2$. Longer wavelength components arrive earlier, shorter wavelength components later. The pulse is stretched in time (chirped) which leads to a reduction of the maximum instantaneous field. The spectral intensity is the same for both pulses. Red: instantaneous electric field. Dashed black: pulse envelope.

$$\Delta\omega = \mathrm{FWHM}\left[I(\omega)\right] \ . \tag{1.13}$$

Since the electric fields in time and frequency description are linked via their Fourier relationship, there is a lower limit of the so-called time–bandwidth product [19]

$$\tau_\mathrm{p}\Delta\omega \geq c_\mathrm{B} \ , \tag{1.14}$$

where the constant c_B depends on the shape of the pulse. In the case of a Gaussian pulse, $c_B = 4\ln 2$. For a transform-limited pulse with a flat spectral phase, the time-bandwidth product is minimal and the equality in Eqn. 1.14 holds.

A train of short pulses results in a frequency comb in Fourier space. The line-width of the individual comb teeth is inversely proportional to the temporal width of the pulses. The comb spacing is given by the repetition rate f_{rep}, the offset is the so-called carrier-offset-frequency f_{CEO} which is closely related to the CEP difference $\Delta\varphi_0$ between consecutive pulses in the pulse train [21]:

$$f_{CEO} = \frac{\Delta\varphi_0 \bmod 2\pi}{2\pi} f_{rep} \ . \tag{1.15}$$

Fig. 1.3 schematically illustrates the correspondence between a train of ultrashort pulses and a frequency comb. In this example, $f_{CEO} = f_{rep}/4$ which means that the CEP slips by $\pi/2$ from pulse to pulse and every fourth pulse is identical. For $f_{CEO} = 0$, φ_0 is constant.

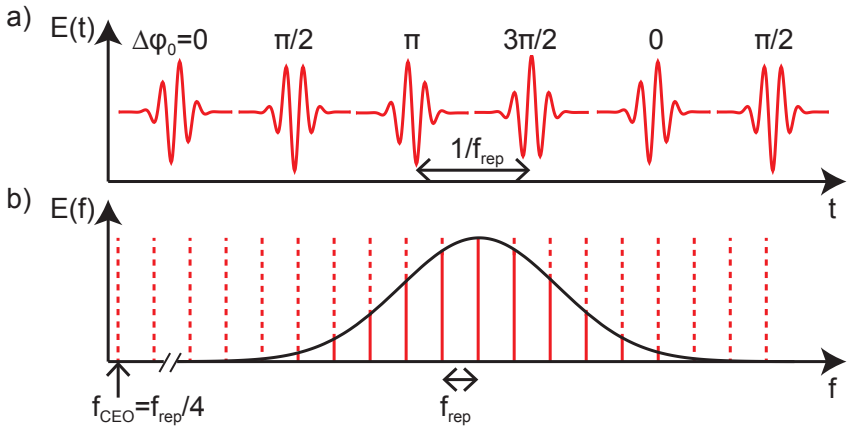

Figure 1.3: Frequency Comb. a) A train of ultrashort pulses in the time domain corresponds to a frequency comb in Fourier space, as schematically illustrated in the b). The comb lines are spaced by the repetition rate f_{rep}. In this example, the carrier envelope offset frequency f_{CEO} is one fourth of the f_{rep} which corresponds to a CEP slip $\Delta\varphi_0$ of $\pi/2$ between consecutive pulses.

1.1.2 Propagation of Ultrashort Pulses

The propagation of an electric field $\mathbf{E}(\mathbf{r},t)$ in a medium is governed by the nonlinear wave equation which can be derived from Maxwell's equations [17]. For non-magnetic media and a vanishing free current density, it assumes the form

$$\nabla \times \nabla \times \mathbf{E}(\mathbf{r},t) + \frac{1}{c^2}\frac{\partial^2}{\partial t^2}\mathbf{E}(\mathbf{r},t) = -\frac{1}{\epsilon_0 c^2}\frac{\partial^2}{\partial t^2}\mathbf{P}(\mathbf{r},t) \ , \tag{1.16}$$

where $\mathbf{P}$ is the polarization response of the medium and vector quantities are denoted in bold font. If we assume a fixed propagation direction along the z-axis, the electric field can be split into a scalar function $u(\mathbf{r})$, which describes the spatial beam profile, and a vector field $\mathbf{E}(z,t)$, which determines the time-dependence and propagation in z-direction, in the following way [22]:

$$\mathbf{E}(\mathbf{r},t) = u(\mathbf{r})\,\mathbf{E}(z,t) \ . \tag{1.17}$$

In the next paragraph, we will consider the vector field $\mathbf{E}(z,t)$ and its propagation through a dispersive medium before we turn to the propagation characteristics of the spatial beam profile $u(\mathbf{r})$ and discuss the special case of a Gaussian beam.

Propagation through a Dispersive Medium A short pulse can be expressed as a coherent superposition of monochromatic waves. In a dispersive medium, these waves travel at different velocities because the optically induced polarization imposes frequency-dependent changes on the incident electric field. This results in a shift of the different frequency components with respect to each other and influences the pulse shape. Mathematically, this can be described by the spectral phase, introduced in Eqn. 1.7.

Neglecting the spatial beam profile and concentrating on one particular polarization direction, Eqn. 1.16 reduces to

$$\left(\frac{\partial^2}{\partial z^2} - \frac{1}{c^2}\frac{\partial^2}{\partial t^2}\right) E(z,t) = \frac{1}{\epsilon_0 c^2}\frac{\partial^2}{\partial t^2} P(z,t) \ . \tag{1.18}$$

In case of a linear response $P(\omega, z) = \epsilon_0 \chi(\omega) E(\omega, z)$, with a scalar dielectric susceptibility $\chi(\omega)$, we can use a Fourier ansatz for the electric field and derive the following solution in frequency space

$$E(\omega, z) = E(\omega, 0)\, e^{-ik(\omega)z} \ , \tag{1.19}$$

where $k(\omega) = \frac{\omega}{c}\tilde{n}(\omega)$ is the wave vector in propagation direction z. The index of refraction $\tilde{n}(\omega)$ is defined as [23]

$$\tilde{n}(\omega) = \sqrt{1 + \chi(\omega)} = n(\omega) + i\kappa(\omega) \ . \tag{1.20}$$

It is a complex quantity which characterizes the light-matter interaction in the linear regime. The imaginary part is called extinction coefficient $\kappa(\omega)$ and describes the damping or enhancement of the field amplitude due to absorption or gain in the medium. The real part $n(\omega)$ is responsible for the frequency-dependent change of the speed of light, which results in refraction and dispersion. The real and imaginary parts of the refractive index are linked by the Kramers-Kronig relation [17]:

$$n(\omega) = 1 + \frac{c}{\pi}\mathcal{P}\int_0^\infty \frac{\kappa(\omega)}{\Omega^2 - \omega^2}\, \mathrm{d}\Omega \ , \tag{1.21}$$

where $\mathcal{P}$ denotes the Cauchy principle value of the integral. The real part of the refractive index for different materials is often given in terms of the wavelength λ

$$n(\lambda) = n(\omega)\left|\frac{\mathrm{d}\omega}{\mathrm{d}\lambda}\right| = \frac{2\pi c}{\lambda^2}\, n(\omega) \tag{1.22}$$

by the so-called Sellmeier equation [24]:

$$n^2(\lambda) = 1 + \frac{B_1\lambda^2}{\lambda^2 - C_1} + \frac{B_2\lambda^2}{\lambda^2 - C_2} + \frac{B_3\lambda^2}{\lambda^2 - C_3} \ , \tag{1.23}$$

where $B_{1,2,3}$ and $C_{1,2,3}$ are the experimentally determined Sellmeier coefficients. In case $n(\lambda)$ depends on the polarization and propagation direction of the light field traveling through the material, the crystal is birefringent.

If a laser pulse traverses a transparent ($\kappa = 0$), dispersive medium of length L, its spectral phase $\Phi(\omega)$ is altered according to [19]

$$\Phi(\omega, L) = \Phi(\omega, 0) + k(\omega)L = \Phi(\omega, 0) + \frac{\omega n(\omega) L}{c} \ . \tag{1.24}$$

By inserting $\Phi(\omega, L)$ into Eqn. 1.9, the Taylor coefficients b_j can be written as

$$b_1 = GD = L\frac{\mathrm{d}k}{\mathrm{d}\omega}\bigg|_{\omega_0} = \frac{L}{v_g} = \frac{L}{c}\left(n - \lambda\frac{\mathrm{d}n}{\mathrm{d}\lambda}\right) , \tag{1.25}$$

$$b_2 = GDD = L\frac{\mathrm{d}^2k}{\mathrm{d}\omega^2}\bigg|_{\omega_0} = \frac{\lambda^3 L}{2\pi c^2}\frac{\mathrm{d}^2n}{\mathrm{d}\lambda^2} \text{ , etc.} \tag{1.26}$$

with the group-velocity $v_g = \frac{\mathrm{d}\omega}{\mathrm{d}k}\Big|_{\omega_0}$. In a dispersive medium, the phase velocity $v_p = c/n$ and v_g are not equal, which means that the relative timing between the envelope and the carrier wave changes during propagation, resulting in a slip of the CEP. As already mentioned in the previous subsection, the GDD and higher order terms of the phase lead to a redistribution of the spectral components in time, resulting in a reshaped pulse. One can define the dispersion length L_D as the propagation distance over which the pulse duration due to GDD doubles

$$L_D = \frac{\tau_p^2}{|b_2|} . \tag{1.27}$$

In order to maintain a short pulse for time-resolved experiments, the phase it accumulates while traveling through air or through transmissive optical elements like filters or lenses has to be corrected. GDD can, to a certain degree, be canceled with the help of prisms [25] and diffraction gratings [26]. For the compensation of higher order spectral phase terms, chirped mirrors [27] or programmable spectrum and amplitude shapers based on liquid crystal displays (LCDs) [28] or acousto-optical modulators [29] can be employed.

In case the polarization on the right hand side of Eqn. 1.18 takes a more complicated form than a purely linear response, it can be useful to simplify the propagation equation by introducing the slowly-evolving wave approximation [30]. If we express the electric field $E(z,t)$ and the polarization $P(z,t)$ in terms of their Fourier components $E_\omega(z)$ and $P_\omega(z)$ and insert the expressions in Eqn. 1.16, we arrive at

$$\frac{\partial^2}{\partial z^2}E_\omega(z) = -\frac{\omega^2}{c^2}\left(E_\omega(z) + \frac{1}{\epsilon_0}P_\omega(z)\right) . \tag{1.28}$$

If the field is propagating in forward direction along the z-axis, it can be decomposed into an amplitude times the oscillating wave $E_\omega(z) = F(z)\exp(ik_\omega z)$, with $k_\omega = \omega n(\omega)/c$. In the framework of the slowly-evolving wave approximation, we can neglect $\partial^2 F(z)/\partial z^2$. Together with the decomposition of the polarization response into a linear and a nonlinear term, $P_\omega(z) = \epsilon_0\chi(\omega)E_\omega(z) + P_\omega^{NL}(z)$, this leads to a first-order propagation equation:

$$\frac{\partial E_\omega(z)}{\partial z} = ik_\omega E_\omega(z) + \frac{i\omega}{2n(\omega)\epsilon_0 c}P_\omega^{NL}(z) . \tag{1.29}$$

In case the assumptions made during the derivation are justified, this equation is valid for arbitrary waveforms.

Gaussian Beam Propagation Now let us focus on the evolution of the spatial beam profile $u(\mathbf{r})$. Although plane waves provide a mathematically correct solution for the wave equation (see Eqn. 1.16), their physical interpretation is problematic. Plane waves propagating in z-direction extend to infinity in the x–y plane. Laser beams on the other hand have a finite spatial spread, which leads to fundamental consequences for their focusing properties.

For a vanishing polarization $\mathbf{P}$ and only slow variations of the spatial profile in z-direction, Eqn. 1.16 and Eqn. 1.17 can be rearranged into the paraxial wave equation [11]:

$$\left(\nabla_t^2 - 2ik\frac{\partial}{\partial z}\right) u(\mathbf{r}) = 0 \ , \tag{1.30}$$

where $\nabla_t^2 = \frac{\partial^2}{\partial x^2} + \frac{\partial^2}{\partial y^2}$ is the second spatial derivative with respect to the transverse Cartesian coordinates and k is the amplitude of the wave vector in z-direction. This equation can be solved by assuming a Gaussian beam, which corresponds to the operating mode of most femtosecond lasers. The spatial profile takes the form [11]

$$u(x,y,z) = \frac{w_0}{w(z)} e^{-(x^2+y^2)/w^2(z)} e^{-ik(x^2+y^2)/2R(z)} e^{i\Psi(z)} \ . \tag{1.31}$$

The beam radius $w(z)$ is defined as the distance from the center of the beam where the field amplitude has decreased to $1/e$ of its maximum value. The focus lies at $z = 0$ where the beam waist is given by w_0. $R(z)$ is the radius of curvature of the phase fronts. The so-called Guoy phase $\Psi(z)$ causes a π phase shift across the focus.

An important measure for the collimation quality of a Gaussian beam is the Rayleigh range [22]

$$z_R = \frac{\pi w_0^2}{\lambda} \ . \tag{1.32}$$

It is given by the distance a collimated beam can travel before doubling its area due to divergence. z_R depends quadratically on w_0 and is inversely proportional to the wavelength. The power $P(r,z)$ which is transmitted through an aperture of radius r placed in the beam is given by

$$P(r,z) = P_0 \left[1 - \exp\left(-\frac{2r^2}{w^2(z)}\right)\right] \ , \tag{1.33}$$

where P_0 is the total power. Fig. 1.4 schematically summarizes the significant parameters of a Gaussian beam.

1.2 Light-Matter Interaction Beyond the Linear Regime

This section will focus on the polarization of a medium interacting with light once the linear response assumed in Subsection 1.1.2 is no longer valid. Excellent textbook references for this section are [31, 32] as well as [33] for the solid-state part of Subsection 1.2.2.

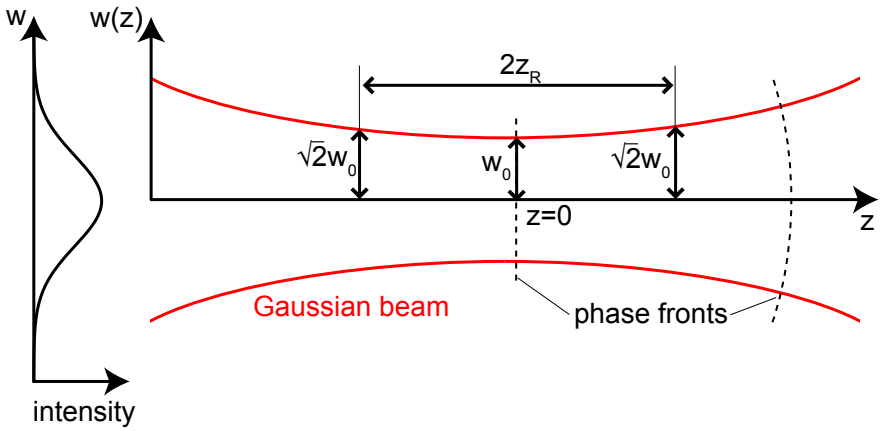

Figure 1.4: Propagation of Gaussian Beam, in z-direction, focused at $z = 0$. The red lines denote the radius $w(z)$ of the beam where the field has fallen off to $1/e$ of its peak intensity at the center. The phase fronts in the focus and the far-field are depicted in dashed lines. The left-hand side of the illustration shows the spatial intensity profile of the beam.

1.2.1 The Nonlinear Regime

In the frequency domain, the vector components P_i of the polarization response can approximately be expressed by an expansion in terms of the electric field [31]:

$$\begin{aligned}\frac{P_i}{\epsilon_0} =& \chi^{(1)}_{ij} E_j(\omega_m) + \chi^{(2)}_{ijk} E_j(\omega_m) E_k(\omega_n) + \\ & \chi^{(3)}_{ijkl} E_j(\omega_m) E_k(\omega_n) E_l(\omega_o) + \dots ,\end{aligned} \tag{1.34}$$

where ω_m, ω_n, and ω_o denote frequencies of incoming electric fields and ijk refer to the Cartesian coordinates. Einstein summation convention is assumed to simplify the notation. The dielectric susceptibility $\chi^{(r)}$ is a tensor of rank (r+1) and describes the response of a system to an electric field $E(\omega)$. If we consider only one polarization component of the interacting fields and assume instantaneous response in a dispersionless and lossless medium, the polarization in the time domain can be written in a compact form

$$\frac{P(t)}{\epsilon_0} = \chi^{(1)} E(t) + \chi^{(2)} E^2(t) + \chi^{(3)} E^3(t) + \dots . \tag{1.35}$$

In general, the nonlinear polarization response in time has to be calculated by taking the Fourier transform of the frequency domain response in Eqn. 1.34. The question if the nonlinear response is instantaneous or not is essential for the amount of energy deposited in the sample. It can be quantified by the work $W(t)$ done by the laser field on the electrons in the transparent material. In case the linear contributions can be neglected, this equals to

$$W(t) = \int_{-\infty}^{t} E(t') \frac{\mathrm{d}}{\mathrm{d}t'} P_{NL}(t') \, \mathrm{d}t' \ . \tag{1.36}$$

If $E(t)$ and $P_{NL}(t)$ do not oscillate in phase, there is an energy transfer either from the laser field to the sample or the other way round. This dynamic energy transfer has been resolved for terahertz [34] up to optical frequencies [35].

The two important special cases of second- and third-order nonlinear processes are discussed in the following paragraphs.

Second-Order Nonlinear Processes In the case of a second-order nonlinear process, the $\chi^{(2)}$ tensor leads to a polarization response which depends quadratically on the incident light field. If we assume that the incoming electric field is given by $E(t) = \mathcal{E}_1 e^{i\omega_1 t} + \mathcal{E}_2 e^{i\omega_2 t} +$ c.c. and it passes through a lossless, dispersionless system with $\chi^{(2)} \neq 0$, it will create an instantaneous polarization response $P^{(2)}(t) = \epsilon_0 \chi^{(2)} E(t)^2$. The polarization response can be split into the following spectral contributions [31]:

$$\begin{aligned} P(0) &= \epsilon_0 \chi^{(2)} (|\mathcal{E}_1|^2 + |\mathcal{E}_2|^2) && \text{OR} \\ P(2\omega_1) &= \epsilon_0 \chi^{(2)} \mathcal{E}_1^2 && \text{SHG} \\ P(2\omega_2) &= \epsilon_0 \chi^{(2)} \mathcal{E}_2^2 && \text{SHG} \\ P(\omega_1 + \omega_2) &= 2\,\epsilon_0 \chi^{(2)} \mathcal{E}_1 \mathcal{E}_2 && \text{SFG} \\ P(\omega_1 - \omega_2) &= 2\,\epsilon_0 \chi^{(2)} \mathcal{E}_1 \mathcal{E}_2^* && \text{DFG} \end{aligned} \tag{1.37}$$

The polarization terms at negative frequencies can be obtained by taking the complex conjugate of the above mentioned quantities.

In the case of optical rectification (OR), the fast field oscillations are eliminated and the field follows the envelope of the incident pulses. This phenomenon has successfully been employed for the generation of intense terahertz waveforms [36, 37]. Second-harmonic generation (SHG) is a special case of sum-frequency generation (SFG), which combines ω_1 and ω_2 to emit a higher frequency photon. In SHG the energy of two photons from the same laser field is used to emit one photon with twice the fundamental energy. Difference-frequency generation (DFG) produces a frequency output with the difference of ω_1 and ω_2. In case one of the incoming fields is much more intense than the other, this process enables optical parametric amplification (OPA). An intense pump signal at frequency ω_1 amplifies a seed signal at ω_2. The newly created beam with a frequency $\omega_1 - \omega_2$ is called idler. The short-wavelength-infrared (SWIR) laser source, which is introduced in Subsection 2.2.2, utilizes the OPA process for the generation of intense, broadband pulses.

A more general description of the second-order polarization response as a vector quantity which also takes the noninstantaneous response due to losses into account, is given by [31]

$$P_i(\omega_n + \omega_m) = \epsilon_0 D \sum_{jk} \chi^{(2)}_{ijk}(\omega_n + \omega_m, \omega_n, \omega_m) E_j(\omega_n) E_k(\omega_m) \ , \tag{1.38}$$

where D is a degeneracy factor which equals the number of distinct permutations of the incoming frequencies and ijk are the Cartesian coordinates. Higher order nonlinear response terms can be expressed in a similar fashion.

It is important to note that $\chi^{(2)}$ has to vanish for centrosymmetric media due to their inversion symmetry. In the nonlinear susceptibility tensor, depending on the symmetry of the crystal, only a limited number of tensor coefficients are independent from each other. For these symmetry considerations and how they can lead to a more compact representation of the susceptibility in terms of the scalar effective nonlinearity d_{eff}, the reader is referred to [31].

In case one of the incoming fields is static (or very slowly varying), the second-order nonlinear susceptibility describes the linear electro-optic effect, also known as direct current (DC) Pockels effect. The polarization response in this case is described by [31]

$$P_i(\omega) = 2\epsilon_0 \sum_{jk} \chi^{(2)}_{ijk}(\omega = \omega + 0) E_j(\omega) E_k(0) \ . \tag{1.39}$$

The applied electric field leads to a linear change in the refractive index, which is polarization dependent. It effectively changes the birefringence of the material and thus transforms it into a voltage-driven wave plate. The resulting polarization rotation of the incoming light wave can be used in electro-optic modulators and in electro-optic sampling, which is introduced in Chapter 3.

An important prerequisite for efficient frequency conversion is the so-called phase matching which corresponds to momentum conservation [11]:

$$\mathbf{k}_i = \mathbf{k}_j + \mathbf{k}_k \ , \tag{1.40}$$

where $\mathbf{k}_i$, $\mathbf{k}_j$, and $\mathbf{k}_k$ are the wave vectors of the contributing electric fields. Due to chromatic dispersion (see Eqn. 1.24), this condition is in general not fulfilled over a long propagation distance for interacting light fields of different wavelengths. Using a birefringent crystal and adjusting the orientation of the optical axis with respect to the polarization of the incoming electric fields, phase matching can be achieved using distinct refractive indices for different polarization components. Depending on the polarizations of the two incoming beams, two types of phase matching are typically distinguished: For type I phase matching, E_j and E_k have the same polarization while in the case of type II phase matching, the polarizations of the incoming beams are perpendicular to each other.

In case the phase-matching condition can not be fulfilled by tuning the optical axis of a birefringent crystal, a technique called quasi-phase-matching allows to limit the wave vector mismatch $\Delta k = k_1 + k_2 - k_3$ [31]. It relies on periodically poled materials which are grown in such a way that the nonlinear susceptibility periodically changes sign. This principle is used in the first two OPA stages described in Subsection 2.2.2 in order to make use of the largest nonlinear coefficient in $LiNbO_3$. This requires all interacting waves to have the same polarization and thus eliminates birefringence as phase-matching mechanism [38].

Third-Order Nonlinear Processes For centrosymmetric materials with vanishing $\chi^{(2)}$, the $\chi^{(3)}$ susceptibility governs the lowest order nonlinear interaction. Since electric fields

with four different wavelengths can take part in a $\chi^{(3)}$ process, one often speaks of four-wave mixing. For the scope of this work however, it is sufficient to consider only fields with the same wavelength and a single polarization component, leading the polarization response [31]

$$P^{(3)}(\omega) = 3\epsilon_0\chi^{(3)}(\omega = \omega + \omega - \omega)|E(\omega)|^2 E(\omega) \ . \tag{1.41}$$

The imaginary part of $\chi^{(3)}$ describes a non-parametric process, meaning that the ground and final state of the system interacting with the light field are not identical. One example for such a process is two-photon absorption, which results into a loss channel for the bulk silicon compressor of the SWIR source in Subsection 2.2.2 and serves as the enabling mechanism for using silicon-based beam diagnostics to characterize the focused SWIR light in Section 3.2. Considering the real part of $\chi^{(3)}$ alone, the nonlinearity leads to an intensity-dependent refractive index

$$n = n_0 + n_2 I \ , \tag{1.42}$$

with $n_2 = \frac{3}{4n_0^2\epsilon_0 c}\chi^{(3)}$, which is typically on the order of a few $1 \times 10^{-20}\,\mathrm{m}^2/\mathrm{W}$ in the off-resonant case [39]. For a temporal variation of the field envelope, this intensity dependence, also denoted as the optical Kerr effect, leads to the generation of new frequency via self-phase modulations (SPM) and plays an important role in the generation of broad spectra, also known as supercontinuum generation. Supercontinua are widely used to approach the few-to-single cycle regime with pulses from conventional laser sources like the titanium-doped-sapphire (Ti:Sa) front end described in Subsection 2.2.1 [40]. The time-varying nonlinear phase $\Phi_{NL}(t) = -n_2 I(t)\omega_0 L/c$ which the laser pulse acquires by traveling through a transparent medium leads to a change in instantaneous frequency [31]:

$$\omega(t) = \omega_0 + \delta\omega(t) = \omega_0 + \frac{\mathrm{d}}{\mathrm{d}t}\Phi_{NL}(t) \ . \tag{1.43}$$

Once the frequency shift $\delta\omega$ exceeds the spectral width of the original pulse, new frequency components lead to spectral broadening of the pulse with blue components at the trailing and red components at the leading edge, assuming n_2 is positive. SPM is accompanied by self-steepening which results from the intensity dependence of the group velocity. The peak of the pulse envelope is slowed down with respect to the edges of the pulse which leads to a steepening of the trailing edge [31].

Since the intensity of a laser pulse not only varies in time but also in space, the intensity-dependent refractive index has further implications, namely the so-called Kerr-lensing. If a collimated Gaussian beam, described in Subsection 1.1.2, traverses a plate of constant thickness, the intensity profile leads to a modulated refractive index which acts like a convex lens. The consequent focusing of the beam is schematically depicted in Fig. 1.5. This mechanism is used in Kerr-lens mode-locked oscillators to reduce the cavity losses compared to continuous-wave operation, which leads to the emission of ultrashort pulses [11]. A Kerr-lens mode-locked oscillator is the central component of the Ti:Sa front end for both laser systems described in Subsection 2.2.1 and Subsection 2.2.2.

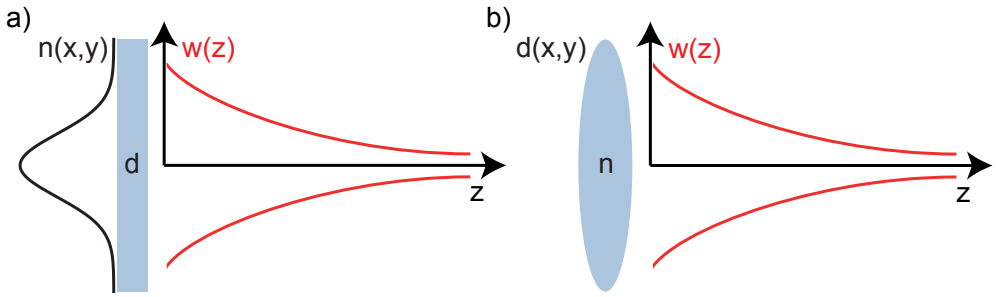

Figure 1.5: Kerr Lens. a) Schematic illustration of the analogy between a Kerr lens and b) a traditional convex lens. Instead of the propagation thickness d, the index of refraction n is modulated transversely to the propagation direction in the $x-y$ plane, which leads to a focusing in propagation direction z.

1.2.2 The Nonperturbative Strong-Field Regime

For large field strengths which are not negligible compared to the atomic field

$$E_{at} = \frac{e/4\pi\epsilon_0}{a_0^2} = 5.14 \times 10^{11}\mathrm{V/m} \ , \tag{1.44}$$

where a_0 is the Bohr radius, the expansion of the polarization response given by Eqn. 1.34 does not converge anymore [31]. In this nonperturbative strong-field regime, new aspects of light-matter interaction can be observed which cannot be described in the framework of the previous subsection. Besides the high intensity, there can be other reasons for a breakdown of the perturbative description of light-matter interaction like gain saturation in the medium, quantum interference, or a Rabi frequency larger than the inverse excited-state lifetime of the system [31]. These regimes will not be discussed further in the scope of this work.

One phenomenon which is of central importance to this work is strong-field ionization. Strong-field ionization in gases and dielectrics can be described in an analogous manner because the involved energy barriers, the atomic ionization potential I_p and the band gap Δ_g, typically lie within the same range. The most important difference is the final state of the electron. While in the case of the gas the electron is released into the continuum, it remains in the periodic potential of conduction band in the case of the solid.

The formalism which Keldysh developed in [41] holds for the ionization in gases and the interband tunneling in solid media alike. The central variable of this theory is the so-called Keldysh parameter

$$\gamma_K(\mathrm{solids}) = \frac{\omega_L\sqrt{m_{red}\Delta_g}}{eE_L} \ , \tag{1.45}$$

$$\gamma_K(\mathrm{gases}) = \frac{\omega_L\sqrt{2m_e I_p}}{eE_L} \ , \tag{1.46}$$

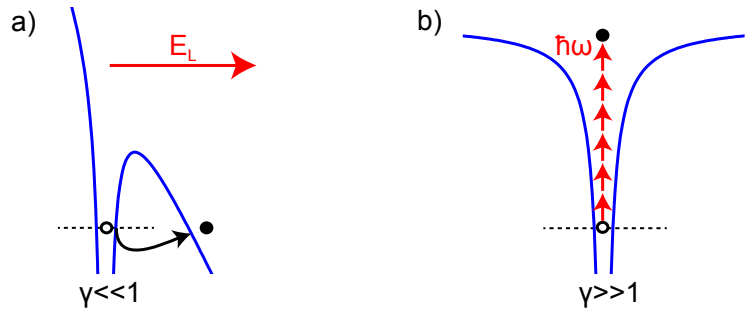

Figure 1.6: Regimes of Strong-Field Ionization. a) For small Keldysh parameters, the tunneling regime is dominant. The applied electric field E_L tilts the atomic potential such that the electron can tunnel out with a certain probability - illustrated by the black arched arrow. b) For large Keldysh parameters, the system is in the multi-photon regime. The atomic potential stays almost unperturbed and the electron absorbs a well-defined number of photons to escape into vacuum/the conduction band.

where ω_L denotes the laser frequency, m_e the electron mass, m_{red} the reduced effective mass of electron and hole ($1/m_{red} = 1/m^e_{eff} + 1/m^h_{eff}$) and E_L the electric field strength applied by the laser. It defines two asymptotic regimes of strong-field ionization: the multi-photon and the tunneling regime. In case $\gamma_K << 1$, tunneling is dominant, for $\gamma_K >> 1$ the electron escapes the atomic potential by absorbing several photons in a nonlinear process. In the intermediate regime for $\gamma_K \approx 1$, where the experiments presented in Chapter 4 and Chapter 5 will take place, the contributions from these two regimes cannot be distinguished.

Keldysh developed a generalized ionization rate Γ_{GKF} [41] which can successfully be applied in a broad parameter range and is depicted in Fig. 1.7:

$$\begin{aligned} \Gamma_{GKF} &= \frac{2\omega_L}{9\pi}\left[\frac{m\omega_L}{\hbar\beta}\right]^{3/2} Q(\gamma_K, \tilde{N}) \exp\left[-\pi\left\lfloor \tilde{N}+1\right\rfloor \frac{K(\beta)-I(\beta)}{I(\alpha)}\right], \\ \alpha &= (1+\gamma_K^2)^{-1/2},\ \beta = \gamma_K\alpha,\ \tilde{N} = \frac{\tilde{\Delta}_g}{\hbar\omega_L},\ \tilde{\Delta}_g = \frac{2I(\alpha)\Delta_g}{\pi\beta},\ N = \frac{\Delta_g}{\hbar\omega_L}\ , \end{aligned} \tag{1.47}$$

where $\tilde{\Delta}_g$ is the effective ionization potential, the functions $K(z)$ and $I(z)$ the complete elliptic integrals of first and second kind, $\lfloor x \rfloor$ denotes the integer part of x, and Q is a slowly-varying quantity describing the discrete spectrum of the absorbed photons (see [41, 33] for the full mathematical expression and further details). The validity of this approximation can be confirmed by numerical comparison with the solution of the one-dimensional time-dependent Schrödinger equation (TDSE) [33].

For small Keldysh parameters, Eqn. 1.47 can be approximated by Zener-like exponential tunneling

$$\Gamma_{Zener} = \frac{e|E_L|a}{2\pi\hbar}\exp\left[-\frac{\pi}{2}\frac{m^{1/2}\Delta_g^{3/2}}{e\hbar|E_L|}\right]\ . \tag{1.48}$$

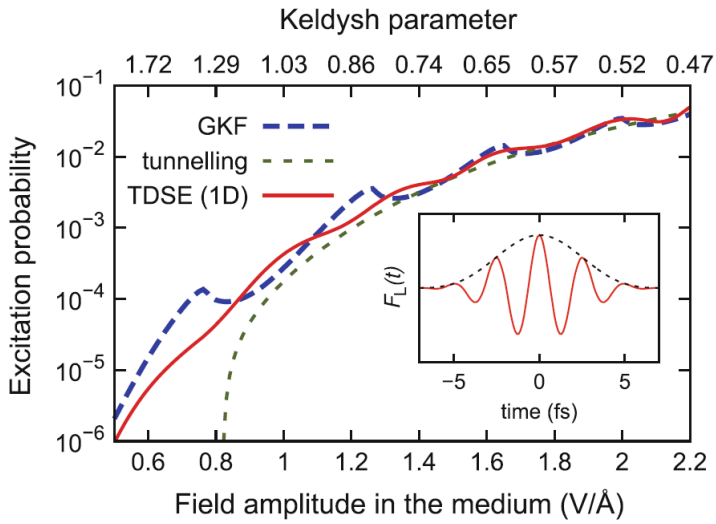

Figure 1.7: Generalized Keldysh Ionization Rate. The excitation probability calculated with the generalized Keldysh formula is in good agreement with the one-dimensional TDSE. The approximation of the excitation probability with a tunneling rate is reasonable for $\gamma_K > 1$. With permission of Springer [33].

The prefactor of the exponential function is very sensitive to the exact approximations made and has yielded slightly different results in publications from Zener [42], Kane [43], and Keldysh [41]. A direct extraction of this parameter from experimental data has — to the knowledge of the author — not been possible so far.

For ultrashort laser pulses, dielectric media can sustain electric field strengths far beyond the DC damage threshold [7]. Therefore, the previously unexplored field of strong-field phenomena in light-matter interaction can be investigated. One interesting finding in this regime is the generation and detection of optical-field-induced currents, which is further elucidated in the last section of this chapter after introducing some basic principles on charge carrier transport in solids.

1.3 Transport of Photoexcited Carriers in Solids

In order to get a better understanding of the strong-field-induced currents, we first have to look into the fundamental principles which govern the transport of photoexcited charge carriers in solids. Only the very basics of the vast topic of charge carrier transport is discussed in this section and the reader is referred to standard solid-state textbooks [44, 45] for further details. A nice overview on pioneering experiments investigating the charge carrier dynamics in semiconductors and the underlying physical principles can be found in [46, 47].

An electron in a crystal can be described as a wave packet which results from a su-

perposition of Bloch waves. Its velocity is given by the group velocity of the wave packet which depends on the band dispersion $E(k)$ [45]:

$$\mathbf{v}(\mathbf{k}) = \nabla_{\mathbf{k}}\omega(\mathbf{k}) = \frac{1}{\hbar}\nabla_{\mathbf{k}}E(\mathbf{k}) \ . \tag{1.49}$$

To describe its motion through the band structure of the solid, we will stick to the semi-classical picture. When an electric field is applied to a solid, electrons in the conduction band are accelerated according to the acceleration theorem

$$\hbar\frac{\mathrm{d}\mathbf{k}(t)}{\mathrm{d}t} = -e\mathbf{E}_L(t) \ , \tag{1.50}$$

$$\mathbf{k}(t) = -\mathbf{k_0} - \frac{e}{\hbar}\mathbf{A}_L(t) \ , \tag{1.51}$$

where $\mathbf{k}(t)$ is the time-dependent crystal momentum of the electron, $\mathbf{k}_0$ its initial crystal momentum prior to interaction, and $\mathbf{A}_L(t)$ the vector potential of the laser pulse. The heavy holes are assumed to be localized due to the flat hole band dispersion of most dielectric materials. Introducing the effective mass m_{eff} as

$$m_{eff} = \frac{\hbar^2}{\mathrm{d}^2E/\,\mathrm{d}k^2} \tag{1.52}$$

allows to bring Eqn. 1.50 to the same form as Newton's second law:

$$\frac{\mathrm{d}\mathbf{v}(t)}{\mathrm{d}t} = -\frac{e}{m_{eff}}\mathbf{E}_L(t) \ . \tag{1.53}$$

The scalar notation of m_{eff} assumes that the dispersion relation is isotropic in k-space. If this assumption does not hold, the effective mass has to be treated as a tensor.

When the electron is accelerated towards the end of the Brillouin zone ($|k| = \pi/a$), its momentum is reversed in case it cannot escape to another band by tunneling. In other words: The electron wave packet is Bragg reflected. This leads to oscillations in real space with the Bloch frequency ω_B [48]:

$$\omega_B = \frac{eE_La}{\hbar} \ , \tag{1.54}$$

where a is the lattice constant of the crystal. If the driving field oscillates at frequency ω_L, the minimum externally applied field strength E_B to accelerate the charge carriers to the end of the Brillouin zone is

$$E_B = \epsilon_r(\omega)\frac{\pi\hbar\omega_L}{ea} \ , \tag{1.55}$$

where $\epsilon_r = 1 + \chi^{(1)}$ is the relative permittivity which represents the linear screening of the field inside the sample.

However, these oscillations can only be observed if no scattering takes place before the charge carriers have completed one oscillation cycle. Charge carriers can scatter due to interactions between each other or due to interactions with lattice distortions. These distortions can either be permanent, due to defects and impurities, or dynamic due to vibrations (phonons). For the lattice constant of α-quartz, which is 0.5 nm, a high DC voltage of 1×10^6 V/m would lead to an oscillation period of 8 ps which is much longer than the typical electron-phonon scattering times of a few femtoseconds. That is why, until recently, Bloch oscillations had been considered without significance to the electron dynamics in a natural solid. The condition $2\pi/\omega_B < \tau_{scatter}$ had only been achieved in artificial systems, like superlattices [49, 50, 51], optical lattices [52], Josephson junction arrays [53], or optic waveguide arrays [54, 55].

A classical approach to describing the charge transfer in a solid state system under the consideration of scattering is the Drude model [56]. Despite its simplicity it has been successfully applied to describe the frequency-dependent conductivity of a large range of materials [57].

$$m\frac{\mathrm{d}\mathbf{v}(t)}{\mathrm{d}t} + \frac{m}{\tau}\mathbf{v}(t) = -e\mathbf{E}_L(t) \ , \tag{1.56}$$

where the second term on the left side represents friction due to a finite relaxation time τ, which comprises all of the above mentioned scattering mechanisms. In the stationary case $\mathrm{d}v/\,\mathrm{d}t = 0$, this leads to a proportionality between the drift velocity, and thus the current density, and the electric field. This is the well-known ohmic transport. In case τ is large with respect to the observed time scales, the charge carriers are accelerated according to Eqn. 1.53. This regime is known as ballistic transport.

The solution of Eqn. 1.56 of the position $\mathbf{x}(t) = \int \mathbf{v}(t')\,\mathrm{d}t'$ for carriers that are injected into the conduction band at a time t_0, for example by photoexcitation, yields

$$\mathbf{x}_{t_0}(t) = -\frac{e}{m}\int_{t_0}^{t} \mathrm{d}t' \exp\left(-\frac{t'-t_0}{\tau}\right) \int_{t_0}^{t'} \mathrm{d}t''\mathbf{E}_L(t'') \cdot \exp\left(\frac{t''-t_0}{\tau}\right) \ . \tag{1.57}$$

For the ballistic case with $\tau \to \infty$, the above equation simplifies to

$$\mathbf{x}^b_{t_0}(t) = -\frac{e}{m}\left(\boldsymbol{\alpha}(t) - \boldsymbol{\alpha}(t_0) - \mathbf{A}(t_0)\cdot(t-t_0)\right) \ , \tag{1.58}$$

where the vector potential $\mathbf{A}(t)$ is the primitive integral of the driving field $\mathbf{E}_L(t)$ and $\boldsymbol{\alpha}(t)$ is the primitive integral of $\mathbf{A}(t)$. In the ohmic case, the result is

$$\mathbf{x}^o_{t_0}(t) = -\frac{e\tau}{m}\left(\mathbf{A}(t) - \mathbf{A}(t_0)\right) \ . \tag{1.59}$$

The charge separation in the ohmic case is clearly dominated by the vector potential while in the case of ballistic transport, both the vector potential and its primitive integral enter the equation. The validity of the Drude model in the case of optical-field-induced currents is discussed in Section 5.4.

After photoexcitation, there are four regimes of carrier relaxation [46]:

1. During the coherent regime, the excited carriers maintain a well-defined phase relation with among each other and with respect to the light field. It is equivalent to the above mentioned ballistic regime.

2. After the coherence is destroyed by scattering processes, a non-thermal charge carrier distribution prevails.

3. Eventually, the energy of the charge carriers gets redistributed by electron-electron scattering and their distribution can be characterized by a temperature which is higher than the lattice temperature. This is the hot-carrier regime.

4. The hot carriers gradually transfer energy to the lattice until an equilibrium is reached in the isothermal regime. The excess electrons will recombine radiatively or non-radiatively.

The regimes cannot be strictly separated — they overlap temporally. Their respective time scales range from a few femtoseconds for the loss of coherence to several 100 ps for the recombination. The exact rates depend among others on the charge carrier density, lattice temperature, and the band structure [46]. They can be theoretically investigated by modeling the evolution of the momentum distribution of excited charge carriers by the Boltzmann transport equation [58]. Experimentally, the short time scales of the initial relaxation steps are not easily accessible but recent experiments suggest that in the case of strong-field excited charge carriers in SiO_2, the decoherence time is on the order of 3 fs [59].

For applied field strengths in the range of a few 1×10^{10} volts per meter, the Bloch period lies in the same, few femtoseconds range, which opens exciting possibilities. In 2009, partial Bloch oscillations were for the first time observed in GaAs [60]. Furthermore, they have been proposed as the mechanism behind the emission of high harmonics from bulk which have been observed lately [8, 9]. However, semiclassical simulations comparing the experimental scaling of high-harmonic signal with intensity revealed the central role of spatial conduction band harmonics in the high-harmonic generation (HHG) process [10]. Recent time-resolved measurements in combination with quantum-mechanical modeling [61] now suggest that the emission of high energetic photons results from a delicate interplay between inter- and intraband dynamics.

Another strong-field phenomenon which results from combined inter- and intraband dynamics is the generation of optical-field-induced currents. They will further be investigated in the following.

1.4 Optical-Field-Induced Currents

When a strong laser field on the order of a few 1×10^{10} volts per meter is applied to a dielectric sample, a current is induced on the time scale of half an oscillation cycle. These currents were for the first time demonstrated by Schiffrin et al. [4]. Shortly after, their

application for the CEP characterization of the excitation pulse was demonstrated [62]. In the underlying nonperturbative strong-field process, charge carriers are promoted into the conduction band by interband absorption and subsequently accelerated in order to generate a measurable current. There are two potential implementations using either a single few-cycle pulse or two pulse replica with crossed polarizations which are temporally delayed with respect to each other. The details of the experimental setup is given in Section 4.2. This section will briefly recapitulate the fundamental findings from the pioneering experiment [4] and present the different theoretical approaches for modeling them.

The two basic experimental configurations which have been employed in the generation of ultrafast currents are indicated in Fig. 1.8. In the one-pulse-scheme, currents on the scale of a few picoamperes are generated by focusing a CEP-stable 4 fs pulse at 760 nm central wavelength onto a dielectric nanogap between two gold electrodes [63]. The measured current amplitude can be translated into a transferred charge $Q = J/f_{rep}$ of up to 10 000 electrons per pulse at a repetition rate of 3 kHz. Varying the CEP of the laser pulse by scanning the insertion of a fused silica wedge pair, shows that the measured current is strongly phase dependent.

By using the two-pulse-scheme, a strong pulse polarized along the electrode gap injects the charge carriers into the conduction band (injection pulse) while a delayed, about 10 times weaker pulse drives the delocalized carriers towards the electrodes (drive pulse). None of the two pulses generates a current by itself, so the signal is recorded in the temporal overlap region only. Since the measured current features the same oscillation period as the drive field pulse, the duration of the injection needs to be confined to less than one half-cycle of the electric field which is about 1.3 fs for the central wavelength of 760 nm. The conductivity of the sample during this time window is increased by 18 orders of magnitude. The experimental findings are summarized in Fig. 1.9.

There are different theoretical approaches to describe the experimental data [33]: the semiclassical model, the interfering multi-photon absorption pathways, adiabatic semimetalization, and ab-initio calculations. The different approaches can be seen as complimentary because they highlight different aspects of the generation and detection of the optical-field-induced currents. All the models have in common that they consider the microscopic current density $j(t)$ whose time integral leads to a polarization density $p(t)$. The latter is equivalent to a charge density $q(t)$:

$$q(t) = p(t) = \int_{-\infty}^{t} j(t')\,\mathrm{d}t' \ . \tag{1.60}$$

The measured transferred charge per pulse Q follows the microscopic $q(t)$ after the excitation at t_0 is concluded:

$$Q = A_{eff} q(t > t_0) \ , \tag{1.61}$$

where A_{eff} is an effective cross section that depends on the details of the metal-dielectric junction.

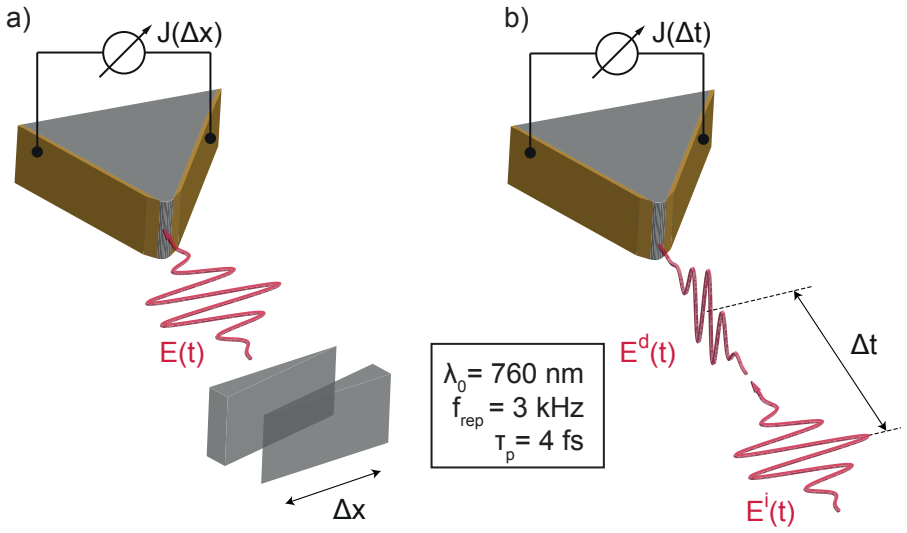

Figure 1.8: Schematic Optical-Field-Induced Current Setup. 4 fs pulses at 760 nm central wavelength and 3 kHz repetition rate induce a current in a fused silica nanogap between two gold electrodes. a) In the one-pulse-scheme, a single pulse is used to generate the current. Its CEP is varied by changing the insertion of a pair of fused silica wedges Δx. b) In the two-pulse-scheme, a strong injection and a weak drive pulse with an adjustable temporal delay are used. The polarization of the injection arm is oriented along the gap while the one of the drive arm is oriented across. There is only a measurable signal in the temporal overlap region. Adapted from [63].

1.4.1 Semiclassical Model

The semiclassical model provides a descriptive physical picture of the current generation in the form of a two-step process: the interband tunneling or multi-photon absorption which launches an electron wave packet in the conduction band and its subsequent acceleration towards the metal electrodes. This picture corresponds well to the experimental findings in the two-arm configuration [4] where the injection pulse takes care of the first step and the drive pulse of the second.

Once the electron packet is launched in the conduction band, it is accelerated in the potential of the band following the acceleration theorem, introduced in Eqn. 1.50. A rigorous treatment of the injection and drive process leads to a current density of the form [33]

$$\mathbf{j}_{\mathbf{k_0}}(t) = -e \sum_i |\alpha_{i,\mathbf{k_0}}(t)|^2 \mathbf{v}_i(\mathbf{k}(t)) - \mathbf{j}_{interband}(t) \ , \tag{1.62}$$

where $|\alpha_{i,\mathbf{k_0}}(t)|^2$ is the probability to find the electron in a particular band i with momentum $\mathbf{k}_0$ and $\mathbf{v}_i(\mathbf{k}) = \nabla_k \mathbb{E}_i(\mathbf{k})/\hbar$ is the velocity which is calculated from the dispersion relation $\mathbb{E}_i(\mathbf{k})$ of the band. The last term on the right hand side corresponds to the current contribution due to interband coherences which depend on the momentum matrix elements

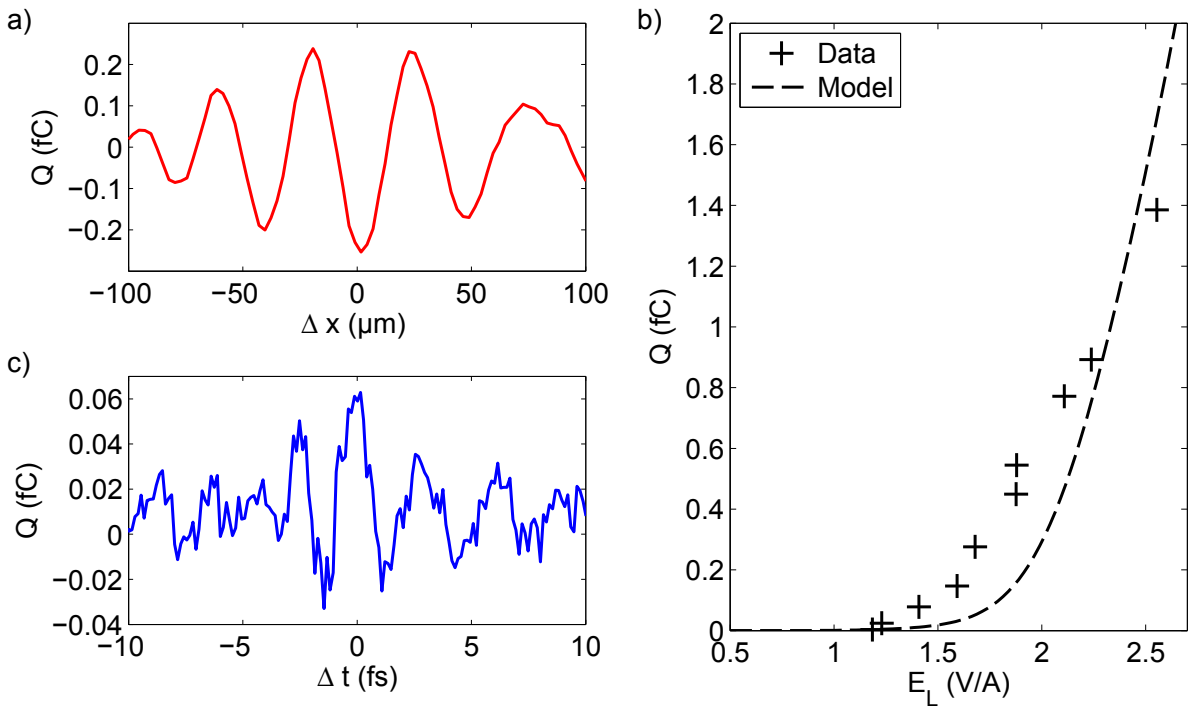

Figure 1.9: Previous Optical-Field-Induced Current Results. a) Transferred charge induced by a single laser pulse in dependence of the wedge position Δx. b) Scaling of the transferred charge with the applied field strength E_L in the one-pulse-scheme (crosses), compared to a adiabatic semimetalization model (dashed line). c) Transferred charge generated by the interplay of a strong injection and a weak drive pulse with crossed polarizations in dependence of their relative time delay Δt. Data from [63, 4]
.

between valence and conduction band. It is small compared to the first term representing the intraband transport of the charge carriers [64].

In numerical simulations, a scaling of the current with field strength at low intensity was investigated [65]. It was determined to be E^{2n+1} with the multi-photon absorption order n. This scaling can very intuitively be interpreted in the semiclassical picture: The intensity of n photons is needed for the injection of the charge carrier. Then the electric field of one more photon is needed for the drive process, summing up to $2n + 1$. A comparison of the semiclassical approach to more sophisticated numerical methods can be found in [66].

1.4.2 Interfering Multi-Photon-Absorption Pathways

For moderate intensities, modeling the laser-induced current as a result of interfering multi-photon pathways reproduces the experimental findings well [65]. This approach directly follows up on pioneering experiments using one- and two-photon absorption in GaAs to

generate phase-dependent currents [67, 68, 69], where the wavelength of the excitation is tuned such that $\Delta_g(GaAs) = 2\hbar\omega_L = \hbar\omega_{SHG}$. Since the initial and final state of the process for the absorption of one and two photons are degenerate, the two quantum-mechanical pathways can interfere. Due to the different $-\mathbf{k}/\mathbf{k}$-symmetry for odd and even multi-photon orders, their interference leads to an asymmetric momentum distribution in the excited state population. As a result, adjusting the phase $\Delta\varphi$ between the fundamental field and the second harmonic can sensitively control the magnitude of the current which is proportional to the velocity of the excited charge carriers. These coherent-control experiments were repeated for other semiconductors [70], molecular wires [71], carbon nanotubes [72], and graphene [73].

In case of the broad bandwidth pulse used in [4, 62] as well as in this work, the different wavelengths corresponding to different multi-photon orders are present in one single waveform. Adjusting the CEP of this pulse can similarly lead to an asymmetry in the momentum distribution in the conduction band. This has been shown in a density matrix approach, solved self-consistently with equations for the macroscopic electric field inside the medium [65].

Regarding the current signal scaling, the interfering multi-photon absorption pathways can also give an intuitive explanation for the E^{2n+1} finding: The total excitation probability is given by the product of two interfering absorption probabilities. In the case of N and $N+1$ photon absorption, which correspond to absorption directly at and slightly above the band gap, respectively, these are proportional to $E^n E^{n+1} = E^{2n+1}$.

The latest results from strong-field attosecond polarization spectroscopy in fused silica under comparable experimental conditions suggest that the polarization response can be described in terms of six-photon absorption [35].

1.4.3 Adiabatic Semimetalization

In the adiabatic semimetalization picture, Wannier-Stark states are used in order to explain the generation of ultrafast currents [33]. The term was coined for the behavior of dielectric nanofilms [74, 75] in a strong electric field. Simulations show that a transient strong field can alter the optical properties of the films, significantly and reversably, to such a degree that the dielectric constant becomes negative, which is typically associated with metals. The conductivity at optical frequencies can reach levels comparable to those of semimetals.

This behavior is explained in terms of Wannier-Stark states which form a basis set for the Wannier-Bloch states. The latter are solutions of the stationary Schrödinger equation in the length gauge [76]:

$$\left(\frac{\hat{p}}{2m} + U(z) + eE_L z\right)\Psi = \mathbb{E}\psi \ , \tag{1.63}$$

where $\hat{p}$ is the momentum operator, $U(z)$ the lattice potential, and E_L the applied laser field. Restricting the electron dynamics to a single band gives the solution

$$\Psi_i = b_i\left(z, k_0 - \frac{eE_L}{\hbar}t\right)\exp\left[-\frac{i}{\hbar}\int \mathbb{E}_i\left(k_0 - \frac{eE_L}{\hbar}t'\right)\mathrm{d}t'\right] \ , \tag{1.64}$$

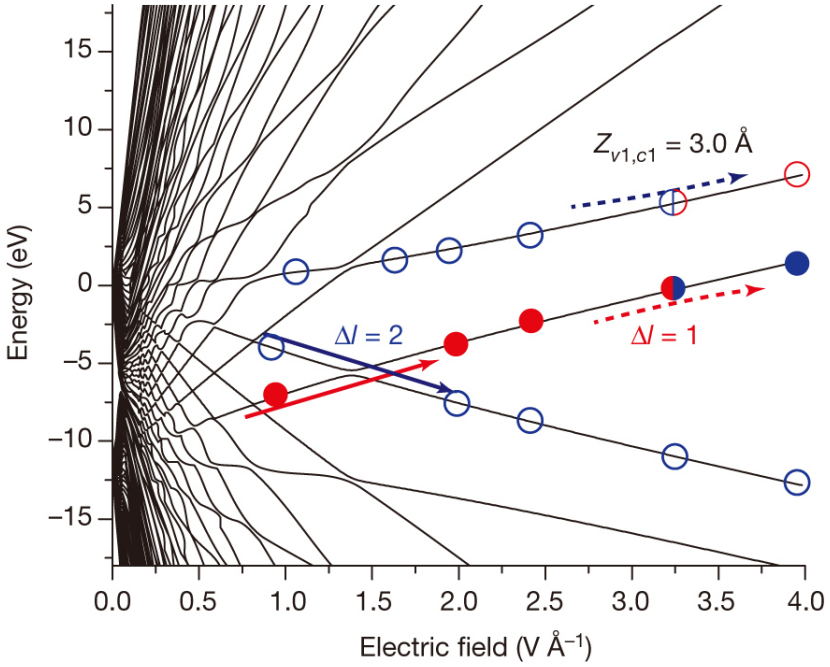

Figure 1.10: Formation of Wannier Stark Ladder at Strong Electric Fields. Red circles indicate valence band wave functions, blue circles conduction band wave functions. Full circles stand for occupied, empty circles for vacant states. The anticrossings at $\Delta l = 1$ and $\Delta l = 2$ are shown with arrows denoting a diabatic (solid) and an adiabatic crossing (dashed). Reprinted by permission from Macmillan Publishers Ltd: Nature [78], copyright (2014).

where Ψ_i is the Wannier-Bloch state, $\mathbb{E}_i$ the respective energy level, and $b_i(z,k)$ is an auxiliary function satisfying the periodic boundary conditions in the reciprocal space of the lattice. The localized Wannier-Stark states $\Psi_{i,l}^{WS}(z)$ can be defined [77] via

$$\Psi_i(z,t) = \sum_l \Psi_{i,l}^{WS}(z) \exp\left[-\frac{i}{\hbar}\mathbb{E}_{i,l}^{WS}\right] \ , \tag{1.65}$$

where l is the lattice site on which the Wannier-Stark state is localized. The energies associated with these states form the so-called Wannier-Stark ladder

$$\mathbb{E}_i^{WS} = \mathbb{E}_i + leaE_L \ , \tag{1.66}$$

where a the lattice constant, and $\mathbb{E}_{i,l} = \frac{\pi}{2a}\int_{-\pi/2}^{\pi/2} \mathbb{E}_i(k)\,\mathrm{d}k$. The spacing between neighboring ladder states corresponds to $\hbar$ times the Bloch frequency. For our purposes this description of the Wannier-Stark states is sufficient. For their more sophisticated treatment as resonances with a finite lifetime, the reader is referred to [33].

If a strong electric field is applied to a dielectric, the fanned out energy levels of valence and conduction band can get close to each other and form an avoided crossing, see Fig. 1.10.

Since the Wannier-Stark states are highly localized, the probability that an electron from the valence band passes the avoided crossing adiabatically and occupies a conduction band state, depends on the distance of the sites which form the avoided crossing. In simulations of SiO_2, the nearest neighbors ($\Delta l = 1$) form an anticrossing above the experimentally tested damage threshold reachable in experiments with our laser parameters of $(2.6 \pm 0.5)\,\mathrm{V/Å}$ [79]. However, there is also a non-zero probability for an adiabatic passage between states at sites with $\Delta l = 2$ which occurs at $E_L = 1.5\,\mathrm{V/Å}$. This field strength is readily reached experimentally [4].

The simulated conduction band population peaks during the strongest half-cycle of the applied electric field and is much larger than the residual population which remains after the pulse. This is in contrast to the strong-field excitation in atoms where the number of excited electrons increases in a step like fashion and the resulting plasma density stays constant after the pulse is gone [80]. The population density that is only present during the interaction with the strong field is attributed to so-called virtual carriers. The virtual carriers lead to an increased polarizability of the system at optical frequencies [81, 82, 83] which can explain the current formation. In the linear regime, virtual and real carriers can be distinguished by detecting radiated waveforms in terahertz spectroscopy [84] while tuning the excitation energy above and below the resonant condition. However, the experiments with field-induced currents do not allow a distinction between real and virtual carriers but the observation of strong-field-induced changes in reflectivity support the adiabatic semimetalization picture [1] and recent experiments with attosecond polarization spectroscopy [35] can resolve virtual and real excitation densities.

1.4.4 Ab-Initio Simulations

The ab-initio simulations of ultrafast currents based on time-dependent density functional theory can provide insight into the excitation dynamics on the atomic scale. Simulations for crystalline SiO_2 (α-quartz) have been performed by Wachter el al. [85]. As has been shown in [4], the behavior of crystalline quartz and fused silica is similar in experiments. In contrast to dissipative processes such as electron-phonon and defect scattering, elastic-scattering is self-consistently included in the calculations.

For small intensities of $5 \times 10^{12}\,\mathrm{W/cm^2}$, the polarization density $p(t)$, which is calculated from the current density as shown in Eqn. 1.60, follows adiabatically the applied field. This is characteristic of a linear response. After the pulse, there is a small residual polarization density overlaid with quantum beats, see in Fig. 1.11. Spatially as depicted in Fig. 1.12, the current density is localized at the oxygen atom, which resembles an atomic-like excitation. In the case of higher intensities at $2 \times 10^{14}\,\mathrm{W/cm^2}$, the current density is delocalized along the Si-O-Si bond axis, which indicates a population of the conduction band levels. The residual polarization density after excitation is orders of magnitude larger than in the low intensity case.

The calculated transferred charge agrees very well with the experimental findings in [4] for more than two orders of magnitude in laser intensity. The simulations furthermore predict two effects which have not experimentally been observed yet: Firstly, there is a

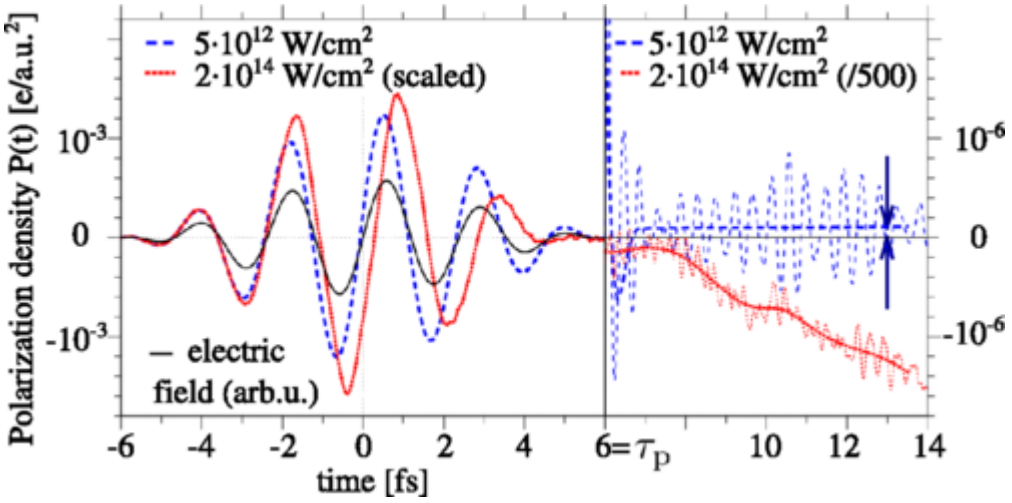

Figure 1.11: Time-Dependent Polarization Response to Strong-Field Excitation in SiO_2. Polarization density shown along the laser polarization direction for two different intensities compared to the electric field. The thick lines depict the temporal average over fast oscillations (thin lines). Reprinted figure with permission from [85]. Copyright (2014) by the American Physical Society. `http://dx.doi.org/10.1103/PhysRevLett.113.087401`

phase shift of the CEP dependent current which depends on the orientation of the crystal axis towards the laser polarization. Secondly, the simulations show a constant transferred charge offset independent of the CEP when the laser polarization is aligned along the a-axis of the crystal. This would allow for the measurement of optical-field-induced currents without a CEP-stabilized laser.

The ab-initio results support the picture of adiabatic semimetalization presented in the previous subsection only at intermediate fields where the calculated field-induced alternating-current (AC) conductivity at the fundamental laser frequency $\sigma(\omega_L)$ reversibly increases by more than 20 orders of magnitude during the laser-matter interaction. Above $5 \times 10^{13}\,\mathrm{W/cm^2}$ however, the ab-initio simulations show that nonadiabatic excitation leads to ballistic currents which dominate the transferred charge. As was mentioned in the previous subsection, virtual (adiabatic) and real (nonadiabatic) population could not yet been distinguished experimentally.

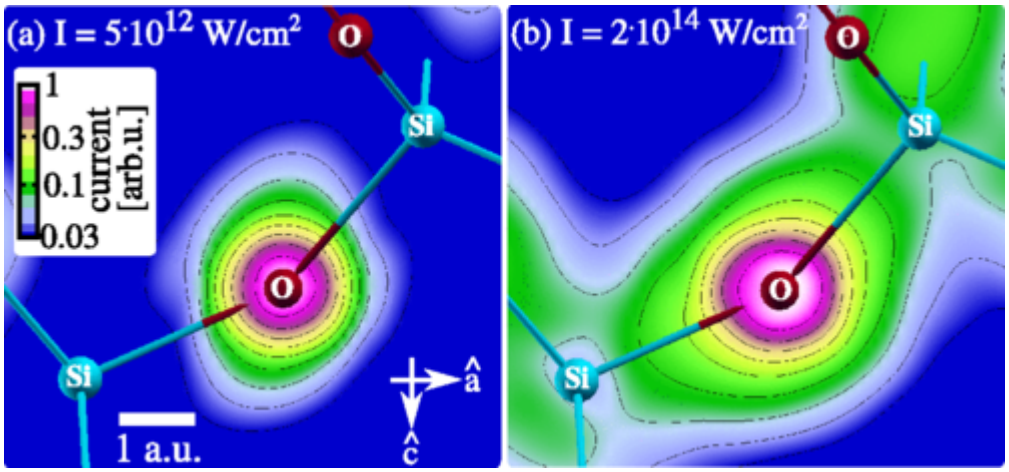

Figure 1.12: Time-Averaged Field-Induced Current Density in SiO_2. The current density is shown in the a-c-plane for two different intensities. The laser is polarized in c-direction. Reprinted figure with permission from [85]. Copyright (2014) by the American Physical Society. `http://dx.doi.org/10.1103/PhysRevLett.113.087401`

Chapter 2

Experimental Tools

This chapter presents the experimental tools which are widely used in ultrafast measurements in general and provide the basis for this work in particular. The first section introduces popular pulse characterization techniques. Besides describing the metrology schemes employed in this thesis, Section 2.1 also gives an overview of state-of-the-art characterization techniques, their potential and their limitations. This serves as benchmarks for the measurement schemes in Chapter 3 and Chapter 5. The phase-stable near-infrared (NIR) laser presented in Subsection 2.2.1 was used in previous experiments on ultrafast currents in solids [4, 62, 63] and is employed in this work in order to investigate some geometrical and material-related effects, summarized in Chapter 4. The SWIR source described in Subsection 2.2.2 was developed by Dr. Alexander Schwarz and others [38]. The further advancements realized in the course of this dissertation have facilitated its applications in experiments and made it the backbone of the interferometric setup described in Section 2.3. This interferometer combines sub-two-cycle visible/NIR and SWIR fields in a pump-probe-like scheme. It was built in order to facilitate the experiments presented in Chapter 3 and Chapter 5.

2.1 Ultrafast Pulse Characterization

The knowledge of the spectral and temporal characteristics of ultrashort laser pulses is essential for their optimization and use in experiments. It not only facilitates the compression or well-defined shaping of the waveforms, it also provides an insight into the polarization response of a system during light-matter interaction. This section recapitulates some of the most commonly used pulse characterization techniques for few-cycle pulses in the visible and infrared range.

2.1.1 Measurement of Spectral Amplitude and Phase

The main problem in measuring ultrashort pulses is that their temporal evolution is faster than the response time of conventional electronic devices. Therefore, they have to be

measured with optical techniques while using a relatively slow electronic detector [86].

One of the most popular techniques for measuring the amplitude and phase of an ultrashort pulse is frequency-resolved optical gating (FROG) [87]. FROG is a technique with multiple geometric variations which works in the hybrid time-frequency domain [20]. In its simplest form it is based on an autocorrelation measurement where the unknown electric test field $E(t)$ is overlapped with a time-delayed gate $g(t-\tau)$ in a nonlinear medium. The resulting nonlinear delay-dependent signal is spectrally resolved and forms a so-called spectrogram or FROG trace

$$I_{FROG} = \left| \int_{-\infty}^{\infty} E(t) g(t-\tau) \exp(-i\omega t)\, \mathrm{d}t \right|^2 . \tag{2.1}$$

In order to extract the electric field $E(t)$ from I_{FROG}, a two-dimensional phase-retrieval problem has to be solved [88]. This mathematical problem is well known and has an essentially unique solution (for details, see [20]). For a given experimentally recorded FROG trace, the exact shape of the electric field can be reconstructed, except for two parameters which remain unknown: the absolute time zero and the CEP.

There are numerous different FROG geometries and four of them are employed over the course of this work: SHG, third-harmonic (THG), transient-grating (TG), and cross-correlation FROG (XFROG), whose FROG traces take the following forms:

$$I_{FROG}^{SHG} = \left| \int_{-\infty}^{\infty} E(t) E(t-\tau) \exp(-i\omega t)\, \mathrm{d}t \right|^2 , \tag{2.2}$$

$$I_{FROG}^{THG} = \left| \int_{-\infty}^{\infty} E^2(t) E(t-\tau) \exp(-i\omega t)\, \mathrm{d}t \right|^2 , \tag{2.3}$$

$$I_{FROG}^{TG} = \left| \int_{-\infty}^{\infty} E^2(t) E^*(t-\tau) \exp(-i\omega t)\, \mathrm{d}t \right|^2 , \tag{2.4}$$

$$I_{XFROG}^{SFG} = \left| \int_{-\infty}^{\infty} E(t) E_{ref}(t-\tau) \exp(-i\omega t)\, \mathrm{d}t \right|^2 , \tag{2.5}$$

where E_{ref} is a known reference field. There are several advantages and disadvantages to these FROG geometries [20].

- SHG FROG: The test pulse and its replica are overlapped in a SFG crystal. Due to the low order $\chi^{(2)}$ nonlinearity involved, the sensitivity of this FROG geometry is high compared to $\chi^{(3)}$ techniques: The setup is simple since it only involves two pulses. The signal can be filtered spectrally and in terms of polarization to improve the signal-to-noise ratio. However, the FROG traces show a symmetry with respect to time reversal, which lead to a temporal ambiguity of the retrieved electric field. Furthermore, the phase-matching bandwidth is limited and depends on the length of the nonlinear crystal. The SHG FROG was used for the definition of the design targets of the chirped mirror compressor for the visible/NIR arm of the interferometer in Section 2.3.

- THG FROG: The setup is the same as for the SHG FROG but the sensitivity is lower since a $\chi^{(3)}$ nonlinear crystal is used for THG. This technique is suitable for SWIR pulses, whose spectrum can be shifted towards the sensitivity range of silicon spectrometers. Thus, the THG FROG can be used for characterizing the SWIR source, see Subsection 2.2.2.

- TG FROG: This FROG implementation involves three input beams and one output beam in noncollinear geometry, which makes the setup slightly more complex. Two pulses are spatially and temporally overlapped to produce a grating via the $\chi^{(3)}$ Kerr nonlinearity of the used medium. The third, delayed beam is diffracted of this grating to form the signal beam. This FROG implementation is especially suited for ultrashort pulses because there are no transmissive optics and no phase-matching bandwidth limitation.

- SFG XFROG: If a well-characterized reference beam is available, it can be overlapped with the unknown test pulse in a SFG crystal. This technique is especially beneficial if the test pulse is weak or temporally stretched since the signal can be scaled by making the reference stronger. Depending on the spectrum of the reference pulse, it can also increase phase-matching bandwidth compared to SHG FROG. In principle any $\chi^{(2)}$ or $\chi^{(3)}$ nonlinearity can be used for XFROG.

An alternative approach is the spectral phase interferometry for direct electric-field reconstruction (SPIDER). It uses the interference of the test field with its replica and a strongly stretched pulse [89]. The experimental setup is more complex than FROG but the analysis is easier since the retrieval algorithm is not iterative. There are variants of both SPIDER and FROG which allow for single-shot measurements. We will not further discuss SPIDER since it is not used in this work.

Neither of the techniques presented in this subsection are sensitive to the CEP of the pulse. However, it has been demonstrated that a combination of FROG with a CEP-sensitive technique can provide this missing information [90].

2.1.2 Measurement of Carrier Envelope Phase

As mentioned in the previous subsection, typical pulse characterization techniques like FROG and SPIDER do not provide information on the CEP of an ultrashort pulse. In order to access this important quantity, different experimental approaches are needed. Two types of CEP measurements are presented in the following: Firstly, we introduce interferometric techniques which characterize the relative CEP in terms of the carrier offset frequency by analyzing the beating between the octave-spanning spectrum of the fundamental beam and its harmonic. Secondly, we discuss techniques for characterizing the absolute CEP which make use of highly nonlinear or nonperturbative processes. If the recorded observables show an asymmetry with respect to the direction of the electric-field, it can be related to the absolute CEP of the few-cycle pulse.

Relative CEP Measurements The measurement and stabilization of the carrier-envelope offset frequency has lead to the realization of stable frequency combs [91, 92] for which John L. Hall and Theodor W. Hänsch were jointly awarded 50 % of the Nobel Prize in Physics 2005. Beyond the applications of these lasers in precision spectroscopy and atomic clocks [93], ultrafast and strong-field science has largely benefited from the availability of phase-stable pulses [94].

The self-referencing technique [21], which is now routinely applied for f_{CEO} characterization and stabilization, is based on the detection of the beating of an octave-spanning spectrum with its 2nd (SHG) or 0th (OR) harmonic. The techniques are called f-2f and f-0f interferometry, respectively. In the case of the f-2f interferometer, the frequency of the interference signal between the fundamental mode $2m$ and the second harmonic mode m is equal to

$$2f(m) - f(2m) = (2mf_{rep} + 2f_{CEO}) - (2mf_{rep} + f_{CEO}) = f_{CEO} \ . \tag{2.6}$$

The same principle holds in the case of DFG in an f-0f interferometer. If the f_{CEO} is detected and locked to an external radio-frequency oscillator, the pulse train from an oscillator can be phase-stabilized by changing the dispersion of the cavity e.g. by modulating the pump laser intensity with an acousto-optical modulator. The self-referencing technique can be also be used for the characterization and stabilization of the CEP in an amplified pulse train [94], as shown in Subsection 2.2.1. Note that the f-2f and f-0f interferometers as well as other interferometric techniques [95, 96] facilitate the relative CEP detection but not the measurement off its absolute value.

Absolute CEP Measurements In order to measure the absolute CEP of a single pulse or a stabilized pulse train, a common approach is the utilization of strong-field effects which are CEP-sensitive. A routinely employed technique is the so-called Stereo ATI. It utilizes above threshold ionization (ATI) [97] in a gaseous medium. In ATI, the photoelectrons absorb more photons of the strong laser field than necessary for escaping the atom. This way, they can reach kinetic energies of up to tens of electron volts. Due to the spatial asymmetry of the transferred momentum in the field of a linearly polarized few-cycle pulse, the spectra of the photoelectrons show a left-right asymmetry parallel to the polarization of the laser pulse [98]. This asymmetry can directly be related to the carrier envelope phase of the pulse and can be used for single-shot CEP tagging [99]. The absolute value of the CEP is obtained by gauging the asymmetry map with the help of TDSE simulations.

Other strong-field approaches use the phase-sensitivity in HHG spectra [100] or optically induced currents [62] to extract φ_0. The underlying physics of the latter approach has been described in Section 1.4.

2.1.3 Full Electric Field Characterization

So far, none of the described techniques has been able to deliver complete and unambiguous information on the electric field of an ultrashort pulse. This subsection introduces

two techniques which have successfully recorded $E(t)$ in the time domain. Electro-optic sampling, a technique originally employed for field measurements the terahertz domain, is discussed in detail in Chapter 3.

In order to temporally resolve electric field oscillations of the test waveform, we need a gate or sampling pulse which is shorter than half its oscillation period. One mechanism in order to achieve such a short gate is HHG in gases. HHG is a process which leads to the emission of light bursts in the extreme ultraviolet (XUV) and soft x-ray regime with photon energies of a few tens of electron volt up to a few kilo electron volt [101]. An important energy scale of this process is the ponderomotive energy U_p which corresponds to the time averaged kinetic energy that a free electron with mass m acquires in a laser field of field strength E_L and angular frequency ω. It is given by [102]

$$U_p = \frac{e^2 E_L^2}{4m\omega^2} \ . \tag{2.7}$$

The resulting force pushes the electrons away from regions of high intensity.

For the scope of this work, we can disregard the quantum mechanical description of HHG [103] and stick with the intuitive simple man's model by Corkum et al. [104]. When an intense laser pulse ($U_p > I_p$, where I_p is the atomic ionization potential) with linear polarization is sent into a gas target, a three-step process takes place:

1. The strong laser field reduces the tunneling barrier for the electron which can escape the atom at every half cycle of the field oscillation.

2. The electron wave packet is accelerated in the laser field away from the ionic care. Once the electric field reverses sign, the electron is pushed back towards the parent ion.

3. With a certain probability, the electron recombines with its parent ion and releases its kinetic energy plus the ionization energy of the atom as an XUV burst.

Since potentially every half cycle can contribute to the emission and acceleration of the electrons, odd harmonics are visible in the XUV spectrum. However for ultrashort pulses with an appropriately chosen CEP, an unmodulated plateau in the cutoff region can be identified, which results from the acceleration of the electron in the strongest half cycle. Using a spectral filter in this region, a single isolated attosecond pulse can be extracted from the pulse train [16]. Other techniques for isolating a single attosecond pulse are polarization gating [105], ionization gating [106], or attosecond lighthouse [107]. Due to the strong temporal confinement of an isolated attosecond pulse, it can serve as a gate for the sampling schemes presented in the following.

The first technique is the attosecond streak camera. It was proposed and theoretically investigated by Itatani et al. [108] and successfully demonstrated for the measurement of an isolated attosecond pulse by Kienberger et al. [16]. When fundamental and XUV pulses are sent into a gas target, the electrons, which are freed by the XUV pulse, feel the electric field of the fundamental pulse. This leads to a delay-dependent modification of their kinetic

energy which can be detected by a time-of-flight spectrometer. The resulting spectrogram carries the information of the temporal structures of the fundamental and XUV pulse. The fundamental electric field can be retrieved from the streaking spectrograms by a retrieval algorithm similar to the one used for FROG traces [109]. The spectral cutoff is determined by the duration of the attosecond pulse which can be as low as 80 as [110].

Although a large variety of pulse shapes has been characterized with this technique [111], there are restrictions on the test waveform. The reason is that the highly nonlinear XUV generation process and the typically low XUV absorption cross sections of the streaking gas target lead to a small number of detected photoelectrons per laser shot. In streaking a high photon flux - typically on the order of 1×10^{11} photons/s [112] - is required such that the photon electron count is sufficient to fight the shot noise. Thus, strong few-cycle pulses with focus intensities on the order of $1 \times 10^{14}\,\mathrm{W/cm^2}$ are needed as a driver. For a detailed analysis on the influence of shot noise on the retrieval algorithm, see [113]. In addition, it needs to be considered that the test waveform undergoes considerable changes during the HHG process. The fundamental spectrum suffers a frequency shift due to the interaction with the free electrons in the gas target. This shift has been found to be substantial [114] and more sensitive to the focusing parameters of the fundamental beam than the HHG spectrum itself [115].

An alternative technique which does not rely on the detection of photoelectrons is the so-called petahertz optical oscilloscope [116]. Here, the electric field of the unknown ultrashort pulse is imprinted onto the deflection of the XUV beam generated by another pulse. This is possible by using the HHG process itself, or, more precisely, the electron excursion before recombination, as an attosecond gate. If the strong sampling pulse and the test pulse are overlapped in noncollinear geometry in a gas target, the test field modulates the electron trajectory during excursion and thereby changes the phase of the XUV pulse which leads to a measurable deflection of the XUV beam. This deflection is proportional to the time derivative of the electric field of the test pulse. A major advantage of this all-optical technique is that it requires only a low flux attosecond source and an XUV spectrometer. It also circumvents the above-mentioned reshaping of the test waveform by using a separate pulse for the HHG. The spectral cutoff of the petahertz optical oscilloscope determined by the excursion time of the freed electron. Theoretical estimation result in 200 nm as the lowest detectable wavelength. A single-shot scheme seems to be feasible but has not been demonstrated yet [116].

Both presented concepts for measuring the full electric field of ultrashort white-light and infrared pulses involve a complicated experimental apparatus and an XUV source. Attosecond streaking additional requires a photoelectron spectroscopy setup. To the knowledge of the author, neither of both schemes have so far been used to characterize SWIR to mid-infrared (MIR) optic parametric amplifiers like the one presented in Subsection 2.2.2. The unfavorable scaling of the HHG efficiency with increasing wavelength of the driving field is a major experimental complication (see Eqn. A.1). Appendix A introduces a SWIR attosecond beamline which is designed for the experimental implementation of HHG and streaking with a 2 µm light source, see Subsection 2.2.2.

2.2 Ultrafast Pulse Generation

Phase-stable few-laser pulses are the workhorse for studying the nonlinear to nonperturbative processes presented in later chapters. There are two common technique in producing ultrashort pulses that are able to reach the necessary intensities on the order of $1 \times 10^{14}\,\mathrm{W/cm^2}$: Ti:Sa-based amplifier systems and optical parametric amplifiers. This thesis makes use of both techniques for two different wavelength ranges.

2.2.1 Source of Phase-Stable Near-Infrared Waveforms

The phase-stable NIR waveforms are derived from a commercial Ti:Sa front end (Femtolasers) consisting of a CEP-stabilized Kerr-lens mode-locked oscillator and a multi-pass chirped-pulse amplifier (CPA). Fig. 2.2 shows a schematic outline of the laser. It delivers 23 fs pulses at a central wavelength of 780 nm and an output energy of 1 mJ at a repetition rate of 3 kHz. 5 % of this energy are split off for generating the seed for the SWIR laser, described in the next section. In order to achieve a sub-two-cycle pulse duration, spectral broadening and subsequent compression is needed. Therefore, the remaining 95 % of the pulse energy is focused into a 1 m long neon-filled hollow-core fiber (HCF) with an inner-core diameter of 250 µm, where the spectrum is broadened to more than an optical octave from about 450 nm to 950 nm via SPM and self-steepening [40], as discussed in Subsection 1.2.1. Fig. 2.1 shows the calibrated spectra before and after the HCF broadening. The resulting white-light pulses are compressed with a set of fused silica wedges

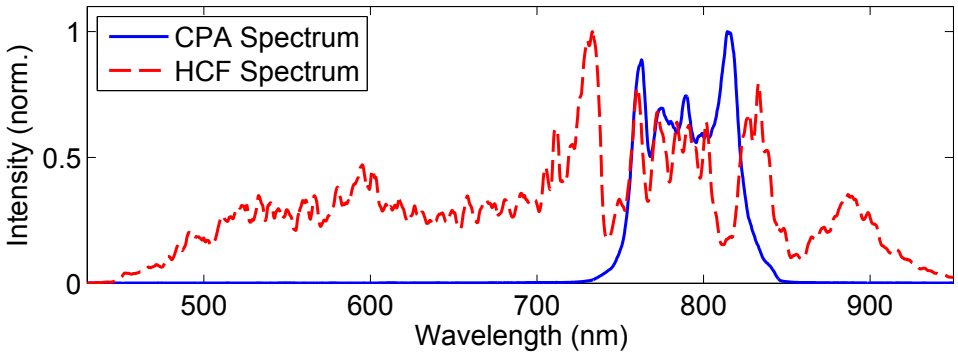

Figure 2.1: Broadened Near-Infrared Spectrum. Blue: Spectrum out of the multi-pass CPA. Red dashed: Broadened spectrum in the visible/NIR range after the HCF.

and a chirped mirror compressor to a sub-two-cycle pulse duration of about 4 fs at a pulse energy of about 500 µJ. To compensate for slow drifts in the CEP of the final pulse, less than 1 % of the power is picked up and sent to a f-2f interferometer (see Subsection 2.1.2) where the CEP drifts are measured. The feedback signal is applied to a piezo stage which changes the insertion of a wedged glass block in the stretcher of the multi-pass CPA to compensate the phase drifts accordingly. The resulting CEP stability is on the order of 150 mrad, averaged over 30 pulses.

During the course of this work, the oscillator was upgraded from a feed-back to a feed-forward CEP stabilized system [117] by the manufacturer. Moreover, an acousto-optic programmable dispersive filter (DAZZLER) was added in the stretcher and the prism compressor was replaced by a grating compressor in the multi-pass CPA. The performance of the system before and after the upgrade is similar but the upgrade allows for better dispersion control as well as more flexibility in modulating the carrier envelope phase which plays a central role in the experiments in Section 4.2. In the following, the front end is denoted front end system 1 before and front end system 2 after the upgrade.

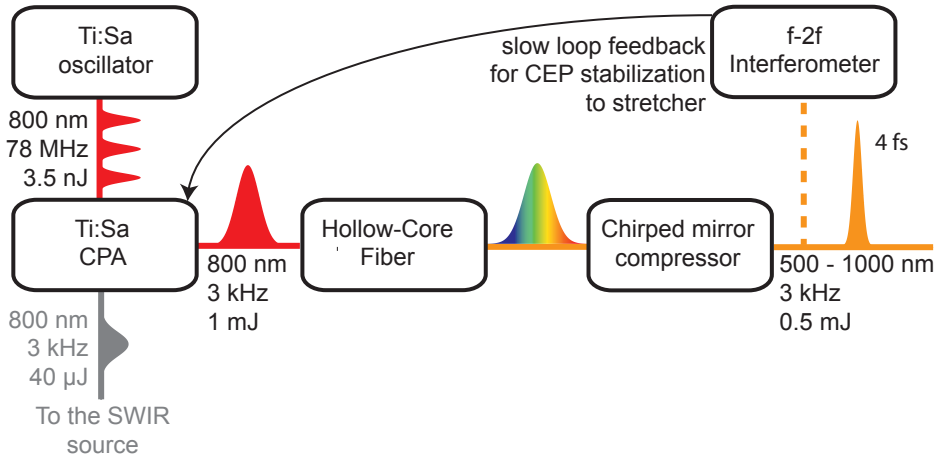

Figure 2.2: Near-Infrared Source. The Ti:Sa oscillator delivers phase-stable pulses which are amplified in a CPA at a repetition rate of 3 kHz. The 1 mJ pulses are further broadened in a HCF and compressed to sub-two optical cycles by chirped mirrors. An f-2f interferometer is used characterize slow CEP drifts which can be compensated in the stretcher of the Ti:Sa amplifier.

2.2.2 Source of Phase-Stable Short-Wavelength-Infrared Waveforms

For the generation of the SWIR waveforms, an optical parametric chirped pulse amplifier (OPCPA) is employed [118, 119]. OPCPA is based on a combination of CPA and OPA: A seed pulse is stretched, then amplified in one or several OPA stages, and subsequently compressed. These systems have several advantages over conventional amplifiers like the one described in the previous subsection:

- The single pass gain is very high, so in our case, three stages are sufficient to amplify the few nanojoule seed by six orders of magnitude.
- The amplified spectrum can either be narrow-band and tunable or very broadband, depending on the phase-matching conditions in the OPA crystals. In the latter

case, OPCPA can generate intense, few-cycle pulses without further broadening and subsequent compression steps.

- Since no energy is stored in the amplification crystals, the thermal load is limited. This makes OPCPA systems highly scalable in terms of amplified power.
- The amplification is confined to a finite time window during the interaction of seed and pump pulse, which leads to a high achievable temporal contrast compared to conventional laser amplifiers.

The setup of the degenerate OPCPA used for this work is to large parts equivalent to the one presented in [38, 120]. However, constant improvements, like a higher pulse energy stability of the pump laser at slightly lower output pulse energies and the availability of larger aperture OPA crystals, have lead to different operating parameters. The system is therefore briefly summarized below and schematically depicted in Fig. 2.3:

The seed and pump pulses of the OPCPA are derived from the same oscillator front end presented in the previous section ensuring optical synchronization. In addition, an active optical synchronization is employed to minimize timing drifts and jitter between the pump and the seed arm to about 24 fs. The details of this synchronization scheme can be found in [121].

Seed Generation The seed is generated via intrapulse DFG by focusing a 4 fs white-light pulse in a 500 µm β-barium borate (BBO) type II crystal (Castech). The broadband conversion efficiency in this simple collinear seed generation scheme can reach above 12 % for appropriately adjusted phase matching [122]. For the white-light generation, about 40 µJ from the commercial Ti:Sa multi-pass amplifier presented in the previous section are broadened in a krypton-filled HCF at about 3 bar and recompressed with chirped mirrors. The CEP of the infrared seed pulses is passively stable and preserved during the amplification process to a stability of 155 mrad as confirmed by f-2f interferometry [38]. The seed pulses are stretched in 9 mm of silicon and an acousto-optic programmable dispersive filter (AOPDF, DAZZLER). The AOPDF serves two important purposes: Firstly, it can correct for higher order spectral phase terms, which is important for the compression of the output pulse. In Section 3.3 an example for iterative pulse compression with the AOPDF is shown. Secondly, it can modulate the CEP of consecutive waveforms in the pulse train in order to facilitate heterodyne signal detection, as explained in Section 3.2 and Section 5.2.

Pump Generation In order to seed the OPCPA pump laser, the 1030 nm pulses derived directly from the oscillator are stretched by a pair of gratings, boosted in a fiber amplifier (Friedrich-Schiller-University Jena) to about 360 pJ, and used as seed for the thin-disk ytterbium-doped yttrium aluminum garnet (Yb:YAG) regenerative amplifier. The output pulses with energies of 17 mJ are compressed to 1.5 ps and pump the OPCPA. More details on the pump laser design and operation can be found in [123]. The amplification dynamics and its role in stable OPCPA operation is investigated in [124].

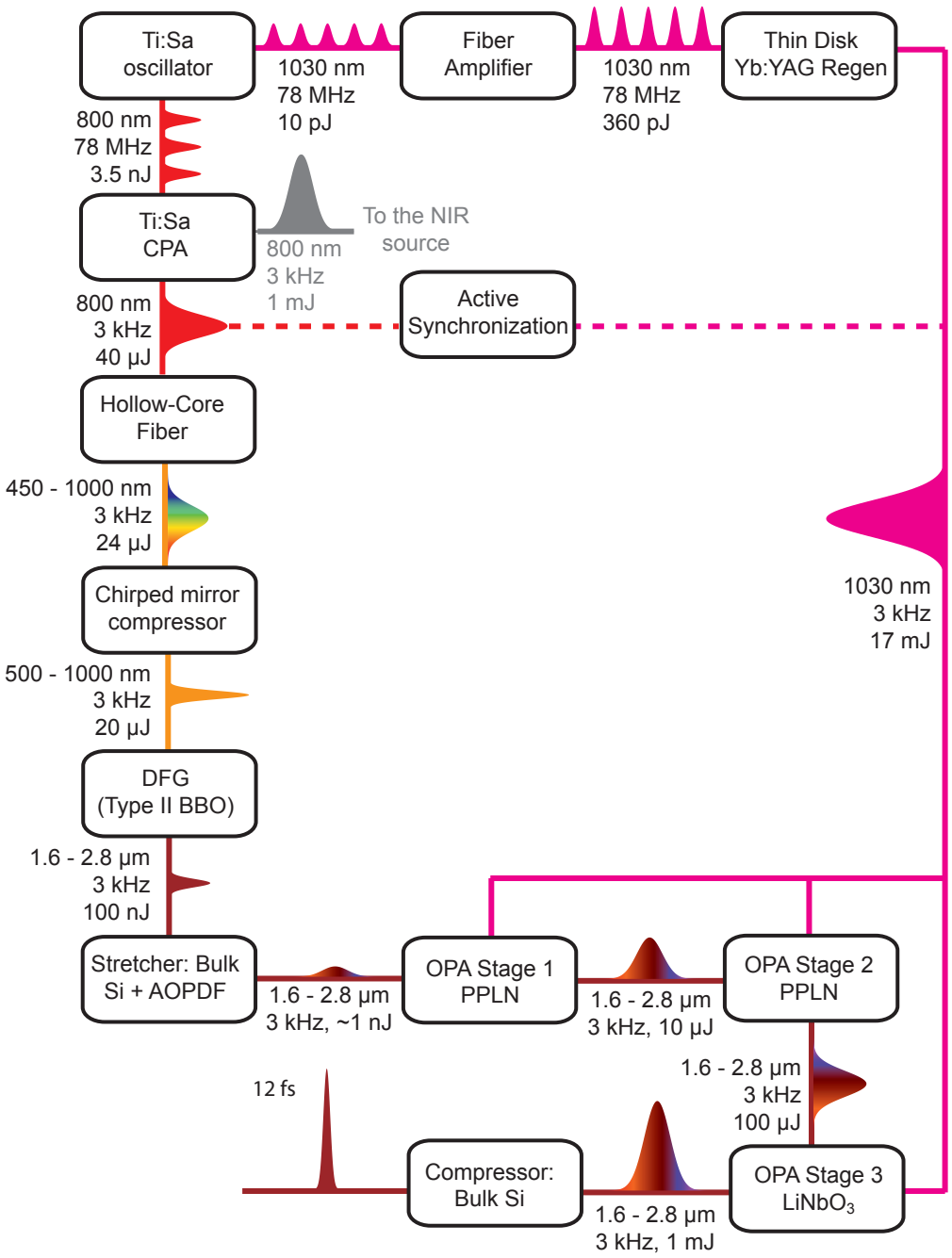

Figure 2.3: Short-Wavelength-Infrared Source. Pump and seed arm of the OPCPA are derived from the same Ti:Sa oscillator. The inherently phase-stable, broadband infrared seed is provided by intrapulse DFG of the white light which is generated by broadening 40 µJ pulses out of the Ti:Sa amplifier, similar to Fig. 2.2. The pump pulses are produced by a Yb:YAG thin disk regenerative amplifier and used to amplify the seed beam in three consecutive stages. For stretching and compression bulk silicon and an AOPDF are used.

OPA Stages Pump and seed pulses are combined in two amplification stages using magnesium-doped periodically-poled lithium niobate (PPLN) crystals (HC Photonics) with 2 mm thickness in the first and 1 mm in the second stage. The periodic poling of the material allows for a broad bandwidth of the amplified spectrum via quasi-phase-matching, see Subsection 1.2.1. The pump pulse energies are 0.4 and 3 mJ, respectively. The resulting 150 µJ pulses can be compressed down to sub-two optical cycles in bulk silicon by adjusting the higher order spectral phase with the AOPDF. An optional third amplification stage in bulk $LiNbO_3$ can provide amplified pulse energies of about 1 mJ. PPLN cannot be used in this final stage because, despite advances in manufacturing, the aperture size of PPLN is still limited to 3 mm. This is smaller than the beam sizes in the third stage which have to be used for efficient pumping without damaging the crystal. A picture of a typical seed and amplified OPCPA spectrum after the second stage is shown in Fig. 2.4.

A more detailed description of this OPCPA can be found in [38], for a more general consideration of the design parameters of OPCPA systems see [15, 125].

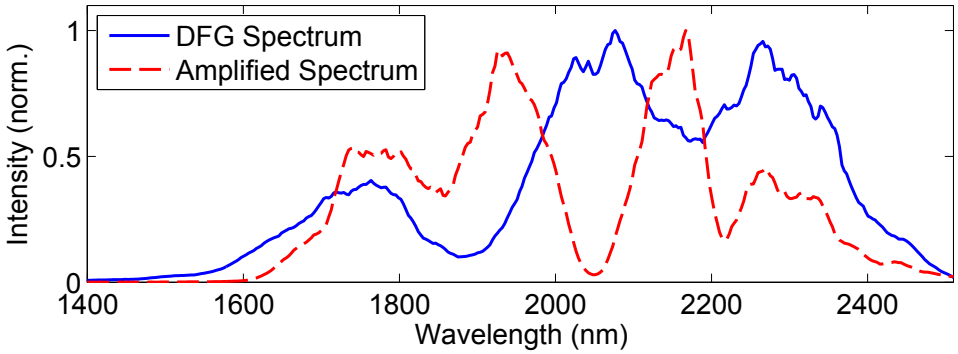

Figure 2.4: Seed and Amplified OPCPA Spectrum. The seed spectrum is recorded before the AOPDF, the amplified spectrum after the AOPDF and two OPCPA stages. The long-wavelength part of the spectrum above 2500 nm lies out of the sensitivity range of the InGaAs based spectrometer. The distinct drop at 2060 nm in the amplified spectrum is due to the phase-matching conditions in the degenerate OPA which also support the SHG of the OPA signal to the pump wavelength of 1030 nm.

2.3 Two-Color Interferometric Setup

The two-color interferometric setup features the combination of two sub-two-cycle pulses in different spectral regimes with a variable delay: a white-light arm with frequencies in the visible/NIR range and an infrared arm with frequencies in the SWIR range. The two arms can be used in a multitude of pump-probe schemes. In the course of this work, they have been applied as sample/test pulses in the EOS experiments in Chapter 3 and as injection/drive pulse as presented in Chapter 5. A schematic overview of the interferometer is given in Fig. 2.5.

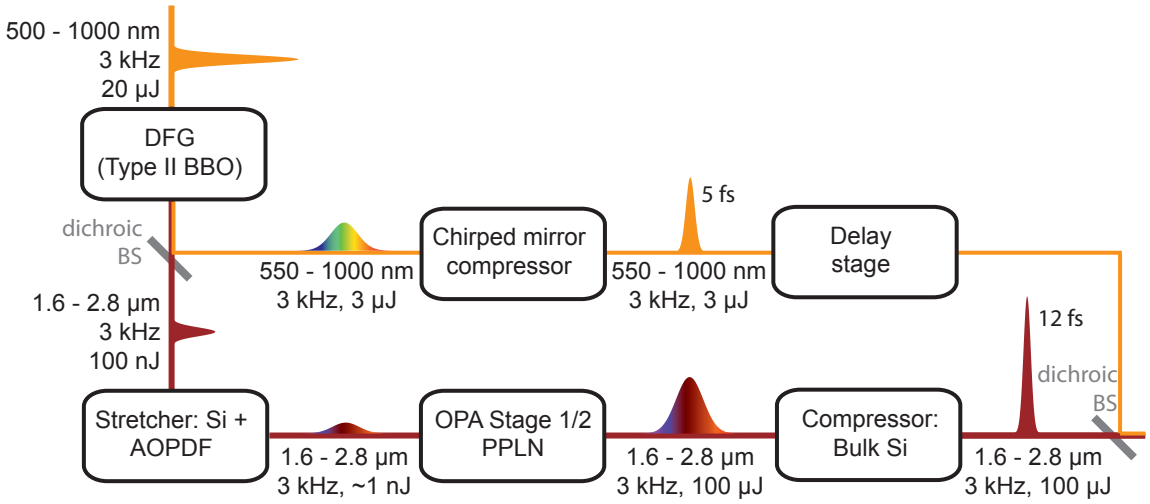

Figure 2.5: Two-Color Interferometric Setup. After the generation of the ultrabroadband OPCPA seed, the residual white light is split off and recompressed to about 5 fs. After compression of the second amplification stage, the two arms are recombined with crossed polarizations and an adjustable time delay.

As described in the previous section, the 4 fs white-light pulses generate the inherently phase-stable infrared seed for the OPCPA via intrapulse DFG. The residual white-light after DFG is split off with a dichroic beam splitter and recompressed to about 5 fs with chirped mirrors. After introducing an adjustable delay in the visible/NIR arm, both pulses are recombined collinearly with crossed polarizations. The two beam splitters used for separating and combining the two colors are custom designed for low dispersion and coated on a 1 mm fused silica substrate by the group of Dr. Vladimir Pervak. The maximum pulse energy is 3 µJ in the visible/NIR and 100 µJ in the SWIR arm. The beams can be attenuated independently by two apertures. For the SWIR pulse, the power can also be adjusted by a pair of wire-grid polarizers. While the infrared pulse is inherently phase-stable, the white-light requires a phase-stable operation of the Ti:Sa oscillator front end.

In order to test the stability of our experimental setup, the CEP in both arms as well as the timing jitter in the interferometer are recorded. The CEP stability for the white light and the infrared arm is characterized by collinear f-2f and 3f-4f interferometry, respectively. As shown in Fig. 2.7, the stability is good with a standard deviation of 235 mrad in the infrared and 151 mrad in the white-light arm. To measure the relative timing stability between the two arms, an interferogram between the third harmonic of the infrared spectrum and the white light can be recorded. The result is shown in Fig. 2.7. The standard deviation of the frequency of the fringes can be converted into a relative group-delay jitter of 1.5 fs.

The interferometer is employed in Chapter 3 and Chapter 5 for pulse characterization of the infrared waveform. However, the same setup can also be used for temporally characterizing the white-light pulse. Focusing both beams in a BBO crystal and placing

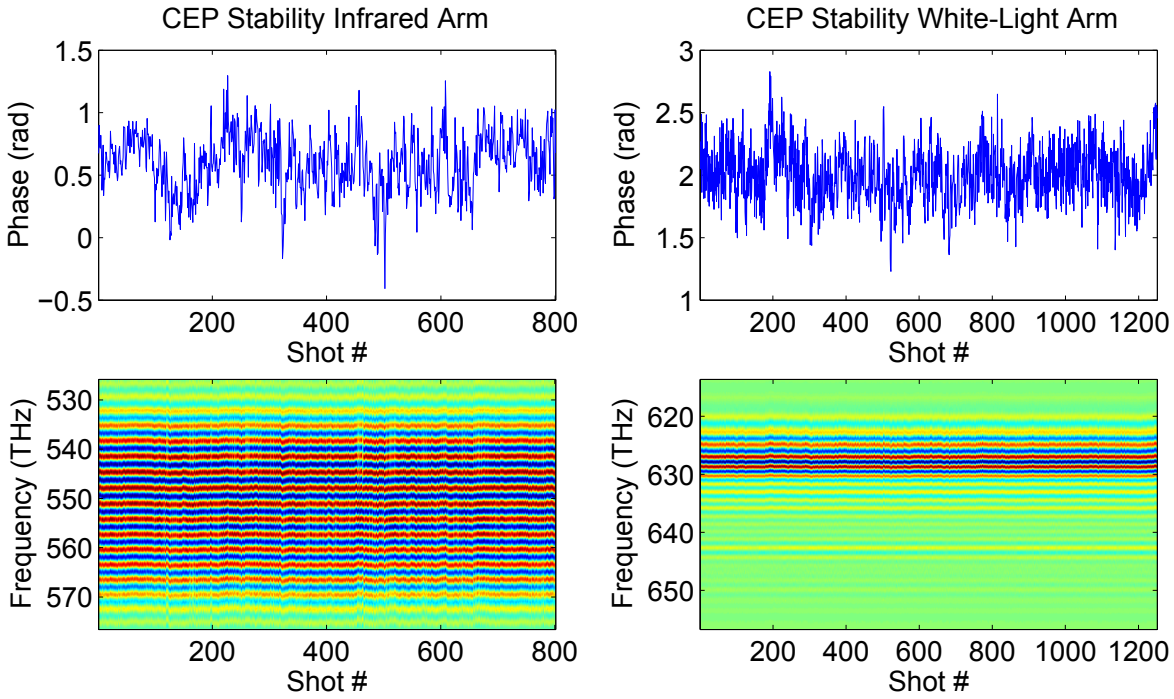

Figure 2.6: CEP Stability of Two-Color Interferometer. Left column: 3f-4f interferometry of the SWIR arm which shows a standard deviation of the CEP of 235 mrad. Right column: f-2f interferometry of the visible/NIR arm with a standard deviation of 151 mrad. The lower plots show the color-coded fringe-intensity in arbitrary units. The integration time of the spectrometer is 10 ms for the infrared and 2 ms for the white light, the total measurement duration in both cases is about 4.5 min.

an off-centered iris in either of the two beams of the interferometer, introduces a slightly non-collinear geometry, which allows the SFG signal to be spatially separated from the fundamental beams, frequency resolved, and used in an XFROG [126]. In Fig. 2.8, an XFROG measurement of the white-light pulse is shown which retrieves to a pulse duration of 5 fs. The SWIR pulse can be characterized by the metrology scheme introduced in Chapter 3 and used as the known reference.

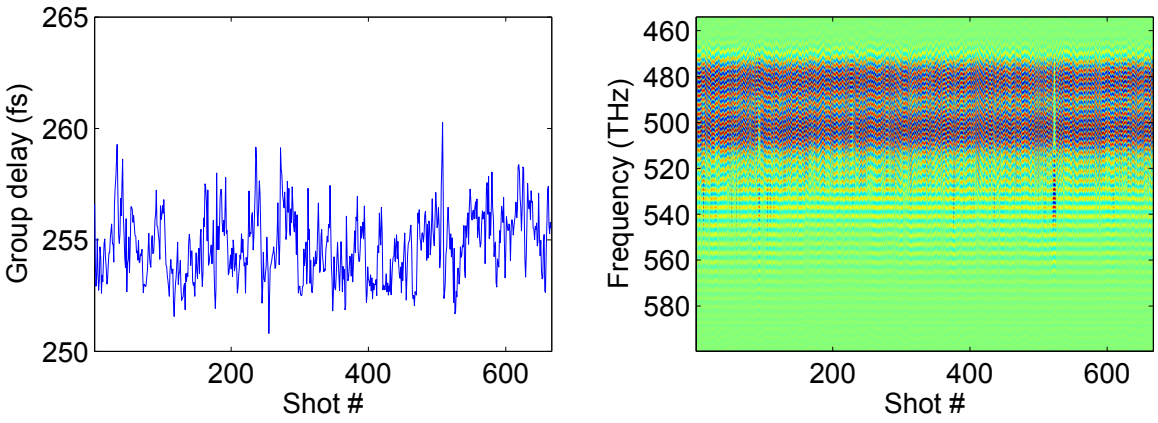

Figure 2.7: Timing Stability of Two-Color Interferometer. Interferometry of white light and third harmonic of the infrared. The right plot show the color-coded fringe-intensity in arbitrary units. The integration time of the spectrometer is 50 ms, the total measurement time about 15 min. The standard deviation of the relative group delay is 1.5 fs.

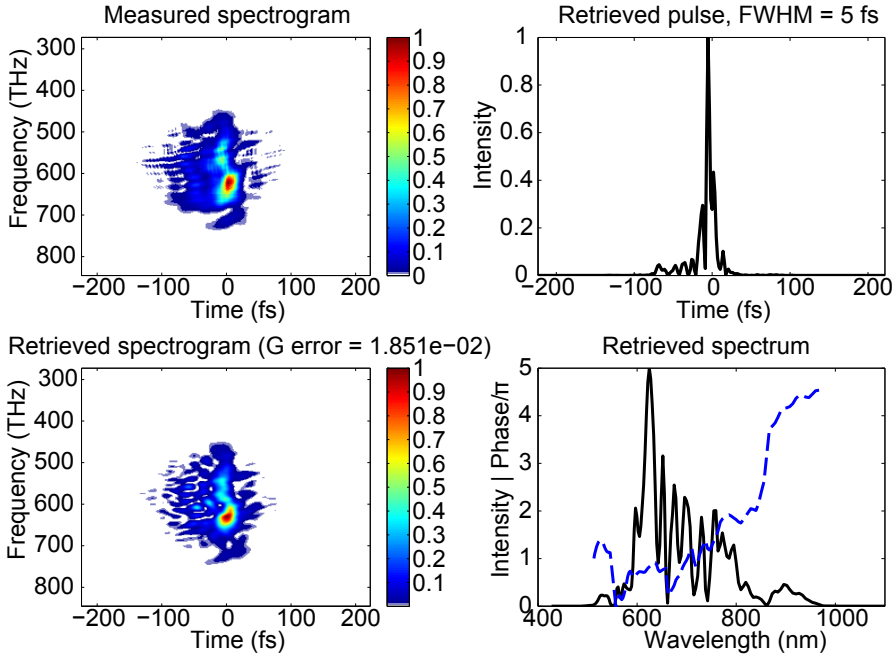

Figure 2.8: XFROG Trace of EOS Sampling Pulse. The trace is recorded with the two-color-interferometer and retrieved using the characterized two-cycle SWIR pulses as reference. The retrieval results in a pulse duration of 5 fs.

Chapter 3

Electro-Optic Sampling of Near- to Short-Wavelength-Infrared Waveforms

In order to study strong-field effects in solids and utilize them for metrology applications, it is necessary to gain full knowledge of the applied electric field. Electro-optic sampling (EOS) provides complete and unambiguous field information of a waveform by utilizing a short sampling pulse as gate, overlapping both pulses in an electro-optic crystal, and detecting the delay-dependent polarization rotation of the sampling pulse. In the terahertz domain, the concept of EOS has been employed successfully for decades [3] and has facilitated the observation of the dynamics of charge-carriers [50, 127, 128, 129, 130, 131], quasiparticles [132], and active optical devices [133]. Advantages of this technique are its compact setup, great dynamic range, and high sensitivity. One demonstration of its excellent achievable sensitivity is the recent measurement of vacuum fluctuations of the electric field by Riek et al. [134].

However, the cutoff frequency of the measured waveforms has until now been limited to the range of 135 THz or 2.22 µm [12, 135] and below. So far only techniques requiring a complex vacuum apparatus - like the attosecond streak camera and the petahertz oscilloscope presented in Section 1.4 - or combined techniques using EOS together with FROG measurements [90, 61] have been able to record the electric field of NIR waveforms.

The question which is addressed in this chapter is if EOS can be extended to the NIR and SWIR regime, where phase-stable sources based on OPCPA systems - like the one presented in Subsection 2.2.2 - show great promise to supersede Ti:Sa based amplifiers for strong-field experiments in gases as well as in solids [14, 136, 137, 15]. This would make EOS the first complete pulse characterization technique in this spectral range. Since it only requires a compact setup in ambient conditions, it enables a simple integration with existing experiments.

After introducing the general concept in Section 3.1 and the experimental setup in Section 3.2, EOS is presented as a valuable diagnostic tool allowing for complete characterization of a SWIR waveform with an almost octave spanning spectrum in Section 3.3.

Exemplary applications include the sub-two-cycle compression of the infrared pulse by feeding the characterized phase back to the AOPDF as well as observing the evolution of the amplified waveform at different pump powers due to changes in the OPA phase and thermo-optic effects. Section 3.4 focuses on the question how EOS can be even further extended to the NIR by post-spectral filtering, achieving an unprecedented cutoff frequency of 235 THz.

This chapter closely follows Keiber et al. [138] where the results were first published.

3.1 Concept

EOS is based on the interaction of a weak, short sampling pulse with a phase-stable infrared or terahertz field, in the following referred to as test field, in an electro-optic crystal. In case the frequency of the test waveform is small compared to the bandwidth of the sampling pulse, EOS can best be explained in the framework of the DC Pockels effect (see Eqn. 1.39): The test field introduces birefringence in the crystal which leads to a delay-dependent polarization rotation of the sampling pulse. This polarization rotation is linear with respect to the instantaneous test field amplitude and can be measured in an ellipsometer, which is further described in Section 3.2.

For a high frequency test waveform, which is the scope of application in this work, it is instructive to describe the sampling process in the frequency domain: When sampling and test pulse overlap in an electro-optic crystal that is phase matched for SFG, part of the sampling field gets shifted to higher frequencies. This nonlinear signal is perpendicularly polarized to and has spectral overlap with the high-frequency part of the initial sampling spectrum. The interference between the spectrally overlapping, crossed-polarized electric fields leads to a measurable, delay-dependent polarization rotation. In case the DFG is phase matched, the same picture applies with the only difference that the generated nonlinear signal overlaps with the lower frequencies components of the sampling spectrum which has to be selectively transmitted.

It is important to note that no retrieval is necessary to extract the field trace from the recorded polarization rotation. The measured signal is a convolution of the test waveform with the response function of the measurement, which results from the propagation of the waveform through the EOS crystal, the finite response time of the sampling pulse, and the spectral sensitivity of filters and detectors, see Eqn. 3.2. As is shown in Section 3.4, this deconvolution is required to correct the spectral intensities at high frequencies close to the cutoff.

3.2 Experimental Setup

The experimental setup is based on the two-color interferometer, presented in Section 2.3. The 5 fs white-light pulse is used for sampling the OPCPA few-cycle waveform. For the first experimental demonstration, we choose a type I phase-matching configuration. An

EOS setup utilizing type II phase matching is introduced in Chapter 5. We extract the parallel polarization components of both arms, which are 45° to the laboratory plane. The pulses are focused into a type I BBO crystal (Innowit) phase matched for SFG. Typical focus sizes are 180 µm for the infrared and 80 µm for the white-light spot ($1/e^2$ width). The SWIR focal spot is measured by the same silicon charge-coupled device (CCD, Dataray Wincam) as the white light, making use of two-photon absorption (see Eqn. 1.41) and correcting the detected beam size by a factor of $\sqrt{2}$. The thickness of the used crystals lies between 10 µm and 100 µm.

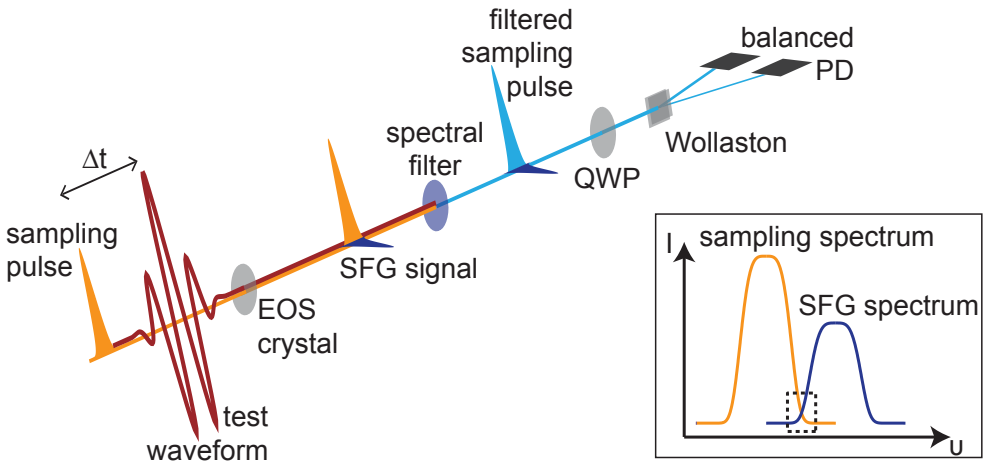

Figure 3.1: Experimental EOS Setup, based on the two-color interferometer from Section 2.3. After recombining the parallel polarization components of the test waveform and the sampling pulse collinearly, the pulses are focused into an EOS crystal (type I BBO). The orthogonally polarized SFG signal spectrally overlaps with the sampling pulse. This leads to an interference at the high-frequency end of the sampling spectrum which is selectively transmitted through a spectral filter. To detect the resulting polarization rotation with respect to the temporal delay Δt, the filtered pulse is sent through a quarter-wave plate, a Wollaston prism and onto a balanced photodiode. The inset shows the frequency domain with the overlap region of sampling and SFG spectrum emphasized in the dashed black box.

Scanning the temporal delay between the pulses, we can detect the polarization rotation which is induced in the white-light with an ellipsometer. It consists of a quarter-wave-plate, a Wollaston prism, and a balanced photodiode as depicted in Fig. 3.1. This setup is similar to the original free-space EOS measurements in the terahertz regime [3]. The role of the spectral filter is clarified in Section 3.4. Modulating the CEP of the infrared pulse with the AOPDF at 1.5 kHz, which is half of the repetition rate, allows for heterodyning and efficient detection at the modulation frequency with a lock-in amplifier (SR830, Stanford Research Systems).

In order to estimate how the interferometric jitter recorded in Fig. 2.7 affects the measurements, consecutive EOS traces are compared as shown in Fig. 3.2. The changes

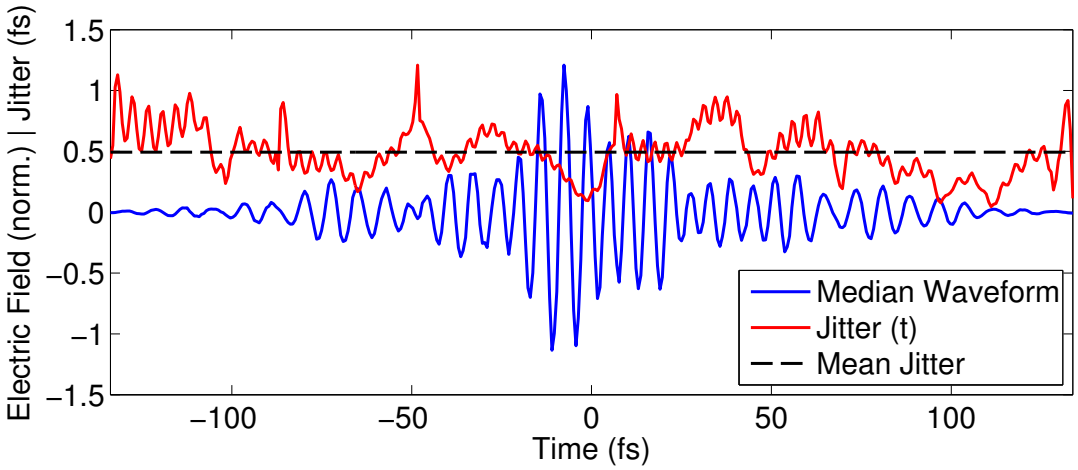

Figure 3.2: Stability of EOS Measurements. Median trace (blue) and timing jitter (red) of an EOS measurement with five consecutive scans with a total measuring time of about 4.5 min and a lock-in time constant of 100 ms. The jitter is extracted from the phase variations in time-gated segments of the traces and equals 0.49 fs on average (black dashed line). There is no obvious correlation between jitter and waveform intensity.

between waveforms result from a combination of timing instabilities and infrared CEP fluctuations. The jitter is calculated by averaging the absolute phase in time-gated segments of the waveforms and equals 0.49 fs. This corresponds to 14 % of the half-cycle duration at the central wavelength 2.1 µm of the infrared arm. The instabilities are lower than in the interferometric measurement recorded in Fig. 2.7, since fast jitter below the time constant of 100 ms is averaged out. Furthermore, intensity fluctuations, which can lead to jitter via amplitude-phase coupling in the third harmonic process, are eliminated. Fig. 3.2 shows that there is no correlation between the instantaneous field strength of the waveform and the jitter, so intensity-related phase shifts, which lead to a systematic distortion of the measured trace, can be excluded.

3.3 Broadband Electro-Optic Sampling in the Short-Wavelength-Infrared

Fig. 3.3 depicts two exemplary EOS traces of the unamplified seed and the first stage signal of the OPCPA in time and frequency domain. It should first of all be noted that the agreement of the EOS spectrum, calculated by taking the squared modulus of the Fourier transformed temporal electric field trace, with the spectrum measured with a commercial InGaAs based grating spectrometer (NIRQuest, Ocean Optics) is excellent. In the case of the seed in Fig. 3.3 b), the grating measured spectrum is taken before the AOPDF, which explains the differences to the EOS result, especially in the short wavelength regime where

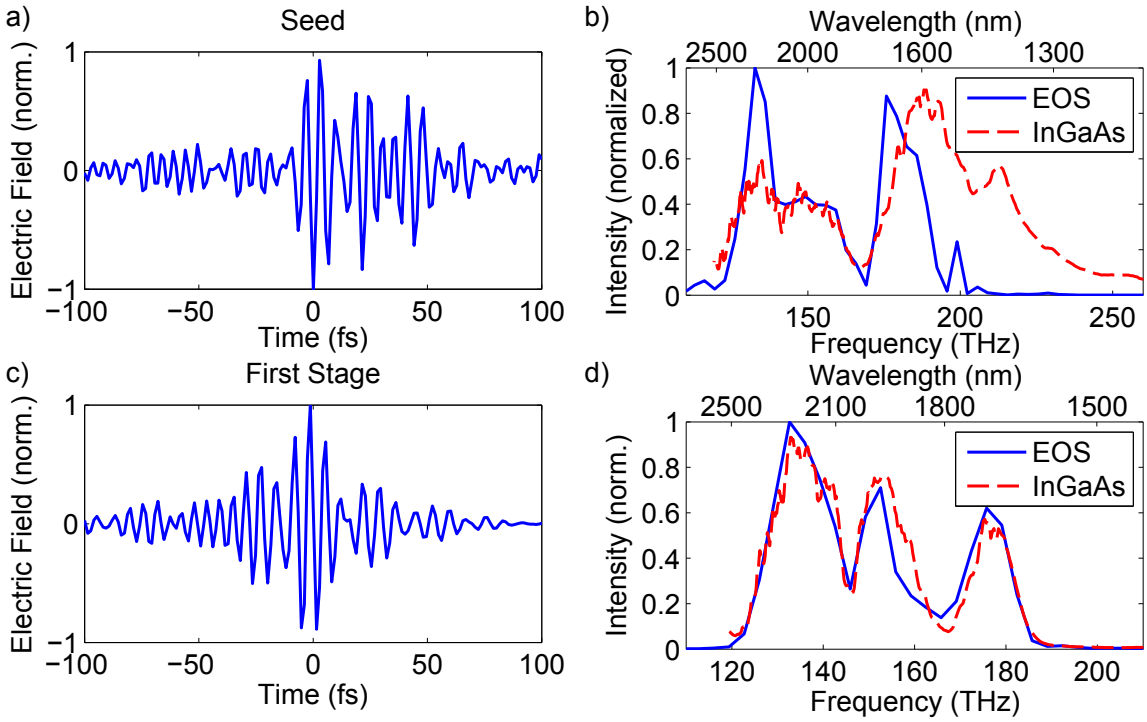

Figure 3.3: Broadband EOS of Short-Wavelength-Infrared Source. Left column: The measured EOS trace. Right column: The spectral intensity of the EOS waveform (blue solid line) compared to the spectrum measured with a commercial InGaAs spectrometer (red dashed line). Top row: The nanojoule seed of the OPCPA used as test pulse. Bottom row: The output of the first OPCPA stage used as test pulse. Adapted from [138].

the AOPDF transmission cuts off at about 1500 nm. The second noteworthy result is that EOS can resolve even the unamplified seed after the AOPDF with pulse energies of a few nanojoule, which shows the great sensitivity of this technique. The dynamic range in case of fully amplified two stages is 1×10^5. The measurement time for one trace lies on the order of 10 min.

The precise knowledge of the electric field of the OPCPA can be used in order to facilitate its day-to-day temporal compression to sub-two optical cycles. Once the OPCPA pulse is characterized, the phase information can be fed back to the AOPDF in order to compensate for the detected dispersion and generate a flat phase. An exemplary compression using two feedback iterations can be seen in Fig. 3.4. In daily operation of the OPCPA, we have found this technique more reliable than the phase characterization with a THG FROG device used previously [38]. Since no retrieval is needed in order to extract the electric field from the measured trace, the characterization of the waveform with EOS is also faster.

Another application which takes advantage of the excellent dynamic range of EOS, is the detection of the OPA phase and how it evolves with different pump powers. In

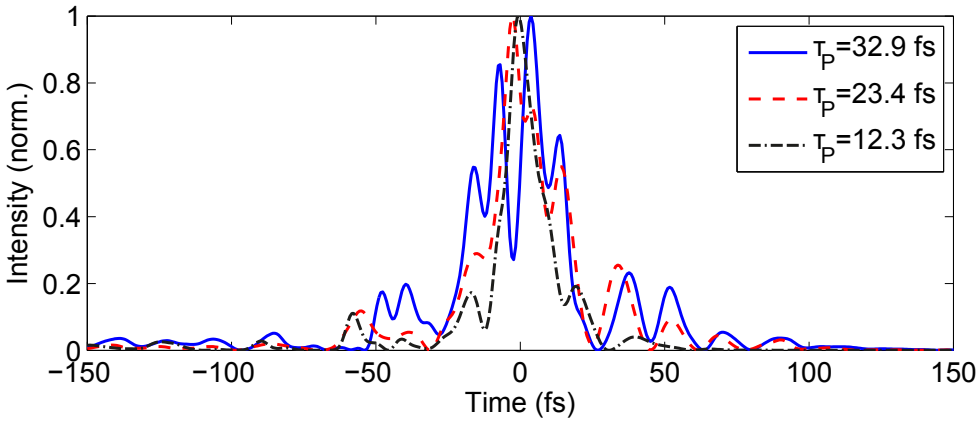

Figure 3.4: OPCPA Compression with EOS. Original waveform (blue solid line) compared to waveforms after one (red dashed line) and two (black dotted-dashed line) feedback iterations where the EOS characterized phase is fed back to the AOPDF to compensate for it.

order to measure this, the pump power in the second stage is attenuated while all other OPCPA parameters are kept constant. The temperature of the PPLN crystal is monitored with a thermal camera. At the highest output energy of 93.3 µJ corresponding to 7.3 W pump power in our case, the second stage saturates and the amplified spectrum shows characteristic saturation features like the prominence of the edges and dips in the center of the spectrum, as depicted in Fig. 3.5. These changes are due to back conversion of energy from the seed to the pump wavelengths. Comparing the EOS traces for increasing pump levels, multiple of changes in the waveforms, besides an increasing amplitude, can be detected: the pulse shifts to earlier times with higher pump powers and the CEP evolves in a non trivial way, as can be seen in Fig. 3.6.

In order to understand the underlying dynamics of this waveform evolution, simulations of the EOS process and the subsequent focusing based on the nonlinear wave equation in the slowly-evolving wave approximation, see Eqn. 1.29, are performed by Dr. Nicholas Karpowicz. The details of the simulation can be found in [138]. The agreement between the measured and simulated waveforms is excellent. The temporal shift in the waveforms can be understood in terms of the increase of crystal temperature by 20 K as confirmed by the thermal camera and the resulting change in the refractive index in $LiNbO_3$ [139]. Also the non-trivial CEP shift can be reproduced and hints on the strong coupling between phase and pump power in the OPA stages. The jumps in the simulated phase evolution are due to the reshaping of the pulse envelope which leads to different half cycles having the greatest amplitude. These results emphasize the importance of stable pump lasers for strong-field measurements. In addition, they suggest a solution for CEP management in case of multiple amplification stages since the phase shift with increasing pump power is not monotonous. By adjusting the experimental parameters in subsequent OPCPA stages, there is a potential configuration such that pump-related phase shifts cancel in the

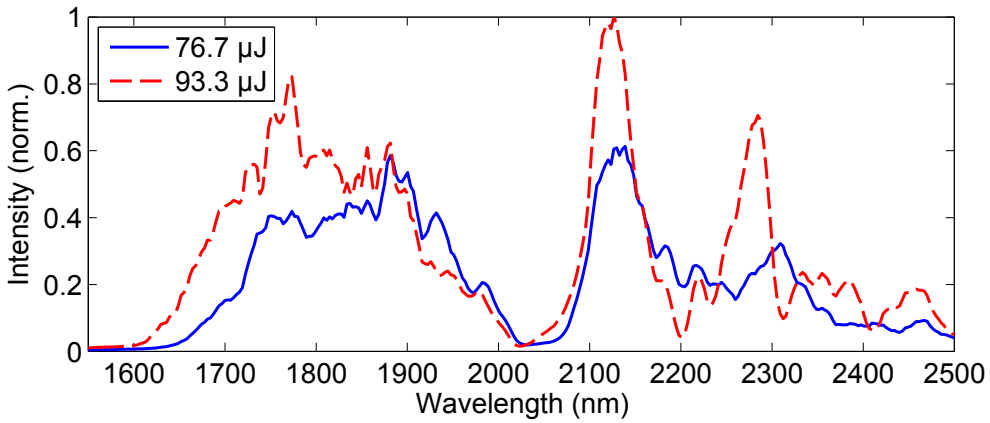

Figure 3.5: OPCPA Spectrum at Different Pump Energies. At 76.7 µJ output energy, the OPCPA spectrum is not yet saturated (blue solid line). At 93.3 µJ, the spectral wings are enhanced and the center is modulated with a dip at 2200 nm (red dashed line). Theses features are due to the onset of back conversion of energy from the seed to the pump.

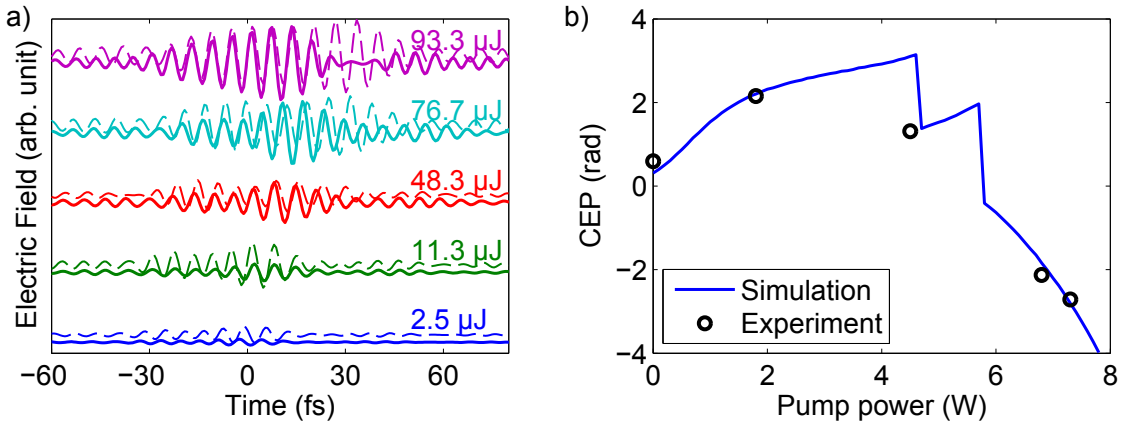

Figure 3.6: OPCPA Phase Evolution. a) Measured (solid line) and simulated (dashed line) OPCPA waveforms for different second stage pump powers. The output energies increase from the bottom to the top. b) Measured (black circles) and simulated (blue line) CEP evolution versus pump power. Adapted from [138].

amplified pulse.

3.4 Spectral Response of Electro-Optic Sampling

As the previous section has shown, EOS can sample the entire bandwidth of the SWIR OPCPA. In order to investigate how far the spectral cutoff can be pushed, we shift the test waveform to shorter wavelengths by adjusting the phase matching of the DFG process and bypassing the DAZZLER and the amplification stages due to their limited transmission bandwidth. The resulting spectrum ranges from 1100 nm to 1900 nm and is plotted in Fig. 3.7 c). The chirped pulse has an energy of few tens of nanojoule and is stretched in a silicon wafer in order to separate the different wavelength components in time, see Fig. 3.7 a). The excellent sensitivity of EOS still allows the unamplified and stretched pulse to be sampled with great signal-to-noise ratio. The recorded trace is deconvoluted by the response function, see Eqn. 3.2.

Zooming in to the trailing edge of the pulse, which features the high-frequency components in Fig. 3.7 b), reveals that even oscillations with a period of 4.25 fs can be resolved. This corresponds to 1.27 µm, or 235 THz in the frequency domain. The spectrum calculated from EOS is slightly shifted with respect to the one measured with a grating spectrometer. We attribute this to the fact that EOS samples the test spectrum at the center of the focus, where it overlaps with the sampling pulse, while the spectrometer measures the spectrum of the whole beam. In the case of the amplified waveforms, this difference is not so pronounced because of the mode cleaning in the pumped OPA crystals. The deconvolution of the detector function has hardly any effect on the longer wavelengths components but noticeably rescales the spectral amplitudes near the cutoff region. Even on a linear scale, frequency components around 240 THz can still easily be distinguished.

The high frequency of the spectral cutoff might be surprising upon first sight. According to the Nyquist-Shannon theorem [140]

$$f_s \geq 2f_t \ , \tag{3.1}$$

where $f_s = 1/\tau_P$ is the sampling frequency and f_t is highest detectable frequency of the test waveform, our sampling pulse with τ_P=5 fs should result in a cutoff of about 100 THz. The reason why in our case EOS is still sensitive to frequency components more than twice as high, lies in the short-pass spectral filtering. As previously shown by Porer et al. [141], spectral filtering improves the signal-to-noise ratio because it selectively cuts out the frequency components in the overlap region of the SFG and the sampling spectrum which contribute to the EOS signal. Thus, the additional noise caused by the spectral components outside of the relevant interference window is eliminated. The second important benefit of the short-pass filter is the reshaping of the response function of our detector $R(\omega)$. The measured signal $S(\Omega)$ at detection frequency Ω is given by the interference between the sampling field $E(\omega_{LO})$ acting as the local oscillator with the SFG field components generated by $E(\omega_{LO} - \Omega)$, convoluted with the detector response $R(\omega_{LO})$:

$$S(\Omega) = \int d\omega_{LO} R(\omega_{LO}) \, |E(\omega_{LO})| \, |E(\omega_{LO} - \Omega)| \, e^{i[\Phi(\omega_{LO}) - \Phi(\omega_{LO} - \Omega)]} \tag{3.2}$$

$R(\omega)$ is depicted in Fig. 3.8 a) together with the sampling spectrum. Despite the diminished blue spectral edge of the white light after the DFG process, there is still a non-zero intensity above the filter edge of 600 nm which contributes to the EOS signal. Fig. 3.8 b) clearly shows how the sensitivity is shifted to higher frequencies by employing the spectral filtering. Including the propagation through a 10 µm or 100 µm BBO crystal does not compromise the broad high frequency response of the detection.

The response is a complex function with amplitude and phase. Experimentally, most contributions to the response function are well known: The spectral response of the photodiodes as well as of used filters can be characterized and the shape of the white-light pulse can be measured by the XFROG technique in-situ, see Fig. 2.8. However, we cannot experimentally access an additional phase to the response function which the EOS process might introduce. Therefore, Dr. Nicholas Karpowicz performed simulations based on Eqn. 1.29 clearly showing the flat phase response in the spectral region of interest, see Fig. 3.9.

3.5 Outlook

This chapter has shown the EOS can be extended to the NIR regime. The key ingredients for this extensions are a 5 fs sampling pulse in combination with the broadband phase matching in BBO and the post-spectral filtering. The latter point allows the reshaping of the response function such that the roll-off predicted by the Nyquist-Shannon at 100 THz is superseded by more than a factor of two. This increase of the spectral cutoff shows great promise for establishing EOS as a pulse characterization technique for broadband NIR to MIR OPCPA systems. Not only can it be used for the daily characterization and compression of the pulses, it is also a sensitive tool to study dynamic processes in the amplifier itself.

Another important field of application is the strong-field light-matter interaction, where the precise knowledge of the electric field - including the CEP - is crucial for the interpretation of the system response. Experiments which have previously used Ti:Sa derived few-cycle pulse and characterized the system response with streaking can now be extended to the few micrometer wavelength regime. One example where such an extension could be beneficial is the recently demonstrated attosecond polarization spectroscopy [35], which resolves the nonlinear polarization dynamics and light-field-induced energy transfer in a dielectric sample by comparing the electric field transmitted through a thin fused silica plate at high and low intensity. While this study used few-cycle pulses derived from a Ti:Sa source and streaking for the field characterization, an experiment with a SWIR source has two major advantages: Firstly, the lower photon energy allows semiconductors to be studied in the highly nonlinear regime. Secondly, the longer central wavelength λ_0 makes it possible to use samples with a thickness $d < \lambda_0$. This simplifies the interpretation of the data by eliminating changes in the waveform due to the propagation in the material, which had to be taken into account in the original study.

Since the applicable wavelength range of EOS now includes the emission band of erbium-

doped fiber lasers around 1.55 µm, numerous applications including telecommunications [142] and eye-safe remote sensing [143] can also benefit from the presented metrology results.

The spectral cutoff presented in the previous section is no ultimate limit but merely a benchmark provided by our current experimental capabilities. It seems possible to push the spectral cutoff of EOS to even higher frequencies and make this tool available for laser systems working in the shorter wavelength regime, like the Ti:Sa based front end introduced in Subsection 2.2.1. Using BBO with its wide transparency range down to about 200 nm together with a shorter sampling pulse comprising frequency components in the blue visible to ultraviolet part of the spectrum, can result in a spectral cutoff below 1 µm. The feasibility of this approach is currently being investigated in our group.

In Chapter 5, we make use of the presented results in order to investigate optical-field driven currents in the two-pulse scheme, see Section 1.4. The direct comparison between the electric field of the drive pulse, characterized by EOS, and the measured current can provide knowledge about the response function of this strong-field process. We show that in the low drive-field regime the ultrashort, nonperturbatively generated gate formed by an optical-field-induced current can be used in a novel characterization scheme to sample waveforms.

This comparison is possible since EOS can be easily integrated with existing experiments since it neither needs a dedicated vacuum setup nor a strong HHG driver like the techniques presented in Subsection 2.1.3.

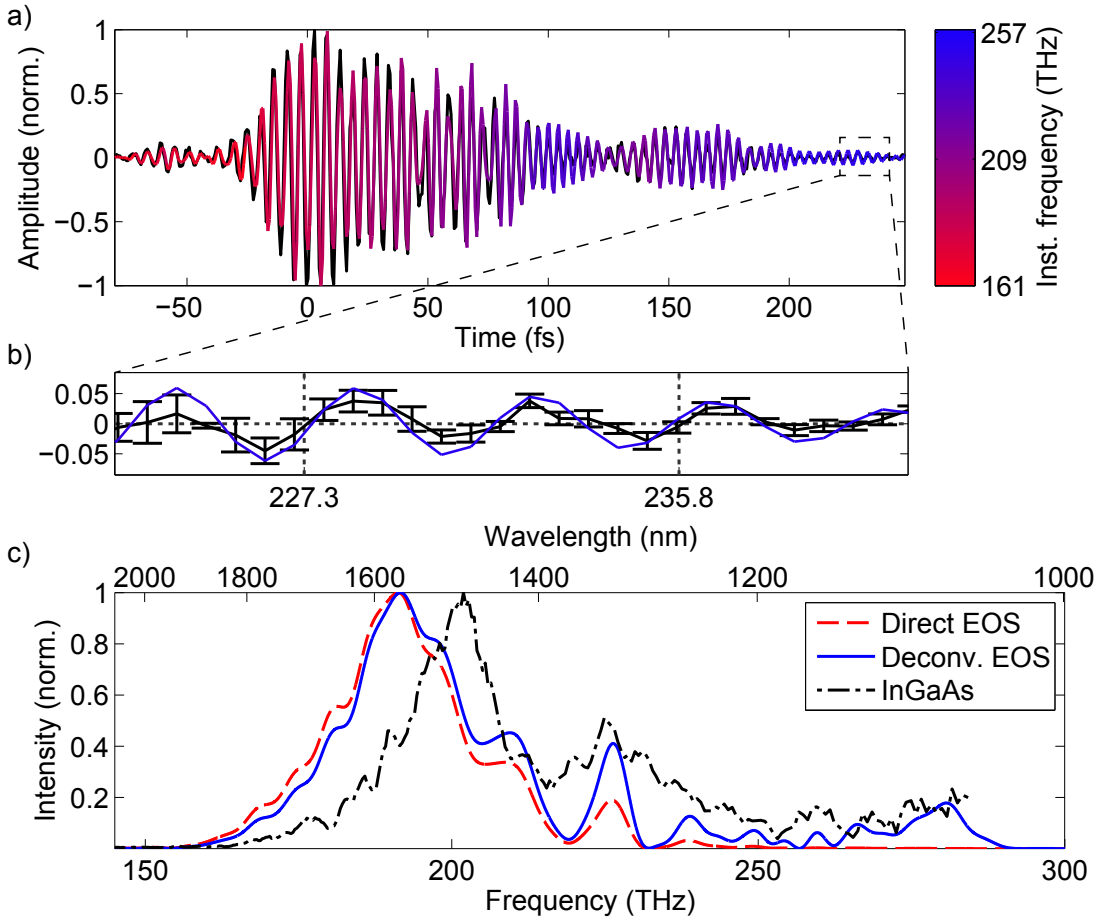

Figure 3.7: Spectral Cutoff of EOS. a) EOS trace of the chirped, blue-shifted OPCPA seed. The black line corresponds to the raw data before deconvolution. The deconvoluted data is color-coded to indicate the instantaneous frequency. The dashed box marks the position of the inset depicted below. b) Trailing edge of the pulse with a period of 4.25 fs corresponding to 235 THz. The gray dashed lines mark the zero crossings of two oscillation periods as a guide to the eye. The error bars indicate the standard error of the mean. c) The spectral response of EOS, direct (red dashed line) and deconvoluted with detector response function (blue solid line), compared with spectrum measured by InGaAs spectrometer (black dotted-dashed line). Adapted from [138].

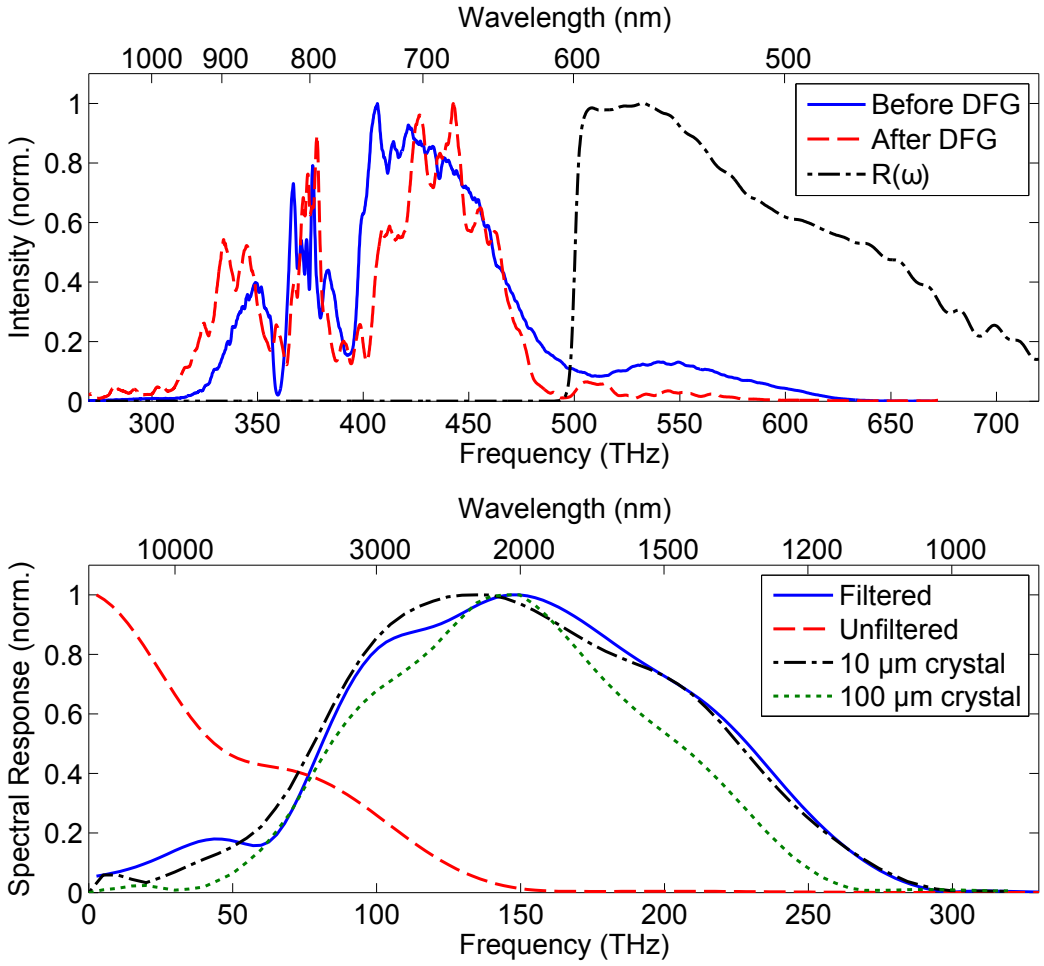

Figure 3.8: Response of EOS in Near-Infrared. a) Spectrum of the white light before (blue solid line) and after DFG generation (red dashed line line) compared to spectral detector response $R(\omega)$ (black dotted-dashed line). b) EOS spectral response corresponding to the actual detection using a short-pass filter (filtered, blue solid line) compared to uniform detection (unfiltered, red dashed line). Nonlinear propagation and dispersion the electro-optic crystal lead to similar responses using a 10 µm (black dotted-dashed line) and 100 µm BBO crystal (green dotted line). Adapted from [138].

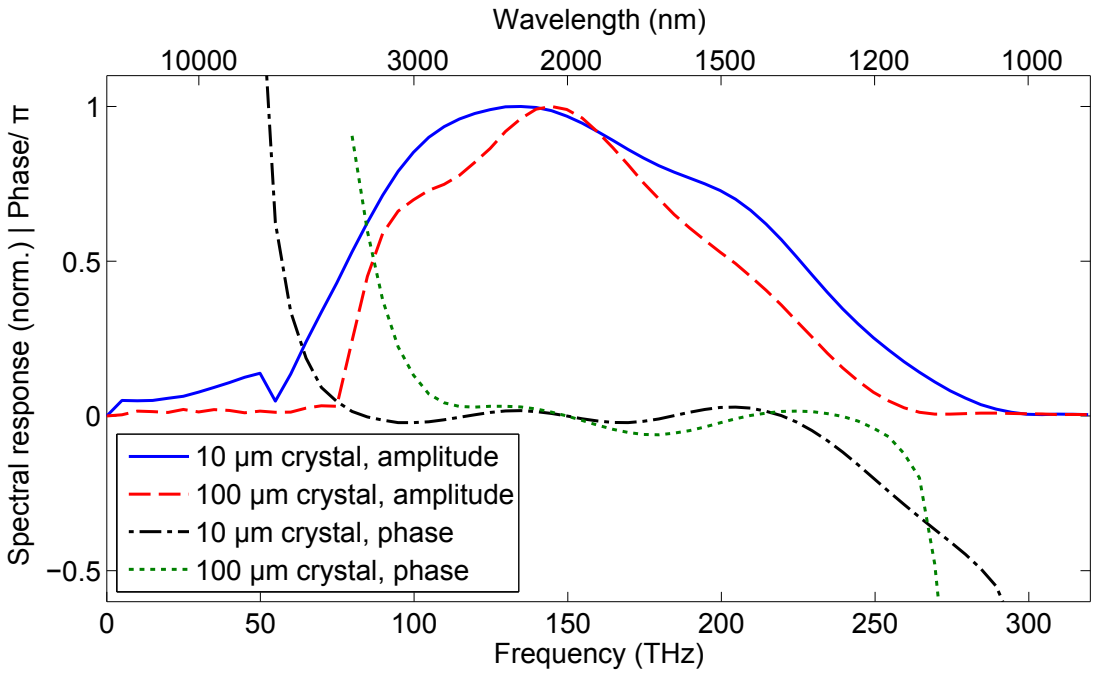

Figure 3.9: Complex EOS Response Function. The amplitude and phase of the EOS response function are shown for crystal thicknesses of 10 µm and 100 µm. In both cases, the phase shows a flat behavior for the experimentally relevant spectral range from 1200 nm to 3000 nm. Adapted from [138].

Chapter 4

Single-Pulse Near-Infrared Optical-Field-Induced Currents

Optically induced currents in solids have had a long and successful history in the generation, detection, and manipulation of electric signals: It started in the linear regime with the discovery of photoconductive switches by Auston [144] and their prominent application in the generation and detection of microwave to terahertz transients [145, 146, 147] with a time resolution in the picosecond range. Later, phase-sensitive currents in semiconductors were generated by using the interference of linear and nonlinear two-photon absorption pathways [148, 149, 67, 68, 69, 150, 70]. This allowed for coherent control in solid-state systems. Finally, the optical control over charge carriers reached the strong-field regime with optical-field-induced currents [4, 63].

In these strong-field experiments, the light-matter interaction takes place in the nonlinear to nonperturbative regime, which was discussed in Subsection 1.2.2. This results in an extremely short time scale on the order of 1 fs, during which the charge carriers are promoted from the valence to the conduction band. The short switching time as well as the degree of control over the amplitude of the current, which can be exerted by shaping the electric field of the laser pulse, make these currents promising candidates for applications in optical metrology [62] and electronic switching [2]. The switching rate at optical frequencies in the petahertz range by far extends the cutoff frequencies of classical electronic devices. State-of-the-art metal-oxide-semiconductor field-effect transistors (MOSFET) based on silicon reach switching speeds of several hundreds of gigahertz [151]. The highest cutoff frequencies have been achieved by high-electron-mobility transistors (HEMT), where the electron mobility can be increased using heterostructures with different semiconductor layers. Using this scheme, switching frequencies of 1 THz are within reach [152]. However, this is still three orders of magnitude smaller than optical frequencies. First design proposals for basic electronic elements based on optical-field-induced currents have already been published [153].

In previous experiments, it has been demonstrated that ultrafast currents can be generated in a variety of materials and sample geometries [63]. However, a detailed study on how the sample parameters influence the measured signal has to date been missing. Reaching a

better understanding of the physical mechanisms behind current generation and detection that are sensitive to these parameters has two major benefits: Firstly, using the current as an observable, the interband tunneling and intraband acceleration, which underlie some recent exciting strong-field experiments [8, 9, 61, 10], can be studied. Secondly, an understanding of how certain parameters influence the ultrafast generation of currents is an important prerequisite for their use in optical metrology and electronic switching applications. One example from the field of metrology is the strong-field pulse characterization technique, presented in Chapter 5. There, the promotion of carriers into the conduction band can be used as an ultrashort gate for time-resolving the electric field oscillations of an optical waveform.

Open questions regarding the optical-field-induced currents include but are not limited to:

- Which sample geometry is the most promising for the investigation of the ultrafast currents and which one is the most suitable for applications?
- Is the current generated primarily in the bulk material or on the surface of the sample?
- What role does the electrode-focus distance play in current generation and measurement?
- How does the amplitude of the current scale with the band gap of the sample material?

This chapter provides a first step towards answering these questions and suggests a roadmap for future investigations. After introducing the general concept in the first section, Section 4.2 presents the experimental setup. Section 4.3 investigates different sample geometries and how they influence the amplitude and phase of the measured currents. The material dependence of the signal is studied in Section 4.4 before an outlook for further investigations is provided in the last section.

4.1 Concept

The underlying mechanisms of ultrafast current generation have been introduced in Section 1.4. For the scope of this chapter, the semiclassical two-step picture including the injection and the drive process is most instructive: During the far-off-resonant injection process, electrons are promoted from the valence into the conduction band via tunneling and/or multi-photon absorption. Since the Keldysh parameter for our experimental parameters is close to 1, we are working in the intermediate regime (see Chapter 1). Once the electrons occupy the delocalized conduction band states, they can in a second step be accelerated towards the sample electrodes which results in a charge separation.

After this charge separation is generated, it has to be coupled into the external measurement circuit in order to result in a measurable current. The details of this coupling

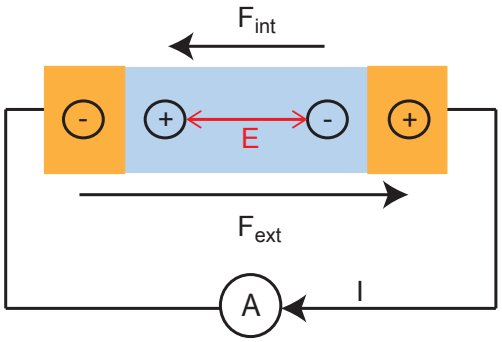

Figure 4.1: Current Detection in External Circuit. The electric field of the laser pulse E forms an internal field F_{int} by strong-field ionization and subsequent acceleration of the charge carriers. The internal field is shielded by the external field F_{ext} formed by the highly mobile electrons in the metal electrodes. This field causes a measurable current in the external circuit.

are not yet fully understood. Previously, it was believed that the electrons would reach the metal electrodes via ballistic transport and tunnel through the metal-insulator barrier [4]. However some experiments in [63] and all experiments in this work use up to 250 µm-sized electrode gaps. These gaps are not only bigger than the typical focal spot of about 50 µm ($1/e^2$ width) but also orders of magnitude larger than the mean free path of electrons which in the case of SiO_2 is only a few nanometers [154, 155].

An alternative explanation for the detection of the current is that the charge separation results in a dipole field which exerts a force on the free charge carriers in the metal electrodes and thereby induces a shielding field resulting in a current flow in the measurement circuit (see Fig. 4.1). Time-resolved terahertz spectroscopy has shown that photoexcited carriers in some large band gap dielectrics like SiO_2 get trapped which stabilizes the charge-separation [156, 157]. This explains the suppression of single-shot current signal for constant CEP at 3 kHz which was observed in [63]. The nature of carrier transport which leads to this charge separation is further discussed in Section 5.4.

4.2 Experimental Setup

The experiments in this chapter use the phase-stable NIR source presented in Subsection 2.2.1 and different sample geometries consisting of a dielectric substrate and a gold metal electrode structure, as depicted in Fig. 4.2. The properties of the different dielectric materials used can be found in Table 4.1. All experiments are performed in the one-pulse-scheme, employing a single pulse for the injection and acceleration of the charge carriers. Two basic experimental configurations are described in the following: one setup using the front end system 1 and an upgraded setup using the front end system 2 (see

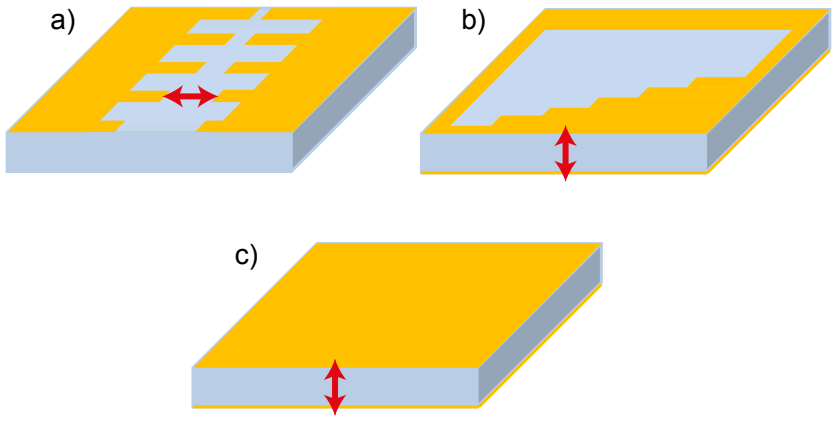

Figure 4.2: Near-Infrared Current Samples. a) Flat geometry with 100 nm gold comb-like electrode structure. b) Sandwich-like geometry with 100 nm gold step-like electrode. c) Sandwich-like geometry with a homogeneous 40 nm gold electrode. The red arrows mark the position of the focus and the polarization direction used in the experiments. A few nanometer thick adhesion layer of chromium is used between the dielectric and the gold electrode.

Subsection 2.2.1).

Experimental Current Setup 1 The experimental setup based on the front end system 1 is equivalent to the one used in [62, 63, 4], so it is only briefly described here. Two-cycle pulses with a central wavelength of 760 nm illuminate the dielectric samples in the gap formed by gold electrodes (see Fig. 4.3) with a focus size of about 50 µm. The laser polarization is chosen along the electrode gap and the power on target can be modified by a variable aperture. For each aperture setting, the focus size is measured with a silicon CCD camera (Dataray Wincam) for deriving the intensity and field strength. The pulse duration is determined by a TG FROG (see Subsection 2.1.1) to below 5 fs full-width at half-maximum.

In order to separate the CEP-dependent signal from any background current, the CEP is varied at half the repetition rate (1.5 kHz). The current averaged over one pulse is enhanced by a transimpedance amplifier (FEMTO Messtechnik GmbH) and measured with a lock-in amplifier at the modulation frequency of the CEP. The unmodulated background results from residual light hitting the electrode and accelerating the free electrons in the metal, thus generating a current. This signal is intensity- but not field-dependent. No bias is applied to the electrodes. The rise time of the measurement circuit is dominated by the 50 µs rise time of the transimpedance amplifier at a gain of 1×10^8 [169].

The measured current shows an oscillation with respect to the wedge insertion that is periodic with a CEP change of 2π. Varying the amount of dispersive material in the beam not only changes the CEP but also the GDD and higher order dispersion. Thus, the

Material	Orientation	E_g (eV)	n @ 760 nm	a (Å)	E_B (V/Å)
Fused Silica	NA	9.3 [158]	1.45 [159]	NA	NA
Borosilicate	NA	4.1 [160]	1.51 [160]	NA	NA
BaF_2	[111]	9.2 [161]	1.43 [162]	6.2 [163]	1.69
CaF_2	[111]	12.1 [164]	1.47 [162]	5.46 [165]	2.03
MgO	[111]	7.8 [166]	1.73 [167]	4.2 [168]	3.65

Table 4.1: Material Properties of Current Samples. Orientation indicates the crystal direction parallel to laser polarization, E_g the electronic band gap, n the real part of the index of refraction at the central wavelength of the NIR source, a the lattice constant, and E_B the critical electric for Bloch oscillations assuming linear screening, see Eqn. 1.55. For the amorphous materials fused silica and borosilicate, the parameters crystal orientation, lattice constant, and critical Bloch field are not available (NA) because the long-range crystalline order is absent.

amplitude of the oscillation decreases away from the optimum wedge position which gives a flat phase, see Fig. 1.9. In order to extract the maximum current, the insertion of one pair of fused silica wedges is scanned around the optimal compression point. Each data point in the current versus CEP traces is averaged over 3000 laser shots. The maximum current S_{max} and the current phase Φ are deduced by fitting a sinusoidal oscillation multiplied by a Gaussian envelope to the experimental data:

$$S_{max} \cdot \exp\left(-\frac{1}{2}\frac{(x-x_0)^2}{\sigma^2}\right) \cdot \sin(kx+\Phi) \ , \tag{4.1}$$

where x is the wedge position, x_0 the central wedge position for maximum signal, k the frequency of the oscillation, and σ the width of the Gaussian envelope. The uncertainties of S_{max} and Φ are given by the 95 % confidence interval of the fit.

Experimental Current Setup 2 In contrast, the upgraded front end system 2 allows for two important improvements of the experimental setup: Firstly, due to the different dispersion properties of the front end, it is possible to compensate for a larger positive GDD after the HCF. Therefore, two wire-grid polarizers (Moxtek) with 1 mm fused silica substrates can be introduced in order to attenuate the beam without affecting the focus size and position. This allows for the power and the focus size to be adjusted independently. Secondly, the AOPDF facilitates cycling of an arbitrary sequence of up to 22 waveforms. We choose to keep spectral phase and amplitude of the waveforms constant and introduce a periodic CEP offset of 0, $1/2\pi$, π, and $3/2\pi$ at one fourth of the repetition rate (750 Hz). This satisfies the Nyquist criterion $f_{rep} > 2 \cdot f_{cycling}$ which means that amplitude and phase of the current can be identified unambiguously for a single wedge position. This improvement facilitates the simultaneous detection of the maximum amplitude and phase of the injected current without scanning the CEP by changing the insertion of a pair of fused silica wedges. In addition, the current amplitude S_{max} is directly given by the lock-in

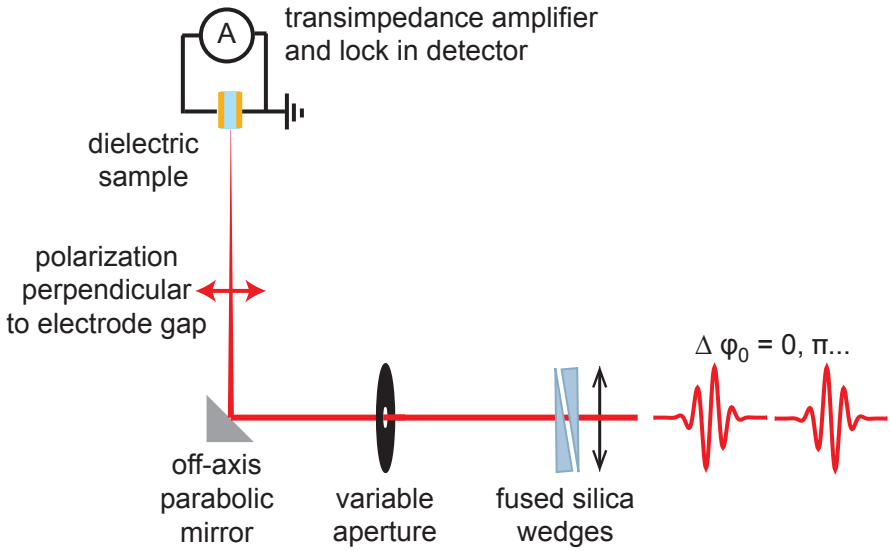

Figure 4.3: One-Pulse Near-Infrared Current Setup. Sub-two-cycle pulses with a CEP modulation at half the repetition rate are focused onto a sample, consisting of a dielectric substrate and a gold electrode structure. The polarization is perpendicular to the electrode gap. The intensity on target can be varied by an aperture, the CEP by the insertion of a pair of fused silica wedges.

amplifier and does not have to be calculated or extracted from a fit. As in the previous setup, one data point corresponds to an average over 3000 laser shots.

Utilizing these two improved features, the measurement setup and procedure could be changed as depicted in Fig. 4.4: While varying the field strength on the sample by rotating the first wire-grid polarizer, below 1 % of the power can optionally be picked off by a pellicle and measured by a diode power meter. The external measurement circuit remains unchanged compared to the previous paragraph. This setup enables faster detection and is thus especially beneficial for the intensity scans presented in Section 4.4 since it minimizes the influence of slow drifts and allows for better reproducibility of scans at different intensities.

4.3 Influence of Sample Geometry

Differently from [62, 63, 4] only samples with an electrode gap larger than the focus size are used in the experiments presented in this chapter. This has proven beneficial for the signal-to-background ratio, since fewer free electrons are illuminated, as well as for the damage threshold of the samples because metal ablation typically occurs at almost one order of magnitude lower fluences than the dielectric breakdown [7, 170]. Another advantage of the larger electrode gaps is an easier and more reproducible manufacturing process.

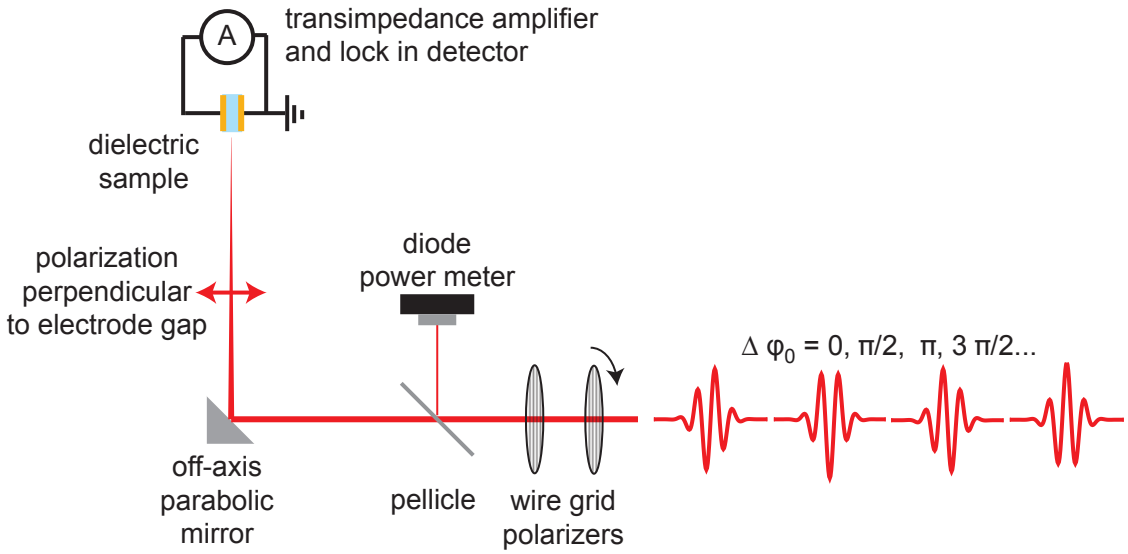

Figure 4.4: Upgraded One-Pulse Near-Infrared Current Setup. Sub-two-cycle pulses with a CEP modulation at one fourth of the repetition rate are focused onto a sample, consisting of a dielectric substrate and a gold electrode structure. The polarization is perpendicular to the electrode gap. The intensity on target can be varied by rotation of the first of two wire-grid polarizers and monitored by sending about 1 % of the power to a diode power meter.

4.3.1 Flat versus Sandwich-Like Geometry

Two main types of sample geometries are used in this chapter: flat and sandwich-like configurations. Both geometries can be used with a variety of different sample and electrode materials as well as electrode distances.

The sandwich-like structures consist of a dielectric substrate, optically polished and coated on both sides with a 40 nm layer of gold (on a 1 nm chromium adhesion layer). The coated substrates are cleaved in order to remove eventual short cuts of the electrodes at the substrate edges and to provide a well-defined surface for illumination, see Fig. 4.2 c). The bottom and the top surface form the two electrodes which can be contacted by clamping the cleaved substrate between two conductive metal fingers that are connected to the electric measurement devices. A variation of this geometry is the propagation sample presented in Subsection 4.3.2, see Fig. 4.2 b).

The flat geometries use dielectric substrates with one optically polished surface, where an electrode structure is defined by means of optical lithography. The electrode pattern can be wire bonded to a socket adapter which is contacted to the measurement circuit. For the experiments in Subsection 4.3.3 a comb-like electrode structure is used, where the distance between the electrodes can be altered by connecting comb teeth pairs with distinct spacings to the external circuit, see Fig. 4.2 a). A photograph of both mounted sample geometries is shown in Fig. 4.6.

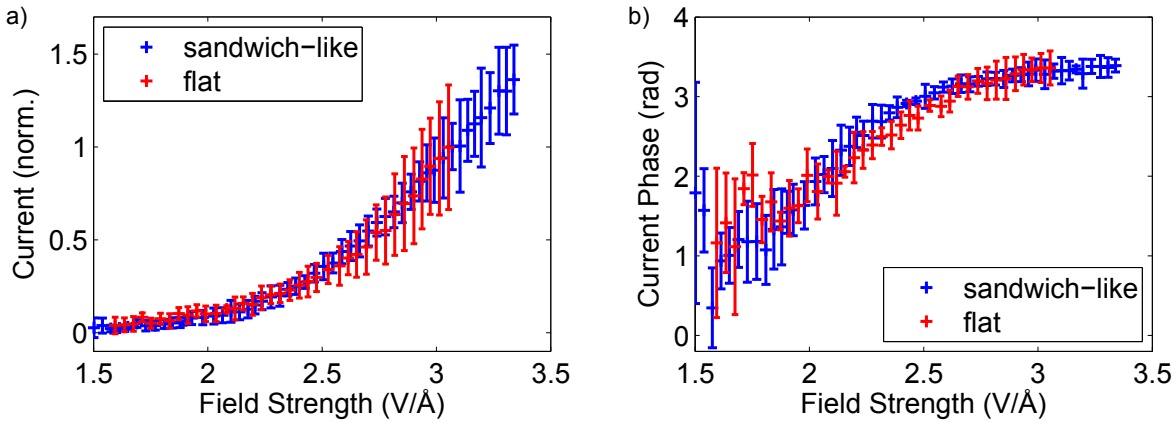

Figure 4.5: Flat versus Sandwich-Like Geometry. a) Scaling of the current amplitude with field strength, normalized to the amplitude at maximum field strength for the flat structure. b) Scaling of the current phase with field-strength. In all cases, data points are averaged over five independent scans and error bars correspond to the standard deviation.

The results of a series of intensity scans comparing the sandwich- with a comb-like structure taken with the upgraded setup 2 in fused silica are depicted in Fig. 4.5. The electrode gap sizes are 50 µm and 100 µm, respectively. The data points are the average of five independent intensity scans at different sample positions each, the errors bars are given by the standard deviation. The signal amplitude curves are scaled by the respective current at 3 V/Å. The unnormalized signal of the sandwich-like geometry is about twice as high as for the comb-like structure. The agreement of both amplitude and phase scaling in the range of the error bars is excellent. The damage threshold for the sandwich structures is higher than for the flat geometry and exceeds the value of (2.6 ± 0.5) V/Å determined by Bothschafter [79]. This is probably due to the fact that the thickness of the samples used in these experiments is larger which reduces the mechanical stress and the surface defects introduced by the polishing procedure.

There are several advantages and disadvantages for the two sample designs. The most important ones are summed up in the following:

- Manufacturing: For the sandwich-like geometry, the polished substrate can be coated in a standard coating facility. A 10 mm times 10 mm substrate can easily be cleaved into four samples. This makes the manufacturing process relatively simple. However, the minimum electrode distance is defined by the minimum thickness of the substrate which the crystal manufacturer can provide. This depends on the mechanical properties of the crystal in the required orientation during polishing. On the other hand, the flat geometry samples need a lithographic electrode structure. Due to the flexible mask design, the electrodes can take a variety of forms with a large range of distances.

- Reproducibility: While the lithographic electrode structures of the flat samples are reproducible to a high degree, the cleaving introduces some difficulty for the sandwich-

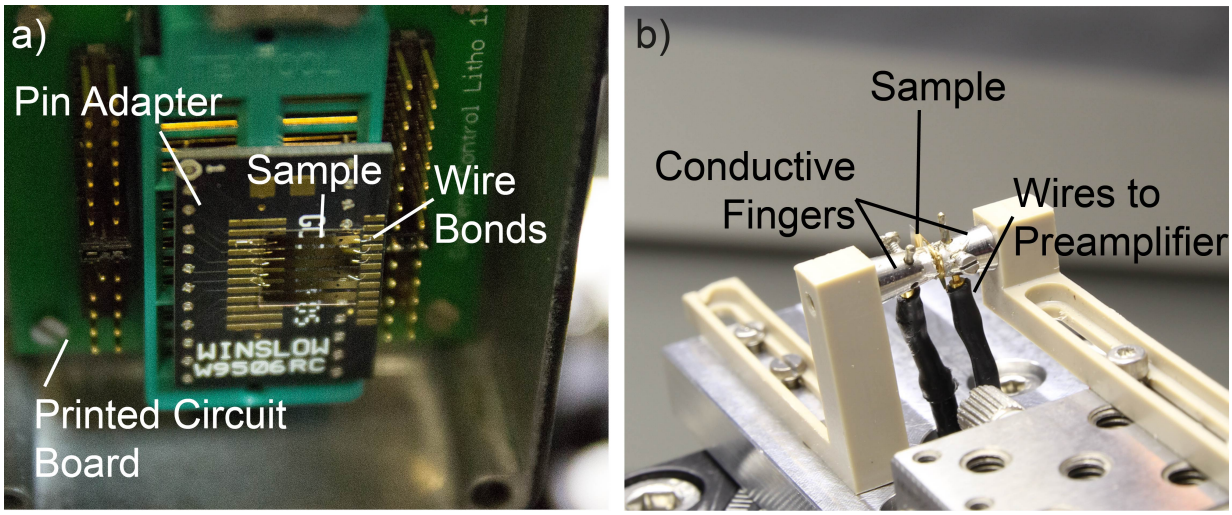

Figure 4.6: Photograph of Mounted Samples. a) Flat geometry, wire bonded to pin adapter. b) Sandwich-like structure, clamped between two conductive fingers.

like structures. In the case of amorphous materials and certain crystal orientations of crystalline samples, it produces smooth surfaces. For other crystal directions however, cleaving might result in steps and other surface defects.

- Mounting: Due to its bulky electrode, the sandwich-like samples can easily be mounted by clamping them between two conductive fingers, see Fig. 4.6 b). The flat samples on the other hand usually have a more delicate electrode structure which has to be connected to the outer measurement circuit by wire bonding, Fig. 4.6 b).

- Alignment: For the flat samples, the back reflection of the incident laser beam gives a very good indication of the position relative to the electrode gap and the tilt of the sample, which can be corrected. This back reflection is typically not visible from the cleaved substrate surface in the sandwich-like structures. This results in an uncertainty in the alignment since the tilt cannot be easily corrected.

- Signal-To-Background Ratio: The signal is typically higher for the sandwich-like structure, probably due to the larger electrode area which can collect the separated charge. At the same time, the background is lower since less light is incident on the electrodes where it can accelerate the free metal electrodes. Only with these samples, it has been possible so far to detect induced currents generated from single laser shots [63].

- Damage Threshold: For the same reason the background is low, the damage threshold of the sandwich samples is higher than for the flat structures. Higher field strengths can be applied.

Considering all these factors, it can be concluded that flat samples are advantageous if a high reproducibility in the electrode geometry as well as the alignment is necessary.

This is why this sample geometry is chosen for the electrode-focus-distance studies in Subsection 4.3.3. In order to study a large range of applied field strengths and in case a large number of samples is needed for good statistics, the sandwich-like structures are the better choice. For this reason, they are used in Section 4.4.

4.3.2 Bulk versus Surface Contributions

This subsection tries to answer the question if the excited electrons which account for the laser-induced current stem from the surface of the illuminated material or from the bulk. The fact that the signal from fused silica tips [63] as well as the flat structures is on the same order of magnitude as the one from sandwich-like geometries, where the light can propagate in a waveguide-like structure, suggests that the surface contribution is at least the dominant one. This is supported by strong-field ablation studies which find a strong confinement of the excited carriers and the resulting damage morphology to a few micrometers behind the surface [7, 157].

Together with Prof. Dr. Özge Sağlam from the group of Prof. Dr. Johannes Barth at the Technische Universität München, we designed a sample with a step-like electrode structure where the effective electrode length can be scanned by moving the sample perpendicular to the beam direction, see Fig. 4.2 b). The width of each step is about 1.6 mm. The electrode length can be varied between approximately 5 µm and 30 µm. The exact length of the step is determined by microscope pictures of the front and the mirror-inverted back of the lithographic structure.

The alignment of the lithography mask close to the illuminated surface of the sample is crucial to make sure the surface contributions from the induced current are collected. This requires a very clean substrate edge, which can be achieved by laser cutting (MDI SCHOTT Advanced Processing GmbH). Borosilicate glass with a thickness of 50 µm is chosen as substrate material because it possesses superior thermal characteristics over other types of glasses for this technique, with a low expansion coefficient of about $30 \times 10^{-7}\,\mathrm{K}^{-1}$ to $60 \times 10^{-7}\,\mathrm{K}^{-1}$ [171].

Fig. 4.7 shows the results of two independent measurement series with the same sample. The dependence of the maximum induced current from the electrode length is plotted. To vary the electrode length, the sample is shifted sideways with respect to the focus, thereby allowing it to illuminate different parts of the step-like electrode structure. The sample height and the other experimental parameters like power and focusing are kept constant. One of the scans is taken before, the other one after the laser upgrade. They are normalized to their respective maximum value for comparison. A clear trend is visible for the longer electrode lengths: After a propagation length of about 20 µm to 30 µm, the signal saturates and does not even increase in the bulk electrode area with a metal-structure length of several millimeters. There is still a non-zero signal amplitude at the shortest electrodes of only a few micrometer length. No distinct phase shift can be observed. The signal scaling does not change in the applied field strength range between 1.5 V/Å and 3 V/Å.

The observed saturation length is about one order of magnitude smaller than the dispersion length (see Eqn. 1.27), which in the case of borosilicate with a GDD of about

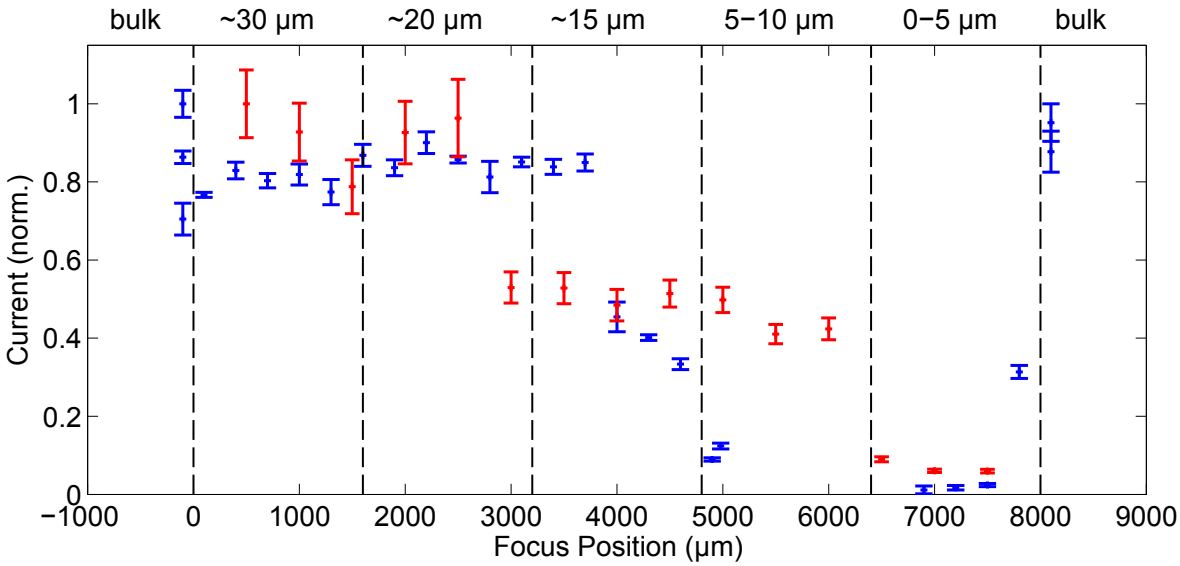

Figure 4.7: Current Scaling with Varying Electrode Length. The crosses show normalized current amplitudes for two independent scans, indicated by the different colors. The error bars are given by the standard deviation of five data points per position. Red: Taken with setup 1, Blue: Taken with upgraded setup 2. The dashed vertical lines indicate the areas with different electrode lengths, ranging from 30 µm to just a few micrometers.

49 fs^2/mm at 760 nm [160] results in 320 µm. This suggests that simple broadening of the pulse due to dispersion cannot be the dominant mechanism behind the saturation. The saturation length is on the same order as another important length scale: the coherence length. While the pulse travels through the material, the dispersion causes a CEP shift $\Delta\varphi_0$ given by

$$\Delta\varphi_0 = -\omega_0 L\left(\frac{1}{v_g} - \frac{1}{v_{ph}}\right) \approx -\omega_0 L\left(\frac{n(\lambda_0) - \lambda_0 n'(\lambda_0)}{c} - \frac{n(\lambda_0)}{c}\right) = -2\pi L n'(\lambda_0) \qquad (4.2)$$

where ω_0 is the carrier frequency, L the physical path length, v_g the group and v_{ph} the phase velocity, $n(\lambda)$ the wavelength-dependent index of refraction and $n'(\lambda)$ its first derivative. This phase shift has to be taken into account when adding the current generated in different depths of the sample. In case of borosilicate, a propagation distance of about 22.7 µm leads to a CEP slip of π which means that the current generated this far inside of the sample should have the opposite sign from the one generated directly at the surface. Of course this is an oversimplified picture because it only holds in case nonlinear propagation effects are negligible, but this coarse estimate fits well to the experimental observations.

There are several difficulties in the interpretation of this data which might be overcome with different sample designs, presented in the following.[1] Due to the current sample

[1] I gratefully acknowledge fruitful discussions with Dr. Tim Paasch-Colberg, Prof. Dr. Özge Sağlam, and Viktória Csajbók on potential electrode designs.

geometry, we can only interpret the signal scaling with electrode length, not with propagation length in the active material. Since the exact mechanism describing how the signal is coupled into the external circuit is not known to date, we can only speculate if restricting the propagation length would result in the same behavior as restricting the charge collecting electrode. A sample design which circumvents this problem is shown in Fig. 4.8 a). Unfortunately, etching such a structure is difficult due to the high etching resistivity of glass [172].

Another idea for the improvement on the sample design aims on the structure of the electrode. Since the electrode length in the used sample changes along the focus position, so does the area for collecting the generated charge carriers. Since we know that the generated current can still couple efficiently into electrode a few 100 µm away in the polarization direction, we cannot exclude that the current generation in the present case is even more localized in depth than the 20 µm to 30 µm which we experimentally determined. This would explain why we do not observe a distinct phase shift in the measured current. We can thus only put this value as an upper limit on the current generation depth. An alternative electrode structure, which keeps the electrode area constant for different generation depths, is presented in Fig. 4.8 b). The thin electrode stripe can collect current from different depths in the sample while maintaining a constant area. However, an accurate model of the current detection in the external circuit is required for all future sample designs to make claims on the generation depth of the optical-field-induced currents.

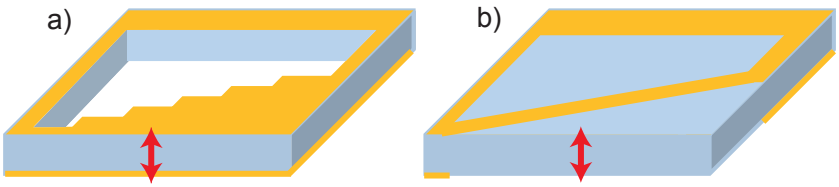

Figure 4.8: Outlook Propagation Samples. a) Step-like etched substrate and gold electrode. b) Substrate with thin, angled gold electrode. In both cases, the electrode structure on the bottom is the mirror image of the visible structure on the top. The red arrows mark the position of the focus and the polarization direction used in the experiments.

4.3.3 Different Electrode-Focus Distances

In experiments on interfering one-and-two-photon pathways in GaAs, it was found that the phase-dependent injected current depends critically on the distance between focus and electrode [95]. In order to investigate which role the electrode-focus distance plays in the detection of the optical-field-induced currents and to find the optimal electrode gap for future applications, fused silica substrates with comb-like electrode structures featuring varying gap sizes are used, see Fig. 4.2 c). In two different types of experiments one parameter determining the spatial distance between focus and electrode is varied.

Variation of the Focus-Electrode Distance The focus size is kept constant at 52 µm while the gap distance is changed by moving the sample with respect to the focus along the gap direction. The measured current shows the behavior depicted in Fig. 4.9. Setup 2 is used for this measurement. The field strength is about 2.3 V/Å. Two different regimes

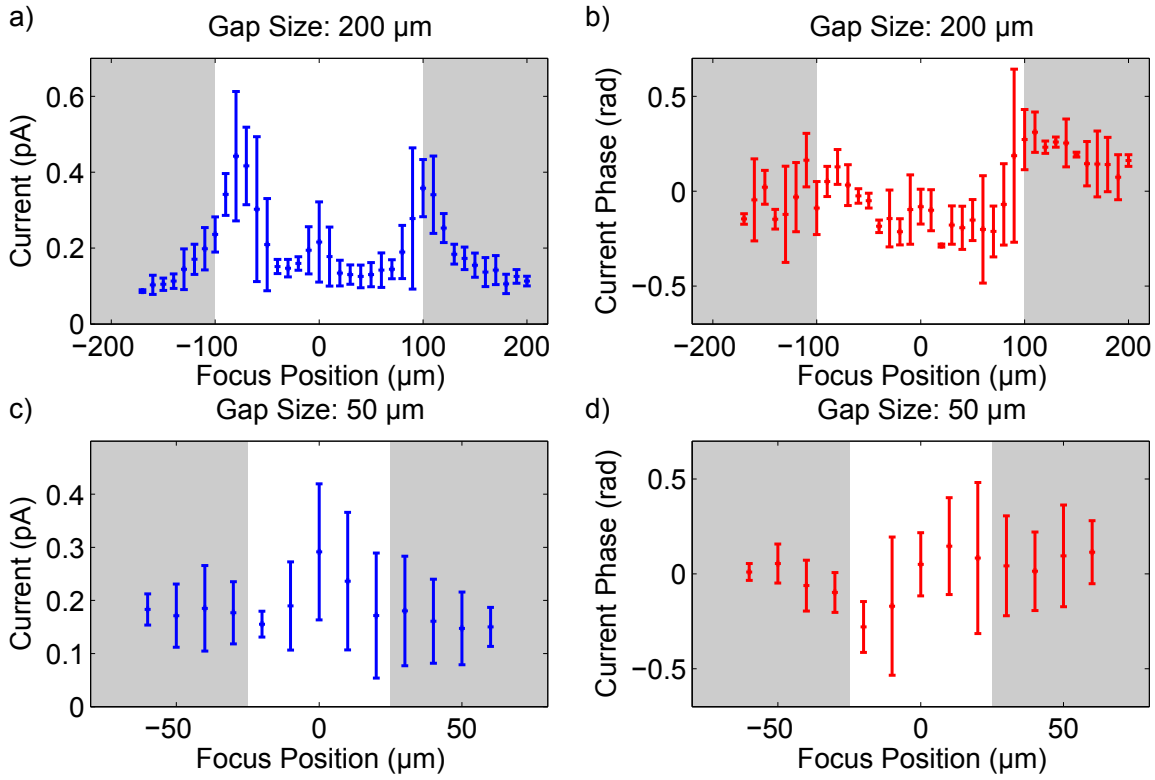

Figure 4.9: Current Scaling versus Electrode-Focus Distance. Left column: Current amplitude with respect to the focus alignment relative to the electrode. Right column: Current phase with respect to the focus alignment relative to the electrode. Upper row: Amplitude and phase for 200 µm gap. Lower row: Amplitude and phase for 50 µm gap. The gray areas indicate the electrode position. a) For the larger gap, two local maxima close to the electrode can be observed. c) For the smaller gap, the maximum is in the middle between the two electrodes. b) A slight phase shift towards the electrodes is visible. d) No distinct phase shift is observable.

are investigated: The regime where the electrode gap size is on the order of the focus and the regime where it is bigger. To this end, the same experiment is conducted for electrode gap sizes of 50 µm and 200 µm separately.

For the larger gap size, two local maxima close to the electrodes can be distinguished while the signal drops in the middle of the electrode gap. For the smaller gap, the maximum lies in the center between the two electrodes. The phase in both cases changes on the range of 0.5 rad. In the case of the 200 µm gap, there might be a slight positive shift of the phase towards to electrodes where the signal amplitude increases. For the 50 µm gap, no clear

trend can be observed.

The signal scaling with focus-versus-electrode position agrees well with measurements on interfering one- and two-photon absorption in GaAs [95] and photoconducting terahertz transmitters [173, 174]. Roos et al. [95] argued that the enhancement close to the electrode might be due to ballistic transport of the charge carriers which is influenced at the Schottky barrier through band bending. Huggard et al. [173] suspected that the electrode structure leads to a highly nonuniform field with a geometrical enhancement of the electrostatic gradient at the interface while Ralph et al. [174] considered in addition the influence of trap-enhanced fields near the electrode. Although the origin of the enhancement cannot be clarified at this point, the fact that a similar increase of the signal, which we detect in the nonperturbative strong-field regime, occurs in both the linear and the low-order nonlinear current generation, points to similarities in the current detection process.

Variation of the Electrode Distance The electrode-focus distance can also be varied by changing the distance of the metal electrodes. Keeping laser power and focus size constant, only the electrode gap is varied by shifting the sample between subsequent scans in order to illuminate different electrode gaps between the comb teeth. Setup 1 is used for these measurements. To make sure that the focus is nicely centered between the electrodes, its alignment is monitored by observing the symmetry of the reflected pattern. For each electrode gap size of 50 µm, 100 µm, 150 µm, and 200 µm, three to six independent scans on five different samples are performed. The field strengths range between 1.68 V/Å and 2.36 V/Å. When fitting the dependence of the maximum signal with respect to the electrode gap size, we find a power law relationship:

$$S_{max} = a\, x^b \ , \tag{4.3}$$

with $b = -1.70 \pm 0.68$. The value for b is the mean of a nonlinear least square fit with the standard deviation from the measurement series on the five different samples, the uncertainty is given by the standard deviation. The absolute current amplitude varied over the range of about one order of magnitude from sample to sample so the five data sets for different samples were fit separately. The left side of Fig. 4.10 shows the data and corresponding fit for one exemplary sample. As can be seen in the right side of the same figure, no pronounced phase shift with respect to the electrode gap size can be detected.

Assuming the schematic picture of how the separated charge is coupled to the external circuit depicted in Fig. 4.1, we can compare the measured value for b to what we expect from the lowest order charge-separated distribution: a dipole. The decrease in signal with larger electrode distance is actually smaller than would be expected from a dipole in the near field with an effective decrease of the electric field strength of $b = -3$. The electric field vector $\boldsymbol{F}$ at place $\boldsymbol{x}$ which originates from a electrostatic dipole $\boldsymbol{p}$ at place $\boldsymbol{x_0}$ is given by [17]

$$\boldsymbol{F}(\boldsymbol{x}) = \frac{3\boldsymbol{n}(\boldsymbol{p}\cdot\boldsymbol{n}) - \boldsymbol{p}}{4\pi\epsilon_0\,|\boldsymbol{x}-\boldsymbol{x_0}|^3} \ , \tag{4.4}$$

where $\boldsymbol{n}$ is the unit vector pointing from $\boldsymbol{x_0}$ to $\boldsymbol{x}$. A potential explanation for the deviation of the experimental scaling from that of a dipole field is the finite laser spot size which

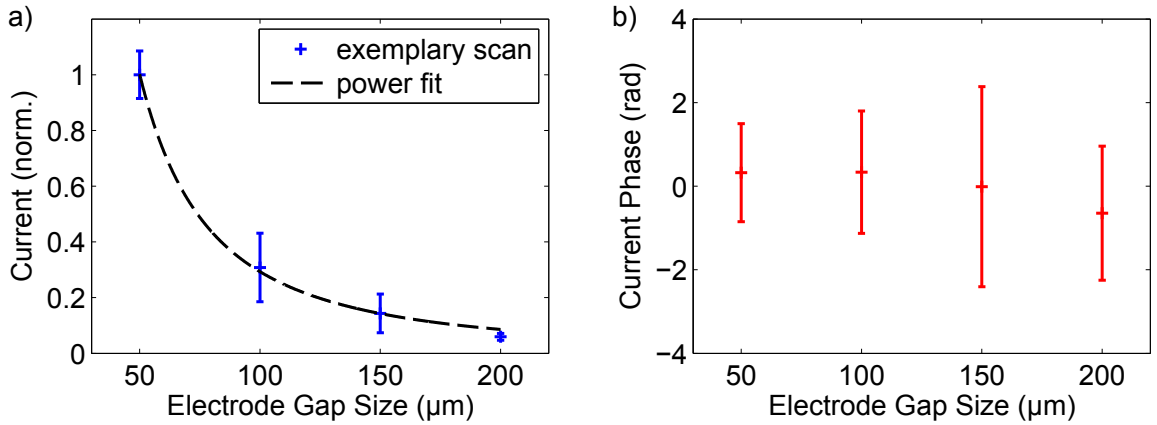

Figure 4.10: Current Scaling versus Electrode Gap Size. a) Exemplary data set: current scaling versus electrode distance at 2.36 V/Å with respective power fit. The error bars stem from the standard deviation. b) Current phase mean averaged over all data sets. The uncertainty is given by the standard deviation of all scans per gap. A constant offset between the data sets is subtracted.

generates an extended charge distribution. Especially for small electrode gaps which are close to the focus size, the dipole approximation might no longer be valid, so a more thorough modeling of the charge distribution and its resulting electric field is needed, which is beyond the scope of this work.

The two measurement series presented in this section show how sensitive the measured signal is with respect to the focus-electrode distance and how important it is therefore to decouple power attenuation from focus size changes. The experiments on intensity scaling in different materials, which is presented in the following section, therefore utilize crossed wire-grid polarizers for attenuation rather than an opening and closing of the iris as in previous publications [4, 62].

4.4 Dependence on Sample Material

In this section, three crystalline materials with different electronic properties are investigated in order to find out how the current and its scaling with respect to the applied field strength depend on the band gap. Preliminary results on the signal scaling where published in [175]. The samples consist of 250 µm thick dielectric substrates of crystalline CaF_2, BaF_2, and MgO in sandwich-like geometry. The three cubic materials have the same space group $Fm\bar{3}m$ and a band gap of 12.1 eV, 9.2 eV, and 7.8 eV, respectively (see Table 4.1). At an excitation energy of $\hbar\omega \approx 1.63$ eV, a valence to conduction band transition thus requires seven to eight, five to six, and four to five photons, respectively. The polarization of the laser is parallel to the [111] direction of the crystal which corresponds to an acceleration of the electrons in the $\Gamma - L$ direction in the Brillouin zone. Band structure calculations of CaF_2, BaF_2, and MgO can be found in [176], [177] and [166]. The band

structure of MgO calculated with Wien2k [178] is depicted in Fig. 4.11.

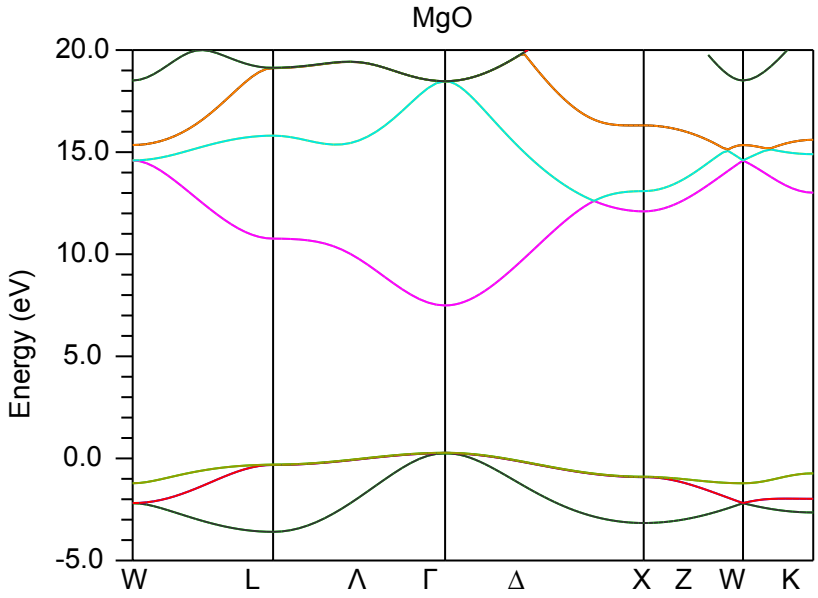

Figure 4.11: Band Structure of MgO. Calculated with Wien2k [178]. Courtesy of Dr. Stanislav Kruchinin.

In order to avoid any enhancement effect which was observed close to the metal coating in Subsection 4.3.3, the focus is aligned to the center between the electrodes. The observed signal enhancement is material-dependent and strongest in MgO. A potential explanation for this observation lies in interface trap states. In contrast to other dielectrics, time-resolved studies of the dielectric breakdown have shown that trapping in the bulk crystal does not occur in MgO [157]. This would make the detection of the current generated close to the metal electrode surface, where the role of stabilizing the charge separation can be resumed by interface traps, more efficient. In order to check this conjecture, a more detailed analysis of the role of trapped states, especially at the dielectric-metal interface, is required. The outlook part of this chapter provides some ideas for further experimental investigations using time-resolved terahertz studies.

Fig. 4.12 shows the amplitude and phase of the laser-induced current as a function of the externally applied field strength. The error bars represent the standard error of the mean of multiple data sets for each material. The number of scans used for data analysis were 25 for MgO, 18 for BaF_2, and 12 for CaF_2. The measured currents range up to about 5 pA in BaF_2, 4.7 pA in CaF_2, and 0.3 pA in MgO. In all three cases, the current phase shows an increase with field strength. It is most evident in MgO and least pronounced in CaF_2, the material with the lowest dielectric constant. This is agreement with previous studies [62], where the phase shift has been attributed to the screening field in the dielectric. At least in the linear regime, this field is smallest in CaF_2.

The good statistics and the wide range of applied electric fields allow for a closer examination of the scaling behavior. Plotting the data points on a double logarithmic scale

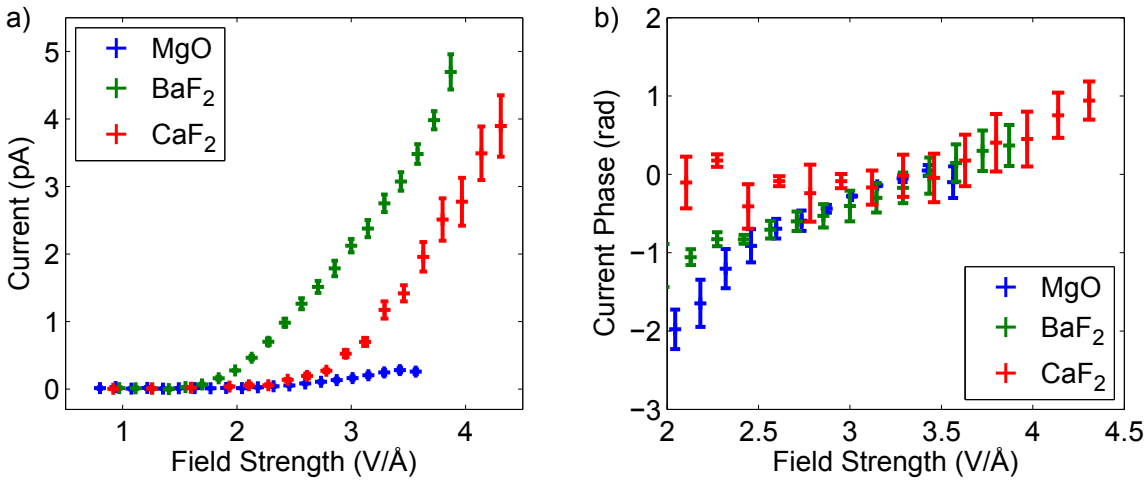

Figure 4.12: Intensity Scaling of Current for MgO, BaF_2, and CaF_2. a) Maximum current with respect to field strength. b) Relative phase of the maximum current. The error bars denote the standard error of the mean of the measurement series for each material.

as depicted in Fig. 4.13 as blue curves, shows that the signal amplitude follows a power law, the order of which changes with electric field strength and is overall smaller than expected from the multi-photon absorption picture. The local power scaling is depicted in green. In all three cases, a saturation behavior can be observed which slows down the increase of current with field strength. The saturation effect has been observed similarly in studies of the excited state population close to dielectric breakdown. However, the initial population scaling in these experiments agreed well with the multi-photon picture [157].

A slower than expected increase of the signal with electric field strength could have several causes, among them the shielding of the electric field [65] and/or the closing of multi-photon channels which has been observed in photoemission experiments from metal films [179] and nanotips [180]. At the current stage of this work, we cannot find a definite answer for the low-order power scaling. A careful modeling of the screening dynamics in these materials and geometries is needed to interpret the data more confidently and is currently being investigated by Dr. Stanislav Kruchinin.

However, a first indication that the transport of the charge carriers into the conduction band plays a role in the scaling is given by semiclassical simulations by Dr. Nicholas Karpowicz. The calculations take into account the acceleration of the electrons in the conduction band (calculated with Wien2k [178]) and show a low power order scaling of the current versus intensity, which gradually slows down with higher field strengths. The scaling behavior for the three investigated materials is depicted in Fig. 4.14. It needs to be pointed out that the x-axis in these graphs refers to the internal electric field while for the experimental data in Fig. 4.12 and Fig. 4.13 the externally applied, unshielded electric field is given.

The simulation features dips in the current amplitude and a π phase shift at a certain field strength (see Table 4.1). Once the electric field reaches these strengths, it is strong

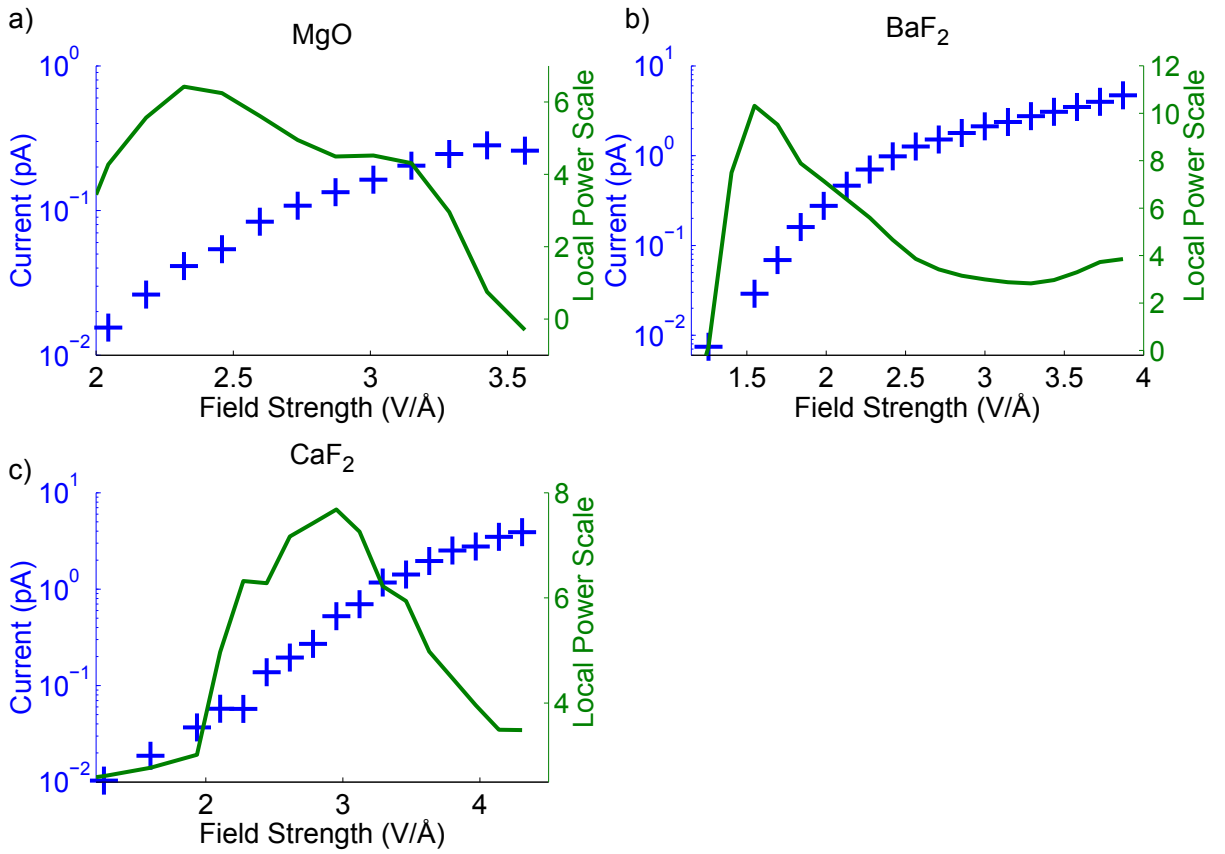

Figure 4.13: Logarithmic Scaling and Local Power Law Scaling for Different Materials. a) MgO, b) BaF_2, and c) CaF_2. Blue: Maximum current on logarithmic scale. Green: Local power law scaling.

enough to push the electron far to the edge of the Brioullin zone, where it reappears on the other side. This makes the current change sign. These features are a direct result of Bloch oscillations, introduced in Subsection 1.2.2. However, they are not present in the experimental data although the calculated critical Bloch field strengths summarized Table 4.1 are exceeded, most clearly for BaF_2, even if screening is considered. The most likely reason why we do not see the simulated features in the experimental data is the tunneling of electrons to higher lying conduction bands before they are reflected. The probability of this tunneling depends strongly on the exact band structure and the energy separation between the first conduction band and higher lying bands. Due to the strong ionic nature of the fluorite crystals, the Wien2k calculations seem to fail in reproducing the higher lying conduction bands properly. While there are advanced band structure models which show a clear separation of the first conduction band in $\Gamma - L$ direction for BaF_2 [181], recent many-body perturbation schemes predict an overlap of several bands there [177]. In the latter case, the accelerated electron propagates in higher lying bands and no Bloch oscillations can be observed.

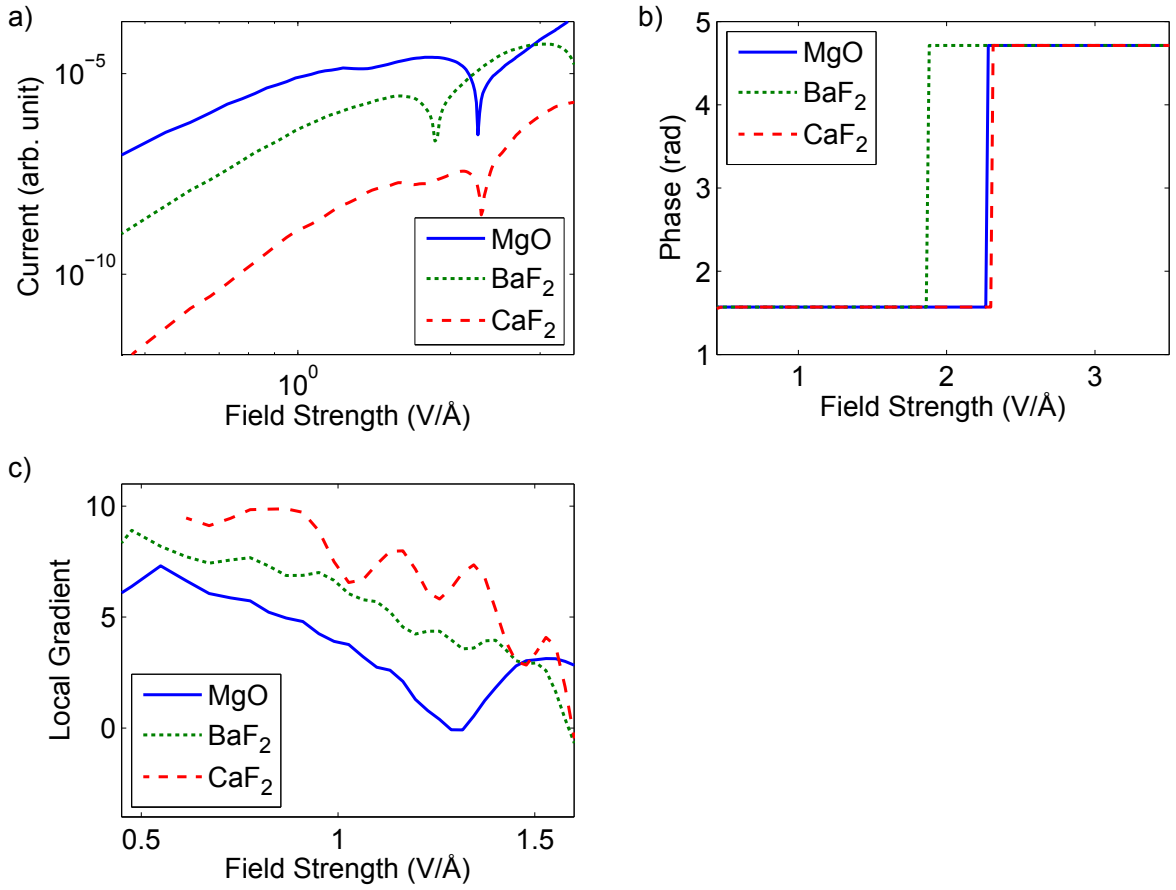

Figure 4.14: Simulated Intensity Scaling for MgO (blue solid line), BaF_2 (green dotted line), and CaF_2 (red dashed line). Upper left: Maximum current on logarithmic scale. Upper right: Phase of maximum current. Lower left: Local power law scaling corresponding to the gradient in the double-logarithmic plot for low field strengths. The x-axis refers to the internal electric field. Courtesy of Dr. Nicholas Karpowicz.

4.5 Outlook

This chapter has presented experimental evidence on how sensitively the optical-field-induced current reacts to changes in the sample geometry and material. While the presented findings cannot resolve all uncertainties connected to the initially posed questions, they provide recommendations on the sample choice and measurement procedure for future applications. The main results are summarized here:

- The sandwich-like structures deliver a higher signal-to-background ratio and are easier to handle than the flat samples - see Fig. 4.2 a) and c). However, the manufacturing and alignment of the latter are more reproducible which makes them better suited for investigating geometric aspects of the current generation and detection. Both sample structure show the same behavior in terms of amplitude and phase

scaling with field strength.

- Thanks to the propagation samples with a step-like electrode structure - see Fig. 4.2 b) - we can give an upper limit on the generation depth of the field-induced current in the range of 20 µm to 30 µm. This threshold is found independent of the field strength in the investigated range between 1.5 V/Å and 3 V/Å. With the proposed sample structures in Fig. 4.8 a more accurate localization of the current generation should be possible.

- The electrode-focus distance has great impact on the signal strength. It is important to find a balance between maximizing the signal and keeping the light exposure of the electrode low, since it leads to a high background current and a low sample damage threshold due to metal ablation. This works best for electrode distances on the order of the focus diameter. Decoupling the field strength adjustment from changes in the focus size is indispensable for an accurate investigation of the scaling behavior. The reproducibility of the local signal maxima close to the electrodes point to the involvement of same coupling mechanisms of the separated charge to the external circuit as is present in the coherent control experiments in GaAs.

- Comparing the amplitude and phase scaling of three dielectric materials shows a slower increase with field strength than expected from a simple tunneling or multi-photon absorption picture. The observed phase shift is smallest in the material with the highest band gap which makes CaF_2 a promising candidate for a CEP detection device [62]. We do not see any features of Bloch oscillations in the range of investigated experimental parameters which is likely due to the tunneling of the excited charge carriers into higher conduction bands.

One of the difficulties in interpreting the field-induced current data stems from the nature of the current as an observable. It is measured as a temporal average over one laser pulse and as a spatial average involving the laser spot size as well as the electrode area. This complicates the disentanglement of the physically relevant mechanisms in the current generation and detection process. Other experimental schemes can be combined with the ultrafast current measurements and thus add information on the underlying physical processes:

- Two-color optical-field-induced currents: Employing the two-color interferometric setup, the injection and drive processes can be disentangled in an unprecedented way. In previous one-color injection-drive experiments [4], the injection process was limited only to one half-cycle of the drive. If the two-cycle NIR pulse is used for injection and the SWIR pulse for the drive, the injection is confined to a temporal window which is about three times shorter than the half-cycle of the drive wavelength. This allows an accurate sampling of the SWIR waveform as shown in Chapter 5. Switching the role between injection and drive can lead to a detectable cutoff in the sample NIR spectrum. This measurement carries information of the time scale on

which the injection takes place and — as will be discussed in Section 5.4 — on the applicability of classical transport models for the strong-field excited carriers.

- Attosecond polarization spectroscopy: With slight alterations in the geometry of the current setup and the mounting of the sample, it is possible to detect the light transmitted through the sample. As has been shown by Sommer et al. [35], temporally resolving the waveform of the pulse interacting with a dielectric at low and high intensities can reveal details of the dynamic nonlinear polarization response. In contrast to the current detection, this optical scheme delivers sub-cycle time-resolved information. If these studies are performed with the SWIR source, the field characterization can be performed using the EOS setup introduced in the previous chapter.

- Field-induced second harmonic (FISH): Using the two-color interferometric setup as a pump-probe setup, the FISH signal [182] can be used to observe the lifetime of the strong-field-induced polarization. SHG can only be observed in media with a broken inversion symmetry, see Subsection 1.2.1. Thus, if the infrared pulse is sent through a centrosymmetric medium, there is no detectable SHG signal unless the inversion symmetry is broken by charge carrier separation in the strong field of the white-light pulse. Recording the SHG signal with respect to the delay of the two arms, the time-dependent charge separation can be measured, which provides important information on the dynamics and the lifetime of the laser-induced charge separation. Similar information can be deduced from time-resolved terahertz spectroscopy [47] which records the signal radiated by the accelerated charge carriers. Thus, it is sensitive to changes of the charge separation rather than the charge separation itself, like FISH.

- HHG spectroscopy: The strong-field excitation of charge carriers in a solid has recently lead to the exciting discovery of HHG from bulk solids [8, 9]. Although the physical mechanism behind this phenomenon is still under discussion, it was previously shown that the emitted HHG spectrum carries detailed information on the conduction band dispersion [10] and the interference of excitation pathways from different valence and conduction bands [61]. Comparing this information to the ultrafast current measurements could provide further insight in the role of inter- and intraband processes.

Chapter 5

Strong-Field Solid-State Sampling

After studying the properties of optical-field-induced currents related to the geometry and active material of the used samples, this chapter introduces their practical application in a novel pulse characterization technique. As was pointed out in previous chapters, the rapid development of few-cycle phase-stable sources and their promising applications in strong-field physics calls for compact metrology devices capable of providing complete information on the electric field of a waveform.

Chapter 3 has introduced EOS as a powerful characterization tool in the SWIR to NIR regime, featuring great sensitivity, a high dynamic range, large detection bandwidth, and compact footprint. However, the spectral cutoff has until now been limited to 235 THz, which corresponds to a wavelength of 1.27 µm. In order to resolve higher frequencies, a sampling pulse shorter than the 5 fs pulse employed in this work is needed. This requires the generation and compression of a broadband white-light spectrum ranging to the ultraviolet and poses increasing experimental difficulties as the test frequencies, which need to be characterized, approach the visible spectral range. Since phase-stable light sources like OPCPA synthesizers are aiming for the generation of spectra ranging from the infrared down to the ultraviolet [15, 183], a novel approach for the electric-field characterization of these waveforms is needed.

Two metrology techniques with high cutoff frequencies were introduced in Subsection 2.1.3. Both use ultrashort gates generated by the strong-field interaction of a NIR field and a gas target to temporally resolve the unknown test waveform. The novel sampling scheme described in this chapter demonstrates for the first time the utilization of a strong-field-driven effect in a solid as an ultrashort gate for optical metrology. In the following, this technique will be referred to as strong-field solid-state sampling (SFS). Like EOS, the compact setup of SFS works in ambient conditions and can easily be integrated into existing experiments. It thus presents a promising alternative to attosecond streaking, especially for solid-state measurements which do not necessarily require a dedicated vacuum setup.

It has been demonstrated previously that nonlinearly induced currents are sensitive to amplitude and phase changes in the electric field [184] and can be used as a solid-state CEP detection device [62]. This chapter investigates for the first time the potential of

optical-field-induced currents for complete waveform characterization. In the first two sections the concept and the experimental setup of SFS are presented. Drive-field assisted carrier-injection is discussed in Section 5.3 as a cause of distortions of the measured waveform at high test fields. Then Section 5.4 presents a juxtaposition of the SFS and EOS characterization of a broadband SWIR waveform, which allows for a benchmarking of these two techniques. Lastly the spectral response and the potential high-frequency applications of the metrology regime are discussed.

5.1 Concept

The basic concept of SFS is maybe best understood in the semiclassical two-step picture of ultrafast current generation (see Section 1.4): The drive pulse is the unknown test waveform and a second pulse is employed for the injection of the charge carriers into the conduction band. The excitation of the electrons to the conduction band, which is confined to approximately one half-cycle of the injection pulse, can be temporally delayed with respect to the test waveform and thus acts as a gate for the drive process. The excited charge carriers, which are delocalized in the conduction band, are accelerated by the electric field of the drive pulse. Their velocity, which is directly proportional to the current density (see Eqn. 1.62), thus gets modulated with respect to the delay between the sampling and the test waveform. This leads to a drive-field-induced charge separation which results in the measurable current. As will be discussed in the course of this chapter, the classical models for the intraband transport of the carriers fail to explain the experimental results. The limits of the classical description can be identified by comparison between the measured current and the electric field of the drive pulse, which is characterized by EOS.

In previous experiments using the two-pulse-scheme [4], it was already speculated that the current recorded with respect to the delay between injection and drive pulse can serve as a measurement of the electric field of the drive field. The current trace was therefore compared to the waveform characterized by attosecond streaking. However, the current measurement was performed in ambient air while the streaking measurement was performed in vacuum several tens of meters from the original experiment. This is problematic since not only the additional beam path and optics give rise to changes in the test waveform. The HHG process itself, which generates the XUV pulses needed for attosecond streaking, leads to a considerable frequency shift in the fundamental spectrum which depends sensitively on the focusing conditions [115, 114], see Subsection 2.1.3. Thus, a direct juxtaposition of the two experimental traces could not prove the applicability of the current measurement as a field characterization technique but provided a first indication towards its potential. The experiments showed that the frequency response of the current in the two-pulse-scheme is broadband, that the oscillations in the delay traces at a period of 2.5 fs correspond to the central wavelength of the drive pulse, and that a CEP-flip in the drive pulse is reflected in a corresponding phase-flip in the current.

In this work, the two-pulse current is directly compared to the waveform of the drive pulse, which can be determined by EOS in situ under nearly the same experimental condi-

tions. This permits a precise validation of SFS as a pulse characterization technique and helps identify the limits of the classical picture of the carrier transport process. The direct comparison with a well established metrology scheme furthermore allows a benchmarking in terms of spectral response, dynamic range, and signal-to-background ratio.

5.2 Experimental Setup

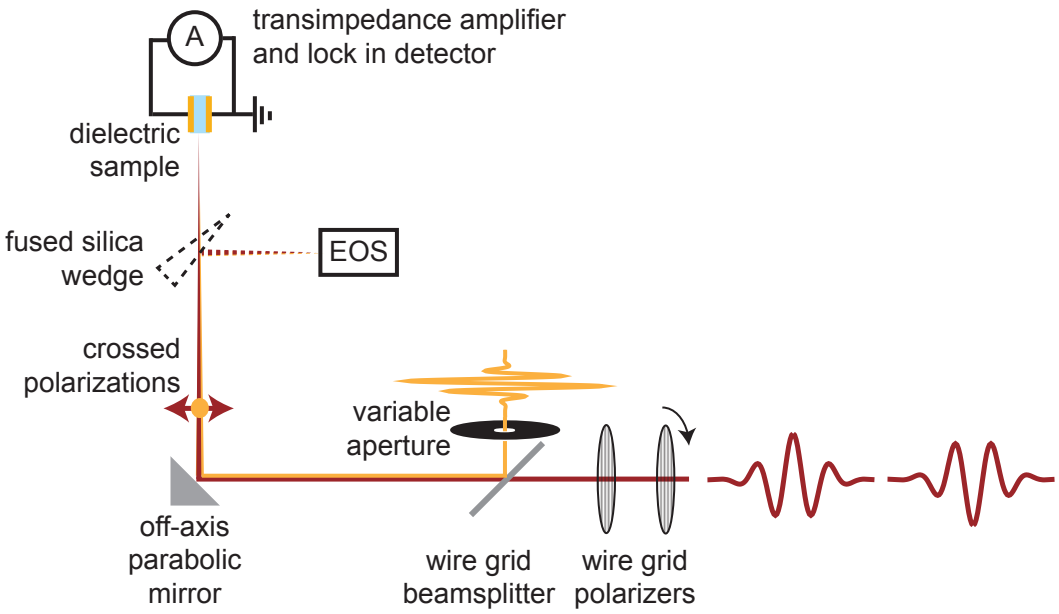

Figure 5.1: Experimental SFS Setup. The strong white-light few-cycle injection and the weak infrared few-cycle drive pulse are combined with a wire-grid beam splitter and focused onto a dielectric sample between the two metal electrodes. The beams can be attenuated via an aperture and crossed wire-grid polarizers, respectively. The polarization of the drive pulse is directed across the electrode gap, the polarization of the injection pulse is perpendicular. By flipping a fused silica wedge (dashed black) into the beam path, the two pulses can be guided to the EOS setup as depicted by the dashed lines. The CEP of the drive waveform is cycled in order to allow for heterodyne detection in both measurements.

The experimental setup is based on the two-color interferometer, which was introduced in Section 2.3 and used with slight modifications for the EOS measurements in Chapter 3. A schematic drawing of the SFS setup is depicted in Fig. 5.1. For the recombination of the white-light and the infrared arm, a wire-grid polarizer instead of a dielectric beam splitter is used. This has the advantage that the polarizations of both arms are cleaned and that the transmission wavelength is not limited to the SWIR range as was the case for the dielectric beam splitter. The wire-grid polarizer features a lower reflection efficiency

compared to the dielectric beam splitter which leads to a reduction of maximum available white-light pulse energy from 3 µJ to about 1.8 µJ.

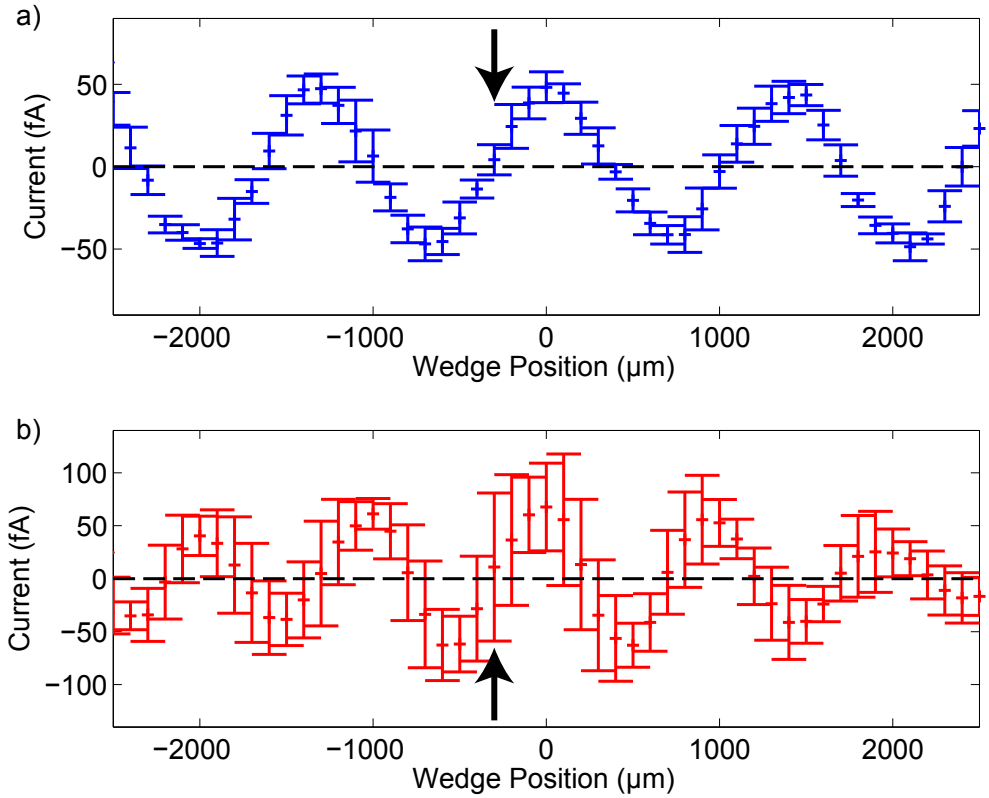

Figure 5.2: Single-Pulse Current Signals in SFS Setup. a) One-pulse signal of the infrared arm with the polarization across the electrode gap. b) One-pulse signal of the white-light arm with the polarization along the electrode gap. The data points are averaged over five independent scans, the error bars are the standard deviation. The black dashed lines indicate the zero level. The black arrows mark potential wedge positions close to the optimal compression point which minimize the one-pulse currents in the SFS measurement.

After recombining the two arms of the interferometer, they are focused by an off-axis parabolic mirror with a focal length of 100 mm to a diameter of about 40 µm for the white-light and 50 µm for the infrared beam. The field strengths in the focus lie on the order of 2 V/Å for the injection and below 0.2 V/Å for the drive pulse. The beam is aligned to the 100 µm or 150 µm gap between the two electrodes of a comb-like structure. These structures presented in Subsection 4.3.1 are chosen in order to minimize propagation effects in the sample (see Subsection 4.3.2) which could lead to CEP shifts or other distortions of the test waveform. The sample mount and the measurement circuit are the same as described in Section 4.2. In order to suppress the current generated from each arm separately, the CEP is adjusted accordingly with the help of two fused silica wedge pairs. One exemplary

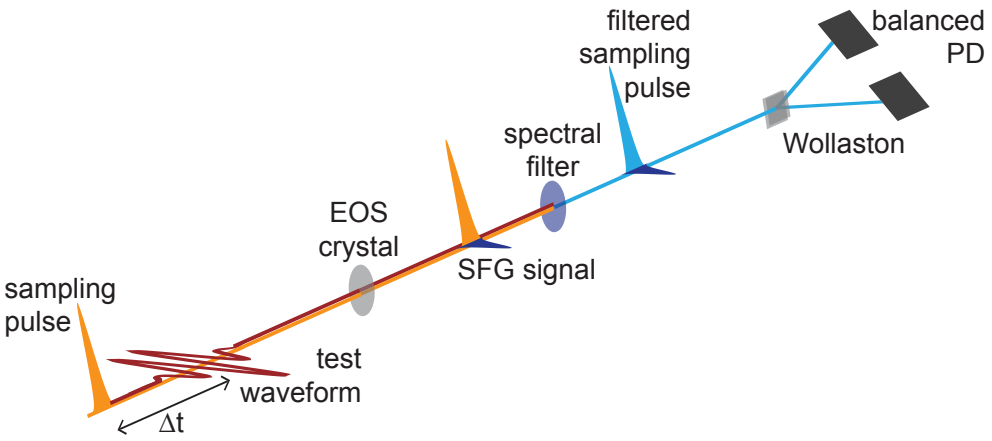

Figure 5.3: Modified EOS Setup. After recombining the test waveform and the sampling pulse with crossed polarizations, the pulses are focused into an EOS crystal (type II BBO). The orthogonally polarized SFG signal spectrally overlaps with the sampling pulse. This leads to an interference at the high-frequency end of the sampling spectrum which is selectively transmitted through a spectral filter. To detect the resulting polarization rotation with respect to the temporal delay Δt, the filtered pulse is sent through a tilted Wollaston prism and onto a balanced photodiode.

wedge scan for each arm is shown in Fig. 5.2, where the polarization of the visible/NIR arm is directed along the gap, the polarization of the SWIR arm across the gap. One applicable wedge position close to the optimal compression point for both arms is indicated by black arrows.

When flipping a fused silica wedge in the focusing beam, about 8 % of the visible/NIR and 0.6 % of the SWIR pulse energy are guided towards the EOS experiment. Two slight modification in the EOS setup compared to Section 3.2 have been implemented. Firstly, since the two-pulse current setup requires crossed polarizations between the injection and drive arm, the phase-matching condition has to be adjusted. Instead of the type I phase matching employed in Chapter 3, a 10 µm thick type II BBO crystal is used. Secondly, in order to simplify the calculation of the EOS response function which is needed for the deconvolution, the ellipsometer depicted in Fig. 3.1 is changed by removing the wave plate and tilting the Wollaston prism instead in order to project the polarizations of the SFG and the sampling pulse onto each other. The changes in the setup are schematically depicted in Fig. 5.3.

The experimental requirements for the two-pulse current generation are more demanding than in the case of EOS because the latter does not require a phase-stable sampling pulse. SFS is sensitive to CEP jitter in both arms as well as to timing fluctuations in the interferometer. The phase and timing jitter are characterized in Section 2.3 and Section 3.2.

5.3 Drive-Field-Assisted Carrier Injection

In a first set of measurements, we investigate if and in which intensity regime the current is proportional to the drive field. To this end, the power of the injection and the drive pulse is varied independently and the maximum amplitude of the generated current is recorded. While the SWIR beam size stays constant because the power on target can be changed via the transmission through wire-grid polarizers, the beam size and thus the focus size of the visible/NIR changes by adjusting an aperture to adjust the intensity. Since the simultaneous monitoring of the focus size during the measurement is not possible in the current version of the setup, the minimum focus size (corresponding to the maximum iris opening at full power) and the power for each aperture opening are measured. With these parameters, the radius of the white-light beam for determining the field strength in the focus is calculated using Eqn. 1.33. The results for the current amplitude scaling versus injection and drive field strength are depicted in Fig. 5.4.

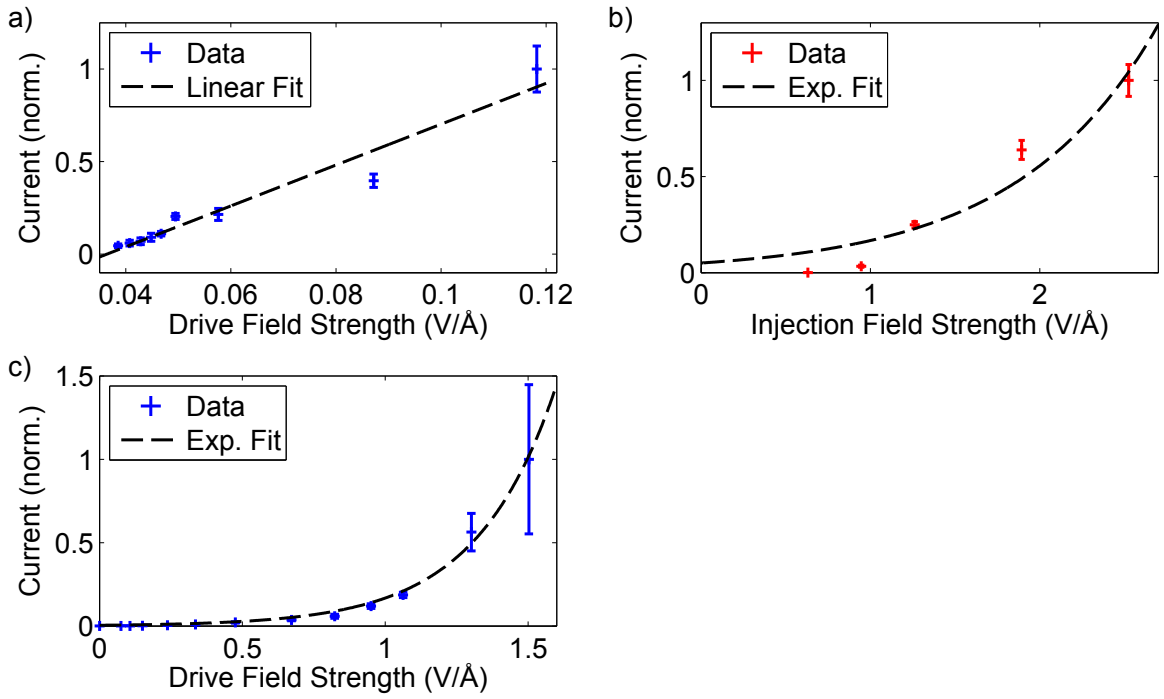

Figure 5.4: SFS Signal Scaling with Injection and Drive Field Strength. a) The scaling of the current amplitude with the drive field is linear at low field strengths. b) The scaling of the current amplitude with the injection field shows a steep rise and is compared to an exponential fit. c) The scaling of the current amplitude at high drive field strengths shows that the linear response breaks down and turns into an exponential behavior. The data points result from the mean of five scans for each field strength, the error bars from the standard deviation. The linear and exponential fits are depicted in dashed black.

The scaling of the current amplitude with intensity of the injection field shows a steep

increase which stems from the highly nonlinear nature of the carrier excitation. Due to the limited maximum pulse energy and the missing option to adjust power and focus size independently, the range of investigated intensities does not allow for a more exact determination of the scaling law. The latter issue can be resolved with the introduction of a pair of wire-grid polarizers like in the infrared arm. However, this requires a chirped mirror compressor with higher negative GDD due to the additional transmission through the polarizer substrate, which was not available for this set of experiments.

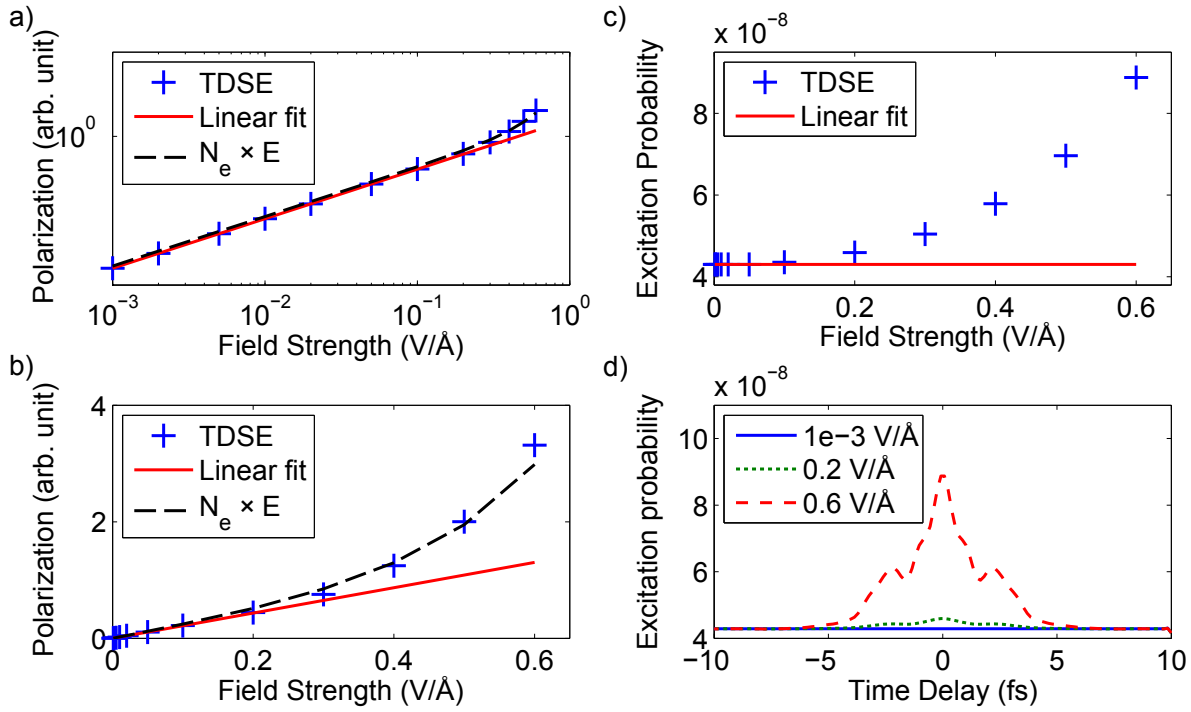

Figure 5.5: TDSE Simulation of SFS in Hydrogen. a) Calculated polarization for different drive field intensities (blue crosses), compared to a linear fit in the low field region (solid red line) and a curve proportional to the number of excited electrons N_e times the field strength E (black dashed line) in a logarithmic plot. b) Same data as a) in a linear plot. c) Excitation probability with respect to field strength (blue crosses) compared to a linear fit in the low field region (solid red line). d) Excitation probability with respect to the delay between injection and drive pulse for three different drive field strengths.

The drive field strength on the other hand influences the maximum signal linearly for low field strengths and clearly follows an exponential fit at field strengths of about 0.5 V/Å and above. This deviation from the linear scaling can stem from a contribution of the drive field to the number of injected carriers. In order to check this conjecture, Dr. Nicholas Karpowicz performed three-dimensional TDSE calculations for a hydrogen atom with I_P=13.6 eV. The atom is ionized by a strong-laser field and the freed electron is driven by a second electric field with crossed polarization. The injection photon energy is adjusted

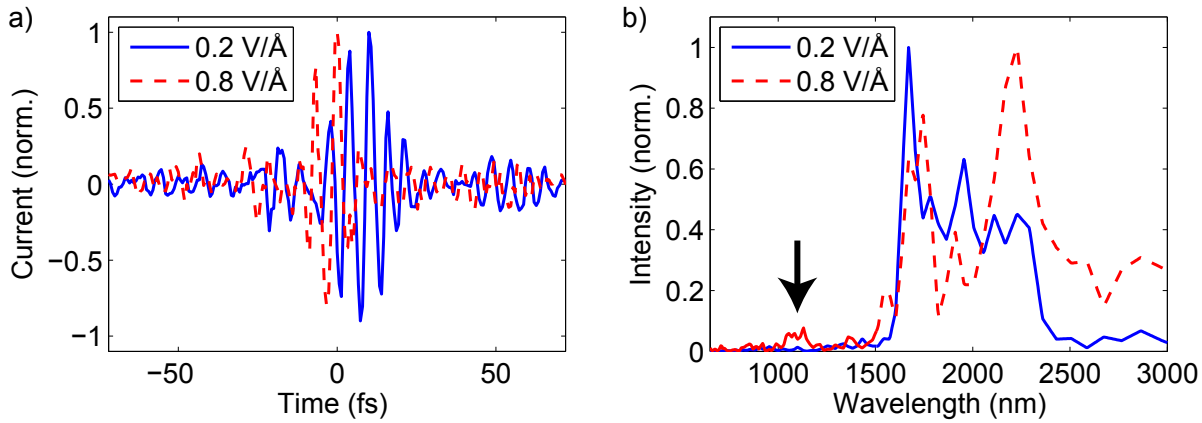

Figure 5.6: SFS Signal Distortions. SFS signal for two different drive field strengths, 0.2 V/Å (blue solid line) and 0.8 V/Å (red dashed line) without band-pass filtering. a) Directly recorded, normalized current traces. b) Spectral intensity of above waveforms. The black arrow indicates spectral intensity at the second harmonic of the fundamental frequencies.

to ω^* such that the ratio $\hbar\omega^*/I_P$ is the same as $\hbar\omega/\Delta_g$ in the experiment. As mentioned in Subsection 1.2.2, the strong-field ionization in atoms and dielectrica underlies to the same basic principles [185]. Thus, a comparison of the simulated injection mechanism in hydrogen and the experimentally investigated excitation in fused silica is justified.

The results for the polarization density are shown in Fig. 5.5. The simple atom model reproduces our experimental result in the solid surprisingly well: After following the drive field proportionally below 0.2 V/Å, the optical-field-induced polarization shows a steeper rise above this threshold. The simulation makes clear that this is due to the increased excited carrier density, see Fig. 5.5 b), which is only present in the temporal overlap region of drive and injection pulse, see Fig. 5.5 c). This points to drive-field-assisted ionization, also known as Franz-Keldysh effect [186, 187]. Clearly, above a drive-field threshold of about 0.2 V/Å, the disentanglement of the injection and drive process is not valid anymore and the semiclassical picture is not applicable.

The resulting SFS traces feature distortions both in the time- and frequency domain. Fig. 5.6 shows how high drive fields reshape the measured current and add spectral intensity also at the second harmonic of the fundamental frequencies. The intensity at even harmonics cannot be explained by the temporally symmetric variation of the charge carrier density. As was shown by Luu et al. [10], harmonic distortions can stem from the electrons being accelerated in a conduction band whose dispersion diverts from a parabolic behavior and comprises several harmonic orders. Although an investigation of this parameter regime appears highly interesting, an undistorted sampling of the infrared waveform calls for low field strengths in the drive arm. Therefore, we limit the following discussion to experiments using drive fields on the order of 0.2 V/Å and below.

5.4 Broadband Strong-Field Sampling in the Short-Wavelength-Infrared

In a next step, the SFS traces are directly compared to EOS measurements. Since the latter sample the waveform at the same focus with the same spot sizes and the same absolute timing — only with slightly lower intensities for both arms — we can assume the same test waveform in both measurements. It has to be noted, that there is an ambiguity concerning the sign of recorded EOS trace. The sign of the detected electric field depends on the sign of the $\chi^{(2)}$ tensor that is defined by the exact orientation of the electro-optic crystal. This cannot be unambiguously identified in the experimental setup.

As explained in the previous section, the stability of the interferometric arms with respect to each other is paramount. In order to minimize slow temporal drifts due to the long separate propagation of injection and drive pulse over several meters, the comparison between EOS and SFS has to be conducted for consecutive measurements which are performed as fast as possible. For each waveform, five independent scans are recorded with a time constant of 30 ms, resulting in 500 pulses per data point. The measurement takes about 2 min per waveform.

The comparison of the two sampling techniques is shown in Fig. 5.7. The EOS measurement is corrected by deconvolving the calculated response function, which takes into account the propagation through the EOS crystal as well as the spectral response of filters and photodiodes used in the balanced detection, see Fig. 3.9. The temporal EOS trace is in excellent agreement with the measured current, despite the complicated structure of the test waveform. The spectral response of the directly measured current shows a pronounced red-shift but its second derivative with respect to time agrees well with the spectral intensity of the EOS. This indicates that SFS samples the integral of the vector potential $\alpha(t)$.

In a first attempt, we try to explain the proportionality of the current to $\alpha(t)$ by a simple classical picture: The photoexcited carriers are accelerated according to the Drude model (Eqn. 1.56) which leads to a charge separation. This charge separation gets trapped and induces a current in our external circuit. For the trapping time, we assume 550 fs, which was measured by Martin et al. [156] in the case of crystalline SiO_2. This assumption seems reasonable since similar trapping kinetics for quartz and fused silica have been observed [188, 189].

The injection probability $w(t)$ is given by the instantaneous power deposited in the sample which equals the integrand of Eqn. 1.36. Recent results in attosecond polarization spectroscopy for strong-field excitations in fused silica predict six-photon absorption as the dominant excitation mechanism in our parameter regime [35]:

$$w(t) \propto E_L(t) \frac{\mathrm{d}}{\mathrm{d}t} \chi^{(11)} \left| E_L(t) \right|^{11} \quad . \tag{5.1}$$

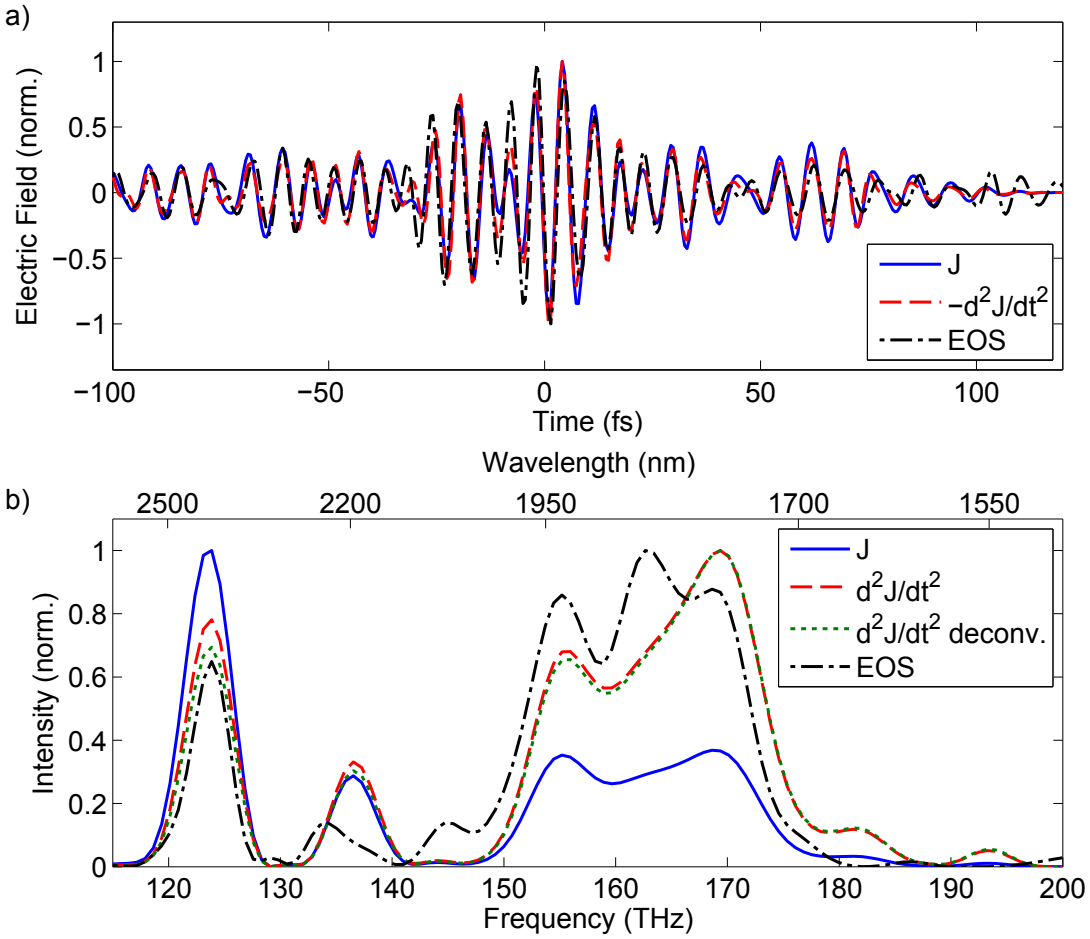

Figure 5.7: Comparison between EOS and SFS. a) Temporal waveforms. In the case of EOS (black dotted-dashed line) a deconvolution with the calculated response function is performed. In the case of SFS, the directly measured current J (blue solid line) and its second derivative respect to time $\mathrm{d}^2J/\,\mathrm{d}t^2$ (red dashed line) are plotted. The latter is flipped horizontally for better comparison. b) Spectral amplitude of the above plotted temporal waveforms. An additional deconvolution of the response function (see Eqn. 5.3) for the SFS signal is shown (green dotted line).

The charge separation of the photoexcited carriers according to the Drude model is governed by Eqn. 1.57 and depends on the relaxation time τ. The measured current $J(\Delta t)$ at each temporal delay Δt between injection and drive pulse is proportional to the integral of the trapped charge separation $x_{tr}(t_0) = x_{t_0}(t = t_{tr})$ weighted with the time-delayed injection probability $w(t_0 - \Delta t)$ over all injections times t_0:

$$J(\Delta t) \propto \int_{-\infty}^{\infty} w(t_0 - \Delta t) \cdot x_{tr}(t_0)\, \mathrm{d}t_0 \ . \tag{5.2}$$

Fig. 5.8 a) shows the injection probability assuming six-photon absorption using the injection pulse characterized by XFROG measurements and assuming no additional CEP offset. In Fig. 5.8 b) three exemplary trajectories for different relaxation times τ are depicted for charge carriers injected at $t_0 = 0$. Fig. 5.8 c) and d) present the simulated results for Eqn. 5.2 in time and frequency space. According to the Drude model, the current follows the vector potential $A(t)$, independent of the relaxation and the trapping time. These results are in agreement with wave propagation simulations based on Eqn. 1.29 that solve Maxwell's equations self-consistently. However, the classical models are in sharped disagreement with the experimental results which means that a quantum mechanical modeling of the current generation is needed.

Fig. 5.9 depicts the solution of the one-dimensional TDSE for a periodic lattice and an atomic potential, performed by Dr. Nicholas Karpowicz. The experiment is mimicked by applying two pulses with a variable time delay Δt to the potential and recording the induced polarization that is left in the material after the pulse is gone. The polarization is calculated by taking the expectation value of the position of the electron wave packet $\langle x \rangle (\Delta t)$. The size of the one-dimensional lattice is 170 nm. There is a striking difference between the atomic and the solid case. Fig. 5.9 d) and f) show that for the lattice potential, the second derivative of the delay-dependent polarization follows the electric field of the drive pulse, just as in the experiment (see Fig. 5.7). The response of the atom however shows a phase shift and a spectral blue shift, which is consistent to the classical result where the induced charge separation follows the vector potential. This distinct behavior can be attributed to the different characteristics of the wave functions and how they adapt to the strong external field. In order to gain a better understanding of this dynamic behavior, further simulations and experiments are needed. Experiments with crystalline samples like α-quartz and BaF_2 are in preparation. From the simulation side, time-dependent density functional theory can give further insight on the microscopic behavior of the current.

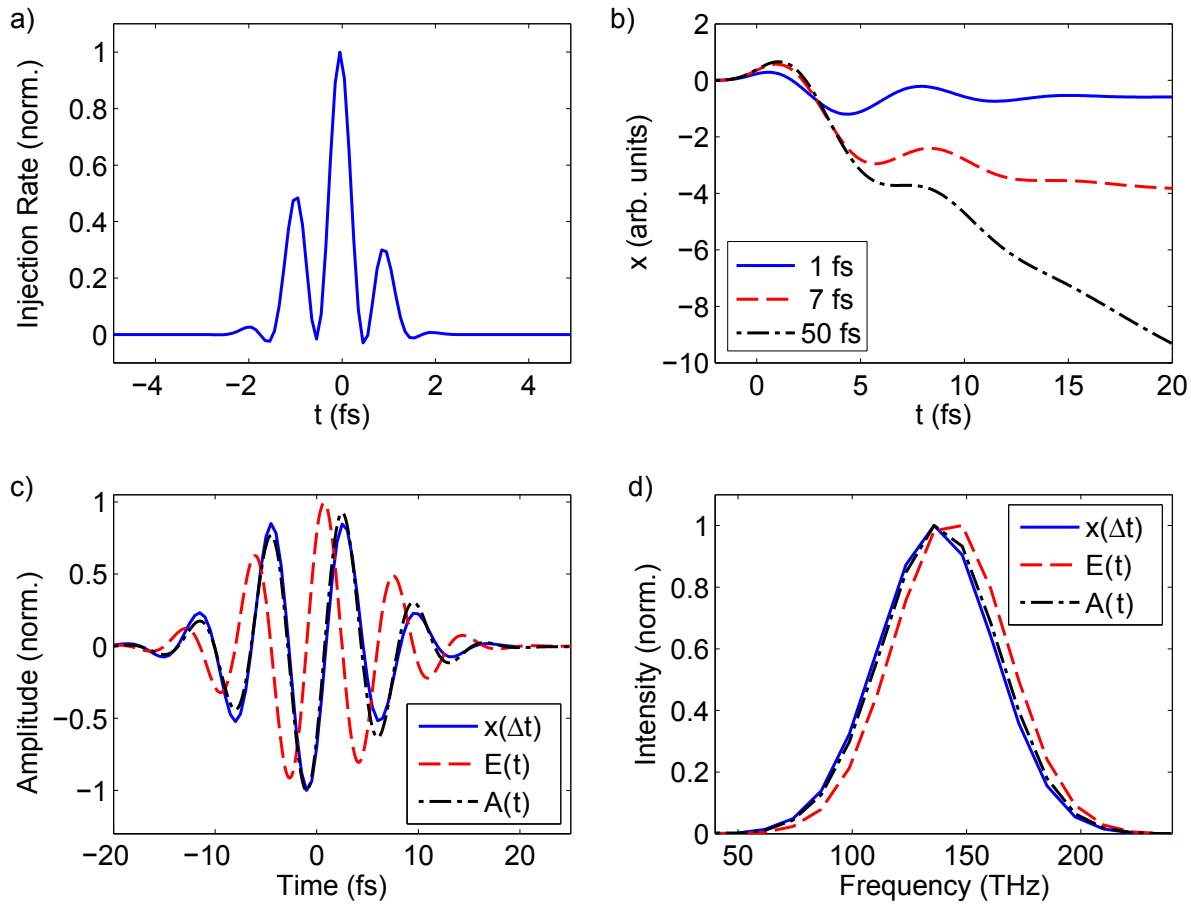

Figure 5.8: Drude Model for Photoexcited Charge Separation. a) Normalized injection probability assuming six-photon absorption by measured injection pulse. b) Trajectories of charge carriers injected at $t = 0$ for different relaxation rates τ. c) Trapped charge separation as a function of delay between injection and drive pulse (blue solid line), compared to the original drive field (red dashed line) and the vector potential (black dotted-dashed line). d) Spectral intensity of the time traces in c).

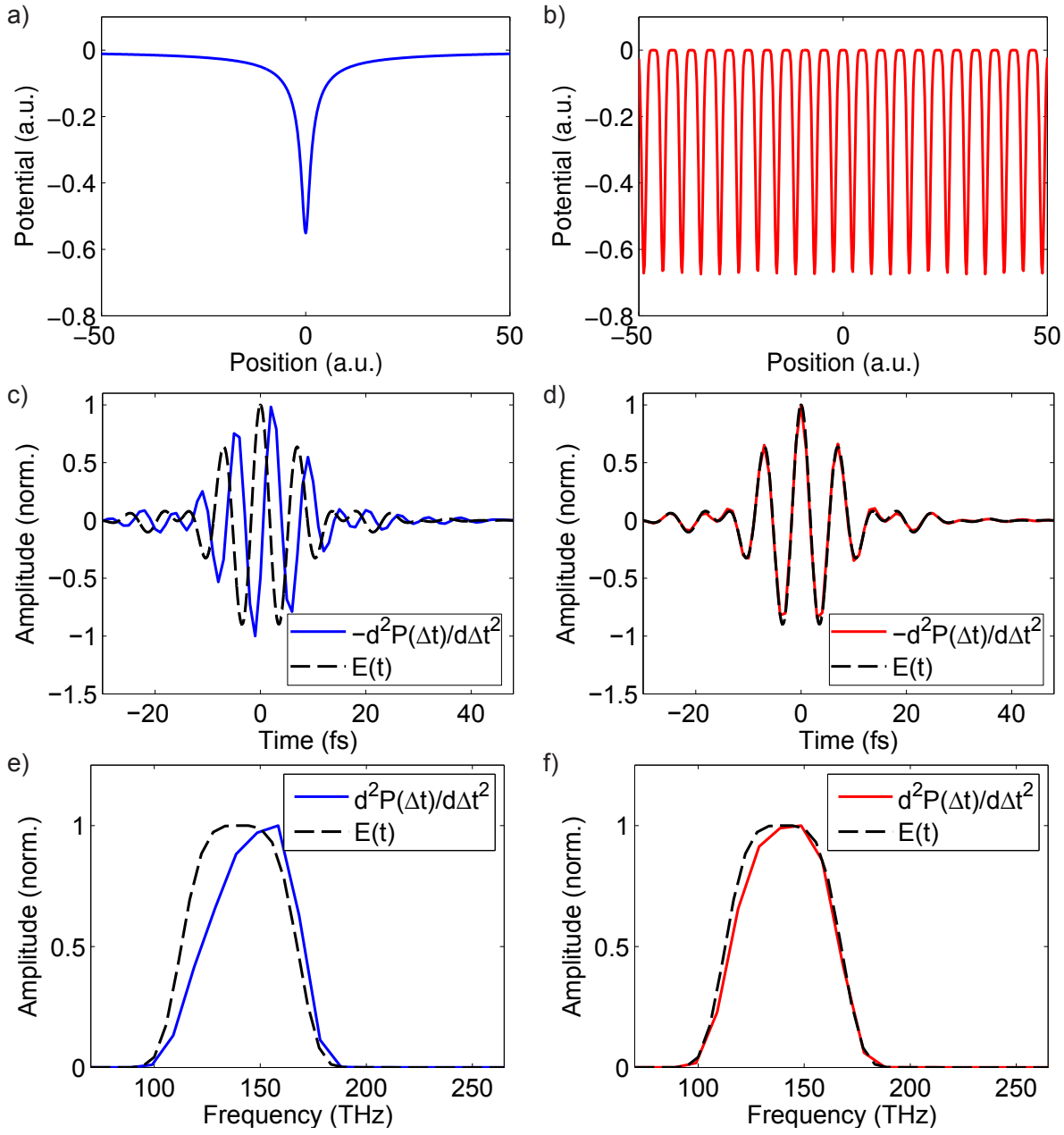

Figure 5.9: TDSE Simulation of SFS. Left column: Atomic case. Right column: Solid case. Top row: Potentials in atomic units. Mid row: Second derivative of the polarization response compared to the electric field of the drive pulse (black dashed line). Bottom row: Spectral amplitude of the above plotted time traces. The second derivative of the polarization in the solid agrees well with the electric field of the drive pulse.

Although the reason for the deviation from the classical behavior cannot be resolved in the course of this work, the experimental results clearly support our claim that ultrafast currents can be used for electric field sampling. Two important figures of merit of optical metrology schemes are the signal-to-background ratio and the dynamic range. In order to compare the signal-to-background ratio of EOS and SFS, a typically recorded signal is compared to a dark scan where the drive arm is blocked. The results are shown in Fig. 5.10. The ratio after averaging over 1500 laser shots per data point is 3.25×10^2 for EOS and 1.41×10^1 for SFS. Keep in mind that the intensity of test waveform sent to the EOS is only 0.6 % of the total intensity used in the SFS setup. Under optimal conditions the signal-to-background in EOS can be orders of magnitude higher. The dynamic range of SFS, which leaves the response of the current undistorted, is on the order of 20 in terms of electric field strength. A brief comparison of the performance of the two presented pulse characterization techniques under the current experimental conditions is given by Table 5.1.

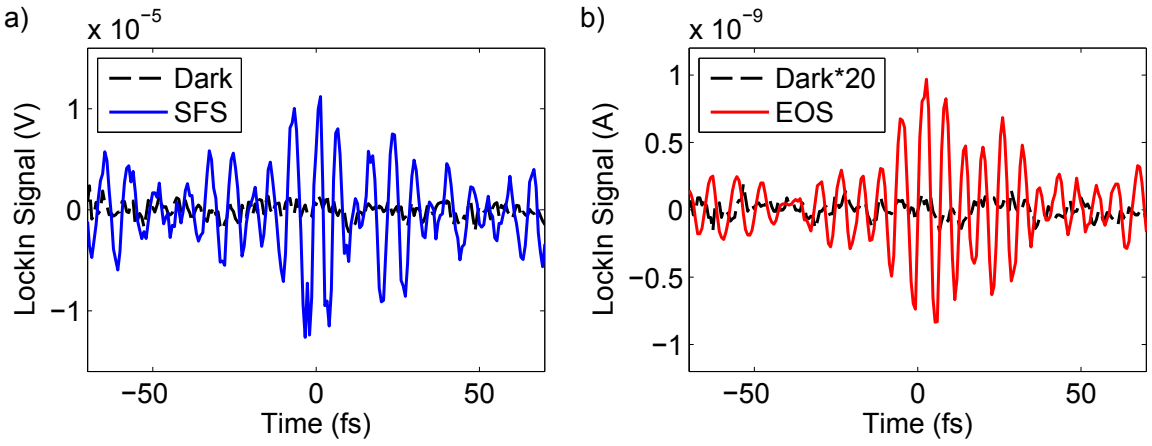

Figure 5.10: Dark Signal Comparison Between EOS and SFS. a) Recorded SFS waveforms. b) Recorded EOS waveforms. For both measurements, 1500 shots are averaged per data point. During the dark measurements (black dashed lines), the SWIR arm is blocked. No bandpass filtering or deconvolution is applied to the raw data.

	EOS	SFS
Proportional to	electric field	integral of vector potential
Gate	sampling pulse	charge carrier injection
Dynamic Range	1×10^5	20
Signal-to-Background	3.25×10^2	1.41×10^1

Table 5.1: EOS versus SFS. Note that the given values for dynamic range and signal-to-background ratio are for the experimental conditions employed in this chapter.

5.5 Spectral Response of Strong-Field Sampling

The last section has demonstrated that the SFS signal follows the integral of the vector potential. This behavior influences the spectral sensitivity of the technique. We discuss the theoretical expression for the spectral response before we turn to potential implementations for confirming it experimentally.

If six-photon absorption is considered as the prominent excitation mechanism at high intensities in SiO_2 as determined in [35], the response of SFS at detection frequency Ω resumes the following form:

$$S(\Omega) \propto \mathcal{F}[E_{inj}(t)^{12}]/\Omega^2 \tag{5.3}$$

The first term reflects the strong temporal confinement of the gate due to the highly nonlinear carrier injection. The $1/\Omega^2$ term stems from the proportionality of the measured current to the second integral of the electric field. Note that in contrast to EOS, no phase-matching condition needs to be met.

The comparison of the SFS with the EOS response function, given by Eqn. 5.3, is visualized in Fig. 5.11. For SFS, $S(\Omega)$ depends on the spectral amplitude and phase of the injection pulse, which is known from XFROG measurements, as well as its CEP. The CEP can in principle be retrieved by one-pulse current scans as demonstrated in [62] but since it depends sensitively on the intensity, the measurement needs to be carefully gauged which is beyond of the scope of this work. Traces for two exemplary CEP choices are plotted in Fig. 5.11 a). Fig. 5.11 b) shows the spectral response without the $1/\Omega^2$-term in order to visualize the broadband response due to the short injection gate and the CEP dependence. The latter is small for most parts of the spectrum but large near the fundamental frequency of the injection pulse. This stems from the fact that the response is composed of the 0th and a 2nd harmonic part of the injection spectrum, which overlap at its fundamental in case the sampling pulse is sufficiently broadband. The CEP determines the relative phase between the DFG and SHG contribution and leads to a significant difference in the response of almost a factor of two. Fig. 5.11 c) shows how the high frequency response is suppressed due to the $1/\Omega^2$ term reflecting the proportionality to the integral of the vector potential.

Despite this roll-off in the response at high frequencies, the sensitivity of SFS should supersede the one of EOS above about 270 THz. In order to investigate this experimentally, an optimization of the experimental setup is needed. In principle, SFS at near-infrared to visible frequencies can be investigated by broadening the infrared drive spectrum by SPM or by generating phase-matched harmonics in a SHG or THG crystal, see Subsection 1.2.1. However, the long arms of the two-color interferometer make this approach unfeasible in the existing setup. The temporal jitter between injection and drive pulse equals the half-cycle duration of the second harmonic spectral components around 900 nm, see Section 2.3. Furthermore, the restrictions in terms of dynamic range and the difficulty to suppress the broadband infrared part of the spectrum with conventional filters call for a high conversion efficiency to the NIR to visible frequencies. Since the drive field cannot exceed 0.2 V/Å to avoid distortions and the interferometric instabilities do not allow for temporal stretching

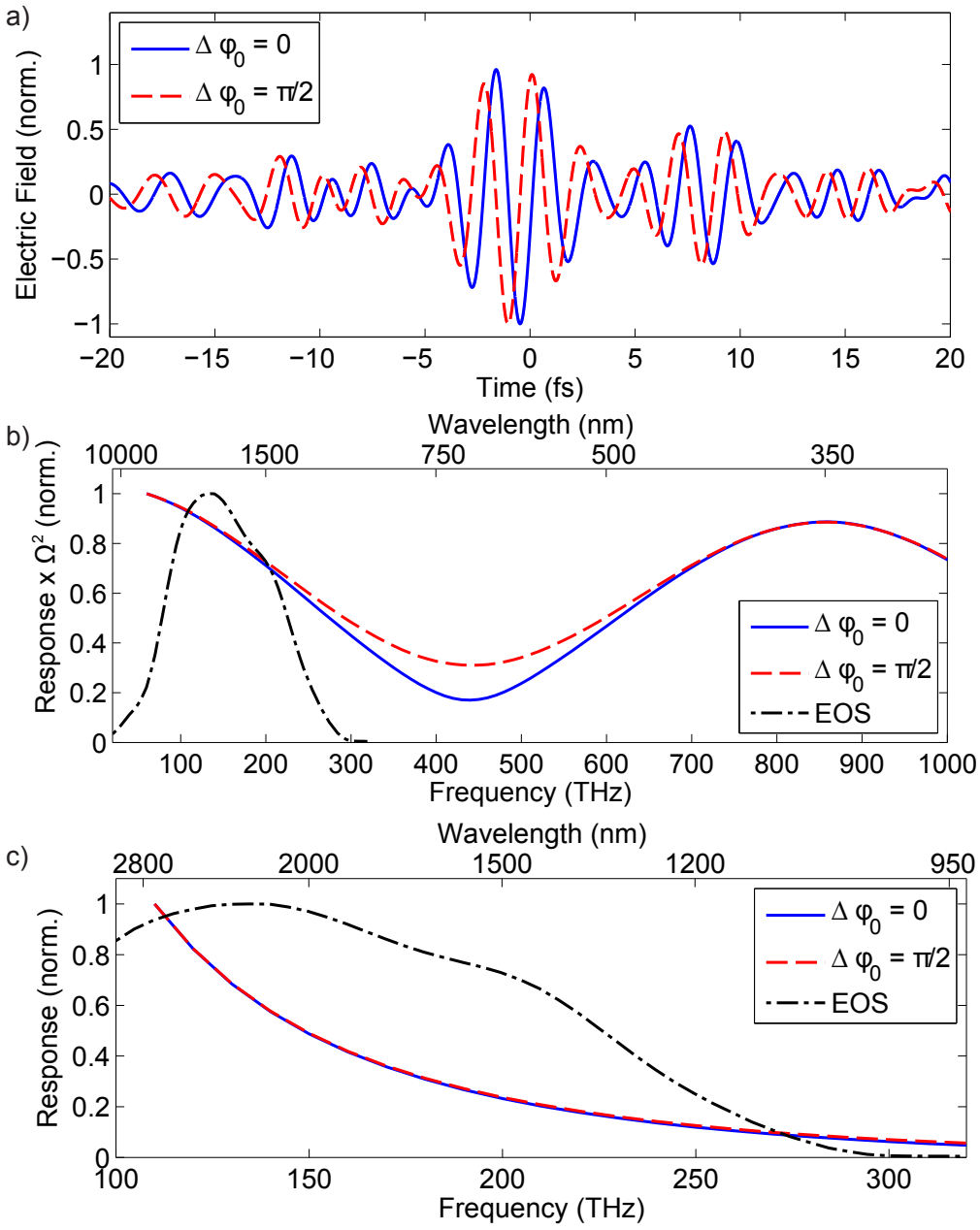

Figure 5.11: Spectral Response of SFS. a) Temporal electric field of the white-light pulse used for injection, with two different CEP offsets $\Delta\varphi_0$. b) Spectral response assuming six-photon absorption as injection mechanism and direct drive field proportionality, compared to EOS response. b) Spectral response assuming six-photon absorption as injection mechanism and proportionality to the integral of the vector potential of the drive field, compared to EOS response.

of the waveform, which would result in longer scanning times, the total usable power for nonlinear conversion is limited.

The temporal instabilities and the restrictions in dynamic range hinder the sampling of frequencies above the fundamental infrared spectrum in the current experimental configuration. However, there are several options to investigate the spectral cutoff and the validity of Eqn. 5.3:

- The two-color interferometer can be shortened by recombining the two arms after the first instead of after the second amplification stage of the OPCPA (see Fig. 2.3). With 10 µJ, the available energy of the drive pulse is sufficient without a further amplification step. However, this change solely eliminates the problems due to the interferometric instabilities.

- In order to reduce temporal jitter and enhance the conversion efficiency, a hollow-core fiber setup can be employed after the third OPCPA stage. As shown by Schwarz [38], focusing the SWIR pulse in an argon-filled HCF, a broadband and spectrally flat spectrum ranging down to 400 nm is generated. This broadband spectrum is the basis of the infrared light field synthesizer which is currently under development in our group (see Appendix A). The high-frequency channel compressed with customized chirped mirrors is planned to inject the charge carriers and sample the waveform comprising the remaining spectrum. The stability of this interferometer is only defined by the number and angle of reflections in the chirped mirror compressor.

- In the original two-pulse current experiments [4], a compact white-light interferometer was used to observe oscillation frequencies corresponding to 760 nm. A careful restriction of the drive field in order to maintain the linear scaling of the overall signal should allow an equivalent detection of the drive waveform as presented above. Since both injection and drive spectrum are equivalent, a strong dependence of the response on the CEP of the injection pulse is expected, see Fig. 5.11 b). Detecting this CEP dependence can serve as a first step towards validating Eqn. 5.3. Additionally, including a SHG crystal in the white-light drive arm can provide frequencies up to the ultraviolet and test the SFS response in the petahertz frequency range.

- An alternative approach to testing Eqn. 5.3 is making the injection gate longer and thus pushing the cutoff frequency to longer wavelengths. In the presented setup, the role of injection and drive pulse can simply be switched by rotating the sample by 90° and adjusting the intensities accordingly. Using the SWIR pulse for injection, the time frame for the excitation from the valence to the conduction band is about three times longer than in the case of visible light injection. A comparison between the Fourier transform of the measured current trace with the spectrum of the drive pulse especially in terms of a cutoff or roll-off can help to identify the temporal confinement of the injection.

5.6 Outlook

Using the EOS setup introduced in Chapter 3, we have demonstrated that optical-field-induced currents scale linearly with the drive field and follow the integral of its vector potential for drive field strengths below 0.2 V/Å. Above this value, drive-field-assisted carrier excitation is observed which leads to a distortion of the recorded trace. For lower waveform intensities however, the ultrafast two-pulse current generation can be employed as a compact characterization technique for phase-stable pulses. The fact that the current measurement reproduces the integral of the vector potential cannot be explained with classical models but requires a quantum mechanical treatment.

Analyzing the spectral response function of the SFS technique has shown the potential to extend the spectral cutoff until the visible to ultraviolet range. Despite its broad bandwidth, the second interesting feature of the spectral sensitivity is a strong CEP dependence at frequencies which correspond to the fundamental of the injection field strength. Options for verifying this behavior experimentally were summed up at the end of the previous section.

The broad expected bandwidth due to the high nonlinearity of the injection process is in contrast to EOS, whose spectral response has a strict limit, when the bandwidth of the sampling pulse meets the test frequency. The limit can within certain boundaries be tailored by applying post-spectral filtering but ultimately depends on the duration of the fundamental sampling pulse. This behavior impedes the extension of EOS to wavelengths below the 1.27 µm cutoff, demonstrated in Section 3.4. Therefore, despite its lower dynamic range and signal-to-background, SFS shows great potential for future applications in the characterization of phase-stable waveforms from conventional Ti:Sa sources, as well as broadband OPCPAs, and light-field synthesizers. The compactness of the setup makes SFS an attractive alternative to attosecond streaking for waveform characterization, especially for studying strong-field dynamics in solids in ambient conditions. Among other applications, the experimental implementation of attosecond polarization spectroscopy [35] could be greatly simplified.

The presented results use fused silica as a sample material due to its easy experimental handling and its previous successful applications in ultrafast current generation [4, 62] and other strong-field experiments investigated in our group [1, 10, 35]. Although the capabilities of SFS as a pulse characterization technique have been demonstrated, our understanding of the underlying processes is still in its infancy. The use of other dielectric materials with a more defined crystalline structure could allow for more accurate modeling and give insight in the universality of the sampling process. Future experimental studies using crystalline SiO_2 and BaF_2 samples are already in preparation.

Chapter 6

Conclusion

Strong-field experiments in solids have recently granted access to a novel regime of light-matter interaction. In the strong-field regime, the response of an optically excited system follows the electric field rather than the envelope of the pulse [1]. Light sources which provide phase-stable waveforms together with metrology schemes, which are able to characterize them, are essential tools for studying this response. While phase-stable waveforms derived from Ti:Sa lasers or optical parametric amplifiers are routinely available, obtaining complete information on their electric field oscillations is challenging. So far, the field-resolved characterization of waveforms has only been obtainable with the help of isolated attosecond pulses from Ti:Sa-based sources [16, 116] or limited to the terahertz to mid-infrared regime [3, 12]. In the wavelength range of a few micrometers, a complete field characterization technique has to date been missing.

This dissertation introduces two measurement schemes for the full electric field characterization of near- to short-wavelength-infrared pulses. Both techniques have been demonstrated using a phase-stable optical parametric amplifier with a central wavelength of 2.1 µm.

The first measurement scheme is an extension of electro-optic sampling to a cutoff frequency of 235 THz. This near-doubling of the previously demonstrated frequency limit [12] is enabled by using a short 5 fs sampling pulse, broadband phase matching in BBO, and post-spectral filtering to extract the high frequency components of the sampling spectrum. The filter reshapes the spectral response function and enhances the sensitivity for higher frequencies compared to the unfiltered case. These improvements facilitate the complete characterization of a broadband waveform generated by the optical parametric amplifier and its compression using a programmable dispersive filter. For the first time, the waveform evolution during the parametric amplification process is observed, revealing a pronounced pump-dependent phase shift.

The extended application range of electro-optic sampling makes it a useful tool for optical parametric amplifiers in the near to mid-infrared region as well as for erbium-based laser systems and their frequent applications in telecommunications and remote sensing. The discussion of the response function shows that there is no fundamental limit to further extending the cutoff frequencies above 300 THz. If the broad phase-matching bandwidth of

BBO as an electro-optic crystal is combined with a sampling pulse comprising wavelength components down to the ultraviolet, a sampling of optical cycles in the Ti:Sa spectral range is feasible.

A metrology technique which has the potential to resolve frequencies even to the visible spectral range is strong-field solid-state sampling. This novel sampling scheme is based on optical-field-induced currents in dielectric materials [4]. The ultrafast injection of charge carriers into the conduction band serves as a gate in the sampling, similar to the high-harmonic-generation process in gases which is used as a gate for the petahertz optical oscilloscope [116]. In the presented experimental implementation, a few-cycle white-light pulse is used for the injection while an infrared waveform derived from the optical parametric amplifier acts as the temporally delayed drive pulse.

For drive field strengths below $0.2\,\mathrm{V/Å}$, the signal scales linearly with the field amplitude. Higher field strengths however, lead to drive-field-assisted carrier injection and a distortion of the recorded trace in time and frequency domain. In the linear regime, the two-pulse current can be used to resolve the electric field oscillations of the drive waveform. This is demonstrated by comparing the current to an electro-optic sampling measurement. The spectral response agrees with the integral of the vector potential. A classical description assuming the Drude model for carrier transport cannot reproduce this behavior. Solving the one-dimensional time-dependent Schrödinger equation shows that the periodic band structure of the lattice leads to a spectral and temporal shift of the induced polarization in comparison with an atomic system. The atomic response follows the vector potential while the polarization in the solid agrees with its integral, reproducing the experimental results. Further studies using different materials for the current generation and more accurate models taking into account the band structure as well as electron-electron interactions are needed to verify the universality of the accomplished results.

In order to gain a deeper understanding of the generation and detection of optical-field-induced currents, this work has systematically studied the influence of the sample geometry and material on the measured signal. By the implementation of a simple one-pulse-scheme, the confinement of the generated current to the first $20\,\mu\mathrm{m}$ from the surface of the material is demonstrated. An enhancement of the current signal close to the electrodes, which has been observed for low-order nonlinear current control experiments [95], is reproduced. Furthermore, the experiments demonstrate a non-trivial scaling with respect to the applied field strength, which deviates from the expected steep scaling associated with multi-photon absorption or tunneling. In order to investigate the current generation process in more detail, the combination with other metrology techniques like time-resolved terahertz spectroscopy [46], field-induced second harmonic generation [182], and solid-state high harmonic spectroscopy [10] are recommended for future studies.

The measurement techniques presented in this work have distinct advantages and limitations: The well-established electro-optic sampling features high sensitivity and a large dynamic range while the frequency cutoff depends on the duration of the gate pulse. Strong-field solid-state sampling on the other hand employs a nonlinearly generated, ultrashort gate, which potentially allows to extend the spectral cutoff into the visible and ultraviolet region. However, its dynamic range is limited and several aspects of the current genera-

tion and detection require further investigation. Both techniques have a compact footprint and work under ambient conditions, which makes them a valuable add-on to existing experimental setups using phase-stable light sources in the mid- to near-infrared spectral regime.

The study and control of strong-field-driven electrons in solids is still in the fledgling stages. Metrology schemes, which are able to unambiguously resolve the driving waveforms as well as the electronic response of excited system, can help to advance the understanding of the underlying dynamic processes. They enable the study of dynamics which have so far been unobservable in solids due to their short time scales, like ultrashort dephasing of excited carriers [59] or the onset of effective mass [190]. The insight that the characterization tools presented in this dissertation provide into carrier dynamics on the time scale of light waves, represents a new step towards petahertz opto-electronics [2].

Appendix A

Short-Wavelength-Infrared Beamline

Although this work primarily utilizes the strong SWIR fields for experiments in solids (see Chapter 5) which can be performed in ambient air, it also lays the foundation for future experiments in vacuum. A vacuum beamline dedicated to experiments with few-cycle SWIR pulses has been designed and implemented over the course of this dissertation. One experiment requiring high vacuum conditions is HHG (see Subsection 1.2.2) in the soft x-ray regime with long-wavelength drivers and their temporal characterization using attosecond streaking, which was introduced in Subsection 2.1.3.

The cutoff energy E_c of the HHG photons is given by [104]

$$E_c = 3.17U_p + I_p \propto \frac{1}{\omega^2} \ . \tag{A.1}$$

Since the cutoff energy scales quadratically with increasing wavelength, there has been considerable effort towards achieving HHG with long wavelength drivers. This is a challenging task because of the unfavorable scaling of the photon flux with wavelength, which has been theoretically determined in the case of a one-electron emitter as λ^{-5} to λ^{-6} [191]. However when considering a real gas target with multiple electrons involved, phase-matching conditions play an important role and can help to enhance the HHG yield [64]. The generation of high energetic photons has been demonstrated in the multi 100 eV to few keV range [101, 192].

The soft x-ray spectral region is extremely relevant for spectroscopic applications, for biological samples as well as in the solid state. Therefore, the application of the SWIR source to HHG is highly desirable. Additionally, the strong-field experiments will benefit from the vacuum beamline because pulse distortions from plasma generation in air, which can occur in the focus of a beam with high pulse energy, are avoided. A vacuum environment is furthermore necessary for studies at low sample temperatures.

The design is loosely based on an existing Ti:Sa beamline [193] and consists of five chambers: the synthesizer, the HHG, the delay, the streaking, and the experimental chamber. Except for the HHG chamber, which is already in use and equipped with all necessary diagnostics, the other chambers have not been commissioned yet.

The pulses derived from the phase-stable SWIR source are broadened in a gas-filled HCF, as already demonstrated in [38], and sent to the synthesizer chamber where they

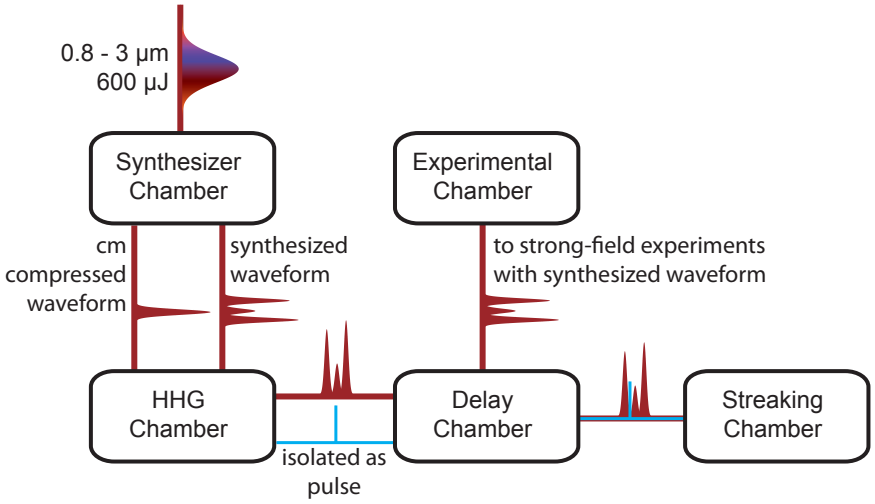

Figure A.1: Short-Wavelength-Infrared Vacuum Beamline, Optional Mode of Operation. In the synthesizer chamber, part of the broadband continuum generated from the SWIR source will be sculpted into an arbitrary waveform. The other part of the beam can be compressed to a few-cycle pulse by a chirped mirror compressor. This pulse can generate the isolated attosecond pulse, which is overlapped and temporally delay with respect to the synthesized waveform. The waveform can then be temporally characterized in the streaking chamber and used to investigate strong-field processes in the experimental chamber.

are split in two paths. Half of the beam is temporally shaped in an infrared synthesizer currently under development. Controlling the dispersion in separate spectral arms and recombining them with an adjustable delay can be used to generate sub-cycle pulses or arbitrary waveforms which can be characterized in the streaking chamber. This concept has already been successfully demonstrated with a NIR drive [111]. Since not every waveform is suitable for HHG, the second part of the beam is not sent through the synthesizer but a chirped mirror compressor instead. Its bandwidth is limited to about one optical octave by the dielectric optics but it still support two-cycle pulses which can used as reliable drivers for HHG. The delay between the two arms can be adjusted by a piezo stage. If only one arm is used, the HHG and infrared can be split and recombined by perforated mirrors and overlapped in the streaking chamber using a Mach-Zehnder type interferometric approach [194, 195] with short arms in order to insure stability. The advantage over using a double mirror for adjusting the relative delay in a collinear fashion is that the focusing of each arm can be adjusted independently to ensure a nice mode in the focus. The characterization of XUV/soft x-ray pulses generated by a SWIR or MIR source by streaking has — to the best knowledge of the author — not been demonstrated yet. Once the synthesized SWIR field is characterized, it can be used for strong-field solid experiments in the experimental chamber.

Optionally, a gas target for vacuum ultra-violet (VUV) generation can be inserted in the synthesized beam. This makes the beamline design flexible to accommodate various modes

of operation, using SWIR, XUV, VUV in different combinations to temporally investigate strong-field tunneling as well as resonant core-state, and valence-band excitations. One exemplary mode of operation using a characterized waveform for strong-field experiments is schematically depicted in Fig. A.1. Fig. A.2 shows a photograph of the actual setup in the attosecond laboratory. A detailed graph with an overview of all optional beam paths in the beamline is given in Fig. A.3.

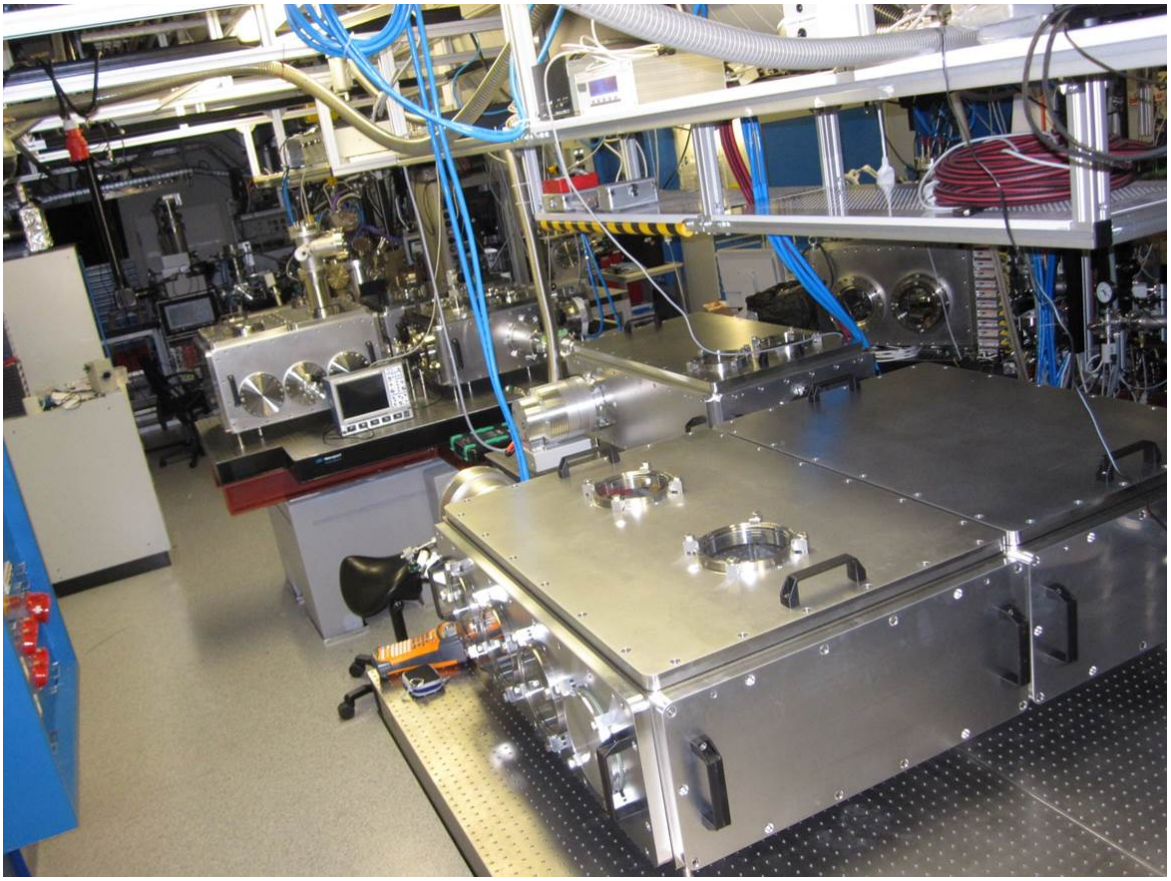

Figure A.2: Photograph of Beamline in Attosecond Lab.

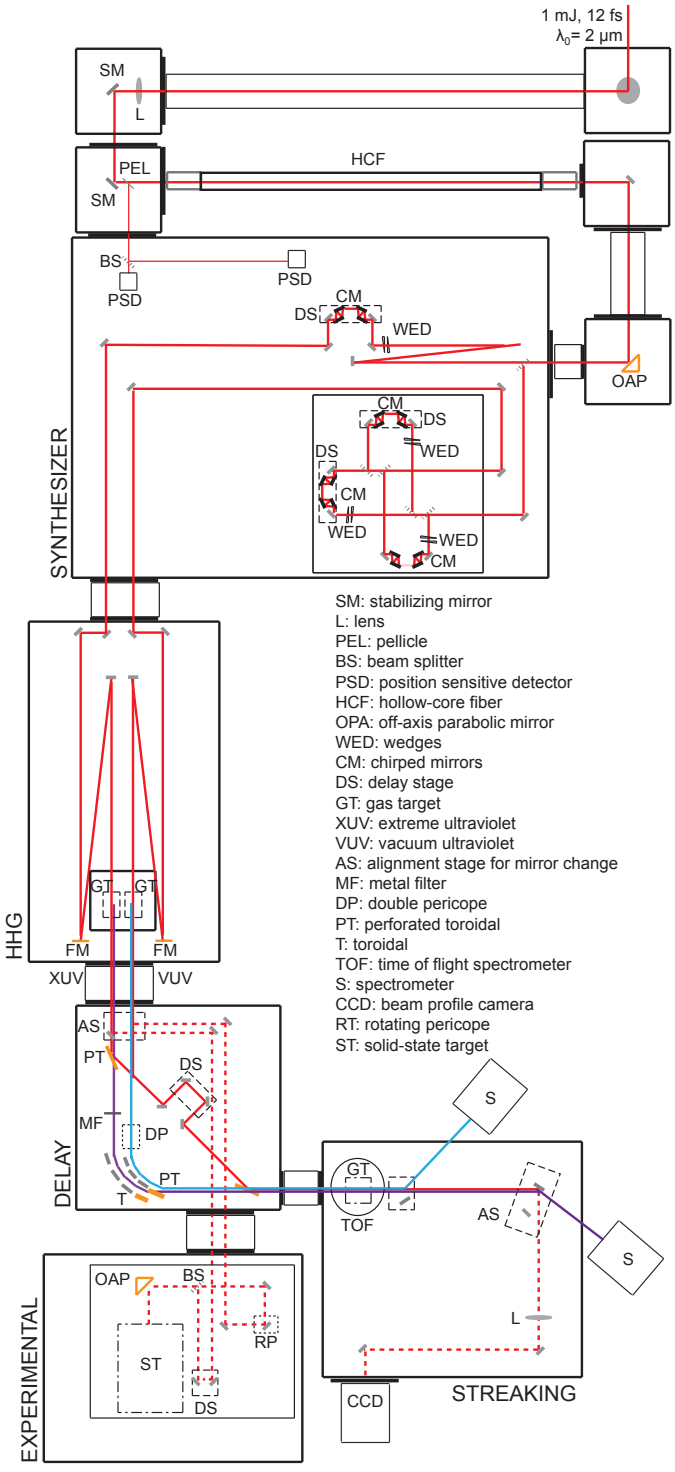

Figure A.3: Detailed Beam Path Short-Wavelength-Infrared Vacuum Beamline. The dashed lines correspond to the beam path at the alternative alignment stage (AS) position. The relative size of the chambers is to scale.

Appendix B

Data Archiving

The experimental raw data, evaluation files, and original figures can be found on the Data Archive Server of the Laboratory for Attosecond Physics at the Max Planck Institute of Quantum Optics: `//AFS/ipp-garching.mpg.de/mpq/lap/publication_archive`

For each figure, there is a dedicated folder containing the raw data, Matlab scripts for the data analysis or simulations, and the figure in .pdf, .png or .jpg format as well as a readme file for further explanations and instructions. An overview of the figures and how they are produced is given in the following table.

Fig. 1.1	schematic sketch (.pdf)
Fig. 1.2	schematic sketch (.pdf)
Fig. 1.3	schematic sketch (.pdf)
Fig. 1.4	schematic sketch (.pdf)
Fig. 1.5	schematic sketch (.pdf)
Fig. 1.6	schematic sketch (.pdf)
Fig. 1.7	reprint Springer
Fig. 1.8	schematic sketch (.pdf)
Fig. 1.9	plot (.pdf), analysis script (.m), original data
Fig. 1.10	reprint Nature
Fig. 1.11	reprint Physical Review Letters
Fig. 1.12	reprint Physical Review Letters
Fig. 2.1	plot (.pdf), analysis script (.m), original data
Fig. 2.2	schematic sketch (.pdf)
Fig. 2.3	schematic sketch (.pdf)
Fig. 2.4	plot (.pdf), analysis script (.m), original data
Fig. 2.5	schematic sketch (.pdf)
Fig. 2.6	plot (.pdf), analysis script (.m), original data
Fig. 2.7	plot (.pdf), analysis script (.m), original data
Fig. 2.8	plot (.pdf), analysis script (.m), original data
Fig. 3.1	schematic sketch (.pdf)
Fig. 3.2	plot (.pdf), analysis script (.m), original data

Fig. 3.3	plot (.pdf), analysis script (.m), original data
Fig. 3.4	plot (.pdf), analysis script (.m), original data
Fig. 3.5	plot (.pdf), analysis script (.m), original data
Fig. 3.6	plot (.pdf), analysis script (.m), original data
Fig. 3.7	plot (.pdf), analysis script (.m), original data
Fig. 3.8	plot (.pdf), analysis script (.m), original data
Fig. 3.9	plot (.pdf), analysis script (.m), original data
Fig. 4.1	schematic sketch (.pdf)
Fig. 4.2	schematic sketch (.pdf)
Fig. 4.3	schematic sketch (.pdf)
Fig. 4.4	schematic sketch (.pdf)
Fig. 4.5	plot (.pdf), analysis script (.m), original data
Fig. 4.6	labeled photograph (.jpg)
Fig. 4.7	plot (.pdf), analysis script (.m), original data
Fig. 4.8	schematic sketch (.pdf)
Fig. 4.9	plot (.pdf), analysis script (.m), original data
Fig. 4.10	plot (.pdf), analysis script (.m), original data
Fig. 4.11	plot (.pdf), code description
Fig. 4.12	plot (.pdf), analysis script (.m), original data
Fig. 4.13	plot (.pdf), analysis script (.m), original data
Fig. 4.14	plot (.pdf), simulation script (.m)
Fig. 5.1	schematic sketch (.pdf)
Fig. 5.2	plot (.pdf), analysis script (.m), original data
Fig. 5.3	schematic sketch (.pdf)
Fig. 5.4	plot (.pdf), analysis script (.m), original data
Fig. 5.5	plot (.pdf), simulation script (.m)
Fig. 5.6	plot (.pdf), analysis script (.m), original data
Fig. 5.7	plot (.pdf), analysis script (.m), original data
Fig. 5.8	plot (.pdf), simulation script (.m)
Fig. 5.9	plot (.pdf), simulation script (.m)
Fig. 5.10	plot (.pdf), analysis script (.m), original data
Fig. 5.11	plot (.pdf), simulation script (.m)
Fig. A1	schematic sketch (.pdf)
Fig. A2	photograph (.jpg)
Fig. A3	schematic sketch (.pdf)

Bibliography

[1] M. Schultze, E. M. Bothschafter, A. Sommer, et al. *Controlling dielectrics with the electric field of light.* Nature, 493 (7430), 75–78 (2013).

[2] F. Krausz and M. I. Stockman. *Attosecond metrology: from electron capture to future signal processing.* Nature Photonics, 8 (3), 205–213 (2014).

[3] Q. Wu and X.-C. Zhang. *Free-space electro-optic sampling of terahertz beams.* Applied Physics Letters, 67 (24), 3523–3525 (1995).

[4] A. Schiffrin, T. Paasch-Colberg, N. Karpowicz, et al. *Optical-field-induced current in dielectrics.* Nature, 493 (7430), 70–74 (2013).

[5] P. B. Corkum and F. Krausz. *Attosecond science.* Nature Physics, 3 (6), 381–387 (2007).

[6] T. Brabec and F. Krausz. *Intense few-cycle laser fields: Frontiers of nonlinear optics.* Reviews of Modern Physics, 72 (2), 545–591 (2000).

[7] M. Lenzner, J. Krüger, S. Sartania, et al. *Femtosecond optical breakdown in dielectrics.* Physical Review Letters, 80 (18), 4076–4079 (1998).

[8] S. Ghimire, A. D. DiChiara, E. Sistrunk, et al. *Observation of high-order harmonic generation in a bulk crystal.* Nature Physics, 7 (2), 138–141 (2011).

[9] O. Schubert, M. Hohenleutner, F. Langer, et al. *Sub-cycle control of terahertz high-harmonic generation by dynamical Bloch oscillations.* Nature Photonics, 8 (2), 119–123 (2014).

[10] T. T. Luu, M. Garg, S. Y. Kruchinin, et al. *Extreme ultraviolet high-harmonic spectroscopy of solids.* Nature, 521 (7553), 498–502 (2015).

[11] A. Weiner. *Ultrafast Optics.* Wiley, Hoboken, N.J, 1 edition edition (2009).

[12] A. Sell, R. Scheu, A. Leitenstorfer, et al. *Field-resolved detection of phase-locked infrared transients from a compact Er:fiber system tunable between 55 and 107 THz.* Applied Physics Letters, 93 (25), 251107 (2008).

[13] G. Cerullo and S. De Silvestri. *Ultrafast optical parametric amplifiers.* Review of Scientific Instruments, 74 (1), 1–18 (2003).

[14] C. Vozzi, M. Negro, and S. Stagira. *Strong-field phenomena driven by mid-infrared ultrafast sources.* Journal of Modern Optics, 59 (15), 1283–1302 (2012).

[15] H. Fattahi, H. G. Barros, M. Gorjan, et al. *Third-generation femtosecond technology.* Optica, 1 (1), 45–63 (2014).

[16] R. Kienberger, E. Goulielmakis, M. Uiberacker, et al. *Atomic transient recorder.* Nature, 427 (6977), 817–821 (2004).

[17] J. D. Jackson. *Klassische Elektrodynamik.* Walter de Gruyter (2002).

[18] J.-C. Diels and W. Rudolph. *Ultrashort Laser Pulse Phenomena, Second Edition.* Academic Press, Amsterdam ; Boston, 2 edition edition (2006).

[19] M. Wollenhaupt, A. Assion, and T. Baumert. *Short and ultrashort laser pulses.* In F. Träger (Editor), *Springer Handbook of Lasers and Optics*, pp. 1047–1094. Springer Berlin Heidelberg (2012).

[20] R. Trebino. *Frequency-Resolved Optical Gating: The Measurement of Ultrashort Laser Pulses.* Springer Science & Business Media (2000).

[21] H. R. Telle, G. Steinmeyer, A. E. Dunlop, et al. *Carrier-envelope offset phase control: A novel concept for absolute optical frequency measurement and ultrashort pulse generation.* Applied Physics B, 69 (4), 327–332 (1999).

[22] A. E. Siegman. *Lasers.* University Science Books (1986).

[23] A. M. Fox. *Optical Properties of Solids.* Oxford University Press (2001).

[24] Sellmeier, Wolfgang von. *Zur Erklärung der abnormen Farbenfolge im Spectrum einiger Substanzen.* Annalen der Physik, 219 (6), 272–282 (1871).

[25] R. L. Fork, O. E. Martinez, and J. P. Gordon. *Negative dispersion using pairs of prisms.* Optics Letters, 9 (5), 150–152 (1984).

[26] E. Treacy. *Optical pulse compression with diffraction gratings.* IEEE Journal of Quantum Electronics, 5 (9), 454–458 (1969).

[27] R. Szipöcs, C. Spielmann, F. Krausz, et al. *Chirped multilayer coatings for broadband dispersion control in femtosecond lasers.* Optics Letters, 19 (3), 201–203 (1994).

[28] M. M. Wefers and K. A. Nelson. *Generation of high-fidelity programmable ultrafast optical waveforms.* Optics Letters, 20 (9), 1047–1049 (1995).

[29] F. Verluise, V. Laude, Z. Cheng, et al. *Amplitude and phase control of ultrashort pulses by use of an acousto-optic programmable dispersive filter: pulse compression and shaping.* Optics Letters, 25 (8), 575–577 (2000).

[30] T. Brabec and F. Krausz. *Nonlinear optical pulse propagation in the single-cycle regime.* Physical Review Letters, 78 (17), 3282–3285 (1997).

[31] R. W. Boyd. *Nonlinear Optics.* Academic Press, Amsterdam ; Boston, 3rd revised edition. edition (2008).

[32] M. Wegener. *Extreme Nonlinear Optics: An Introduction.* Springer Science & Business Media (2006).

[33] V. S. Yakovlev, S. Y. Kruchinin, T. Paasch-Colberg, et al. *Ultrafast control of strong-field electron dynamics in solids.* In M. Kitzler and S. Gräfe (Editors), *Ultrafast Dynamics Driven by Intense Light Pulses*, number 86 in Springer Series on Atomic, Optical, and Plasma Physics, pp. 295–315. Springer International Publishing (2016).

[34] P. Gaal, W. Kuehn, K. Reimann, et al. *Carrier-wave Rabi flopping on radiatively coupled shallow donor transitions in n-type GaAs.* Physical Review B, 77 (23), 235204 (2008).

[35] A. Sommer, E. M. Bothschafter, S. A. Sato, et al. *Attosecond nonlinear polarization and light-matter energy transfer in solids.* Nature, advance online publication (2016).

[36] A. Nahata, A. S. Weling, and T. F. Heinz. *A wideband coherent terahertz spectroscopy system using optical rectification and electro-optic sampling.* Applied Physics Letters, 69 (16), 2321–2323 (1996).

[37] K.-L. Yeh, M. C. Hoffmann, J. Hebling, et al. *Generation of 10* µj *ultrashort terahertz pulses by optical rectification.* Applied Physics Letters, 90 (17), 171121 (2007).

[38] A. Schwarz. *Few-cycle phase-stable infrared OPCPA.* Ph.D. thesis, Ludwig-Maximilians-Universität München (2014).

[39] R. W. Hellwarth. *Third-order optical susceptibilities of liquids and solids.* Progress in Quantum Electronics, 5, 1–68 (1977).

[40] A. L. Cavalieri, E. Goulielmakis, B. Horvath, et al. *Intense 1.5-cycle near infrared laser waveforms and their use for the generation of ultra-broadband soft-x-ray harmonic continua.* New Journal of Physics, 9 (7), 242 (2007).

[41] L. V. Keldysh. *Ionization in the field of a strong electromagnetic wave.* Soviet Physics JETP, 20 (5), 1307–1314 (1965).

[42] C. Zener. *A theory of the electrical breakdown of solid dielectrics.* Proceedings of the Royal Society of London. Series A, 145 (855), 523–529 (1934).

[43] E. O. Kane. *Zener tunneling in semiconductors.* Journal of Physics and Chemistry of Solids, 12 (2), 181–188 (1960).

[44] N. W. Ashcroft and D. N. Mermin. *Festkörperphysik.* De Gruyter Oldenbourg, 4 edition (2013).

[45] H. Ibach. *Festkörperphysik: Einführung in die Grundlagen.* Springer, 7. Aufl. 2009 edition (2008).

[46] J. Shah. *Ultrafast Spectroscopy of Semiconductors and Semiconductor Nanostructures*, volume 115 of *Springer Series in Solid-State Sciences.* Springer Berlin Heidelberg, Berlin, Heidelberg (1999).

[47] R. Ulbricht, E. Hendry, J. Shan, et al. *Carrier dynamics in semiconductors studied with time-resolved terahertz spectroscopy.* Reviews of Modern Physics, 83 (2), 543–586 (2011).

[48] F. Bloch. *über die Quantenmechanik der Elektronen in Kristallgittern.* Zeitschrift für Physik, 52 (7-8), 555–600 (1929).

[49] J. Feldmann, K. Leo, J. Shah, et al. *Optical investigation of Bloch oscillations in a semiconductor superlattice.* Physical Review B, 46 (11), 7252–7255 (1992).

[50] C. Waschke, H. G. Roskos, R. Schwedler, et al. *Coherent submillimeter-wave emission from Bloch oscillations in a semiconductor superlattice.* Physical Review Letters, 70 (21), 3319–3322 (1993).

[51] P. Leisching, P. Haring Bolivar, W. Beck, et al. *Bloch oscillations of excitonic wave packets in semiconductor superlattices.* Physical Review B, 50 (19), 14389–14404 (1994).

[52] O. Morsch, J. H. Müller, M. Cristiani, et al. *Bloch oscillations and mean-field effects of Bose-Einstein condensates in 1D optical lattices.* Physical Review Letters, 87 (14), 140402 (2001).

[53] J. Delahaye, J. Hassel, R. Lindell, et al. *Low-noise current amplifier based on mesoscopic josephson junction.* Science, 299 (5609), 1045–1048 (2003).

[54] T. Pertsch, P. Dannberg, W. Elflein, et al. *Optical Bloch oscillations in temperature tuned waveguide arrays.* Physical Review Letters, 83 (23), 4752–4755 (1999).

[55] R. Morandotti, U. Peschel, J. S. Aitchison, et al. *Experimental observation of linear and nonlinear optical bloch oscillations.* Physical Review Letters, 83 (23), 4756–4759 (1999).

[56] P. Drude. *Zur Elektronentheorie der Metalle.* Annalen der Physik, 306 (3), 566–613 (1900).

[57] M. Dressel and M. Scheffler. *Verifying the Drude response.* Annalen der Physik, 15 (7-8), 535–544 (2006).

[58] N. S. Shcheblanov, E. P. Silaeva, and T. E. Itina. *Electronic excitation and relaxation processes in wide band gap dielectric materials in the transition region of the Keldysh parameter.* Applied Surface Science, 258 (23), 9417–9420 (2012).

[59] A. P. Pati, I. S. Wahyutama, and A. N. Pfeiffer. *Subcycle-resolved probe retardation in strong-field pumped dielectrics.* Nature Communications, 6 (2015).

[60] W. Kuehn, P. Gaal, K. Reimann, et al. *Coherent ballistic motion of electrons in a periodic potential.* Physical Review Letters, 104 (14), 146602 (2010).

[61] M. Hohenleutner, F. Langer, O. Schubert, et al. *Real-time observation of interfering crystal electrons in high-harmonic generation.* Nature, 523 (7562), 572–575 (2015).

[62] T. Paasch-Colberg, A. Schiffrin, N. Karpowicz, et al. *Solid-state light-phase detector.* Nature Photonics, 8 (3), 214–218 (2014).

[63] T. Paasch-Colberg, R. Kienberger, P. A. Feulner, et al. *Ultrafast, optical-field-induced currents in solid-state materials.* Ph.D. thesis, Universitätsbibliothek der TU München, München (2014).

[64] V. S. Yakovlev, M. Ivanov, and F. Krausz. *Enhanced phase-matching for generation of soft X-ray harmonics and attosecond pulses in atomic gases.* Optics Express, 15 (23), 15351–15364 (2007).

[65] S. Y. Kruchinin, M. Korbman, and V. S. Yakovlev. *Theory of strong-field injection and control of photocurrent in dielectrics and wide band gap semiconductors.* Physical Review B, 87 (11), 115201 (2013).

[66] P. Földi, M. G. Benedict, and V. S. Yakovlev. *The effect of dynamical Bloch oscillations on optical-field-induced current in a wide-gap dielectric.* New Journal of Physics, 15 (6), 063019 (2013).

[67] R. Atanasov, A. Haché, J. L. P. Hughes, et al. *Coherent control of photocurrent generation in bulk semiconductors.* Physical Review Letters, 76 (10), 1703–1706 (1996).

[68] A. Haché, Y. Kostoulas, R. Atanasov, et al. *Observation of coherently controlled photocurrent in unbiased, bulk GaAs.* Physical Review Letters, 78 (2), 306–309 (1997).

[69] A. Haché, J. Sipe, and H. van Driel. *Quantum interference control of electrical currents in GaAs.* IEEE Journal of Quantum Electronics, 34 (7), 1144–1154 (1998).

[70] L. Costa, M. Betz, M. Spasenović, et al. *All-optical injection of ballistic electrical currents in unbiased silicon.* Nature Physics, 3 (9), 632–635 (2007).

[71] I. Franco, M. Shapiro, and P. Brumer. *Robust ultrafast currents in molecular wires through Stark shifts.* Physical Review Letters, 99 (12), 126802 (2007).

[72] L. Prechtel, L. Song, S. Manus, et al. *Time-resolved picosecond photocurrents in contacted carbon nanotubes.* Nano Letters, 11 (1), 269–272 (2011).

[73] L. Prechtel, L. Song, D. Schuh, et al. *Time-resolved ultrafast photocurrents and terahertz generation in freely suspended graphene.* Nature Communications, 3 (2012).

[74] M. Durach, A. Rusina, M. F. Kling, et al. *Metallization of nanofilms in strong adiabatic electric fields.* Physical Review Letters, 105 (8), 086803 (2010).

[75] M. Durach, A. Rusina, M. F. Kling, et al. *Predicted ultrafast dynamic metallization of dielectric nanofilms by strong single-cycle optical fields.* Physical Review Letters, 107 (8), 086602 (2011).

[76] G. H. Wannier. *Wave functions and effective hamiltonian for Bloch electrons in an electric field.* Physical Review, 117 (2), 432–439 (1960).

[77] G. H. Wannier. *Dynamics of band electrons in electric and magnetic fields.* Reviews of Modern Physics, 34 (4), 645–655 (1962).

[78] A. Schiffrin, T. Paasch-Colberg, N. Karpowicz, et al. *Addendum: Optical-field-induced current in dielectrics.* Nature, 507 (7492), 386–387 (2014).

[79] E. M. L. Bothschafter. *Femtosecond and attosecond electron dynamics in semiconductors and dielectrics.* Ph.D. thesis, Technische Universität München (2014).

[80] M. Uiberacker, T. Uphues, M. Schultze, et al. *Attosecond real-time observation of electron tunnelling in atoms.* Nature, 446 (7136), 627–632 (2007).

[81] M. Yamanishi. *Field-induced optical nonlinearity due to virtual transitions in semiconductor quantum well structures.* Physical Review Letters, 59 (9), 1014–1017 (1987).

[82] D. S. Chemla, D. A. B. Miller, and S. Schmitt-Rink. *Generation of ultrashort electrical pulses through screening by virtual populations in biased quantum wells.* Physical Review Letters, 59 (9), 1018–1021 (1987).

[83] E. Yablonovitch, J. P. Heritage, D. E. Aspnes, et al. *Virtual photoconductivity.* Physical Review Letters, 63 (9), 976–979 (1989).

[84] B. B. Hu, X.-C. Zhang, and D. H. Auston. *Terahertz radiation induced by subband-gap femtosecond optical excitation of GaAs.* Physical Review Letters, 67 (19), 2709–2712 (1991).

[85] G. Wachter, C. Lemell, J. Burgdörfer, et al. *Ab initio simulation of electrical currents induced by ultrafast laser excitation of dielectric materials.* Physical Review Letters, 113 (8), 087401 (2014).

[86] I. A. Walmsley and V. Wong. *Characterization of the electric field of ultrashort optical pulses.* JOSA B, 13 (11), 2453–2463 (1996).

[87] D. Kane and R. Trebino. *Characterization of arbitrary femtosecond pulses using frequency-resolved optical gating.* IEEE Journal of Quantum Electronics, 29 (2), 571–579 (1993).

[88] H. Stark. *Image Recovery: Theory and Application.* Elsevier (1987).

[89] C. Iaconis and I. A. Walmsley. *Spectral phase interferometry for direct electric-field reconstruction of ultrashort optical pulses.* Optics Letters, 23 (10), 792–794 (1998).

[90] Y. Nomura, H. Shirai, and T. Fuji. *Frequency-resolved optical gating capable of carrier-envelope phase determination.* Nature Communications, 4 (2013).

[91] R. Holzwarth, T. Udem, T. W. Hänsch, et al. *Optical frequency synthesizer for precision spectroscopy.* Physical Review Letters, 85 (11), 2264–2267 (2000).

[92] D. J. Jones, S. A. Diddams, J. K. Ranka, et al. *Carrier-envelope phase control of femtosecond mode-locked lasers and direct optical frequency synthesis.* Science, 288 (5466), 635–639 (2000).

[93] S. T. Cundiff and J. Ye. *Colloquium: Femtosecond optical frequency combs.* Reviews of Modern Physics, 75 (1), 325–342 (2003).

[94] A. Baltuška, T. Udem, M. Uiberacker, et al. *Attosecond control of electronic processes by intense light fields.* Nature, 421 (6923), 611–615 (2003).

[95] P. Roos, Q. Quraishi, S. Cundiff, et al. *Characterization of quantum interference control of injected currents in LT-GaAs for carrier-envelope phase measurements.* Optics Express, 11 (17), 2081–2090 (2003).

[96] K. Osvay, M. Görbe, C. Grebing, et al. *Bandwidth-independent linear method for detection of the carrier-envelope offset phase.* Optics Letters, 32 (21), 3095–3097 (2007).

[97] P. Agostini, F. Fabre, G. Mainfray, et al. *Free-free transitions following six-photon ionization of xenon atoms.* Physical Review Letters, 42 (17), 1127–1130 (1979).

[98] G. G. Paulus, F. Lindner, H. Walther, et al. *Measurement of the phase of few-cycle laser pulses.* Physical Review Letters, 91 (25), 253004 (2003).

[99] T. Wittmann, B. Horvath, W. Helml, et al. *Single-shot carrier-envelope phase measurement of few-cycle laser pulses.* Nature Physics, 5 (5), 357–362 (2009).

[100] C. A. Haworth, L. E. Chipperfield, J. S. Robinson, et al. *Half-cycle cutoffs in harmonic spectra and robust carrier-envelope phase retrieval.* Nature Physics, 3 (1), 52–57 (2007).

[101] T. Popmintchev, M.-C. Chen, D. Popmintchev, et al. *Bright coherent ultrahigh harmonics in the keV x-ray regime from mid-infrared femtosecond lasers.* Science, 336 (6086), 1287–1291 (2012).

[102] T. W. B. Kibble. *Refraction of electron beams by intense electromagnetic waves.* Physical Review Letters, 16 (23), 1054–1056 (1966).

[103] M. Lewenstein, P. Balcou, M. Y. Ivanov, et al. *Theory of high-harmonic generation by low-frequency laser fields.* Physical Review A, 49 (3), 2117–2132 (1994).

[104] P. B. Corkum. *Plasma perspective on strong field multiphoton ionization.* Physical Review Letters, 71 (13), 1994–1997 (1993).

[105] G. Sansone, E. Benedetti, F. Calegari, et al. *Isolated single-cycle attosecond pulses.* Science, 314 (5798), 443–446 (2006).

[106] M. J. Abel, T. Pfeifer, P. M. Nagel, et al. *Isolated attosecond pulses from ionization gating of high-harmonic emission.* Chemical Physics, 366 (1-3), 9–14 (2009).

[107] H. Vincenti and F. Quéré. *Attosecond lighthouses: How to use spatiotemporally coupled light fields to generate isolated attosecond pulses.* Physical Review Letters, 108 (11), 113904 (2012).

[108] J. Itatani, F. Quéré, G. L. Yudin, et al. *Attosecond streak camera.* Physical Review Letters, 88 (17), 173903 (2002).

[109] J. Gagnon, E. Goulielmakis, and V. S. Yakovlev. *The accurate FROG characterization of attosecond pulses from streaking measurements.* Applied Physics B, 92 (1), 25–32 (2008).

[110] E. Goulielmakis, M. Schultze, M. Hofstetter, et al. *Single-cycle nonlinear optics.* Science, 320 (5883), 1614–1617 (2008).

[111] A. Wirth, M. T. Hassan, I. Grguraš, et al. *Synthesized light transients.* Science, 334 (6053), 195–200 (2011).

[112] F. Ferrari, F. Calegari, M. Lucchini, et al. *High-energy isolated attosecond pulses generated by above-saturation few-cycle fields.* Nature Photonics, 4 (12), 875–879 (2010).

[113] Z. Chang. *Fundamentals of Attosecond Optics.* CRC Press (2011).

[114] M. Hentschel, R. Kienberger, C. Spielmann, et al. *Attosecond metrology.* Nature, 414 (6863), 509–513 (2001).

[115] M. B. Gaarde, M. Murakami, and R. Kienberger. *Spatial separation of large dynamical blueshift and harmonic generation.* Physical Review A, 74 (5), 053401 (2006).

[116] K. T. Kim, C. Zhang, A. D. Shiner, et al. *Petahertz optical oscilloscope.* Nature Photonics, 7 (12), 958–962 (2013).

[117] F. Lücking, A. Assion, A. Apolonski, et al. *Long-term carrier-envelope-phase-stable few-cycle pulses by use of the feed-forward method.* Optics letters, 37 (11), 2076–2078 (2012).

[118] A. Dubietis, G. Jonušauskas, and A. Piskarskas. *Powerful femtosecond pulse generation by chirped and stretched pulse parametric amplification in BBO crystal.* Optics Communications, 88 (4), 437–440 (1992).

[119] I. Ross, P. Matousek, M. Towrie, et al. *The prospects for ultrashort pulse duration and ultrahigh intensity using optical parametric chirped pulse amplifiers.* Optics Communications, 144 (1–3), 125–133 (1997).

[120] Y. Deng, A. Schwarz, H. Fattahi, et al. *Carrier-envelope-phase-stable, 1.2 mJ, 1.5 cycle laser pulses at 2.1 μm.* Optics Letters, 37 (23), 4973–4975 (2012).

[121] A. Schwarz, M. Ueffing, Y. Deng, et al. *Active stabilization for optically synchronized optical parametric chirped pulse amplification.* Optics Express, 20 (5), 5557–5565 (2012).

[122] H. Fattahi, A. Schwarz, S. Keiber, et al. *Efficient, octave-spanning difference-frequency generation using few-cycle pulses in simple collinear geometry.* Optics Letters, 38 (20), 4216–4219 (2013).

[123] T. Metzger. *High-repetition-rate picosecond pump laser based on an Yb:YAG disk amplifier for optical parametric amplification.* Südwestdeutscher Verlag für Hochschulschriften, Saarbrücken (2010).

[124] H. Fattahi, A. Schwarz, X. T. Geng, et al. *Decoupling chaotic amplification and nonlinear phase in high-energy thin-disk amplifiers for stable OPCPA pumping.* Optics Express, 22 (25), 31440 (2014).

[125] H. Fattahi. *Third-generation femtosecond technology.* Ph.D. thesis, Ludwig-Maximilians-Universität München (2015).

[126] J. Dudley, X. Gu, L. Xu, et al. *Cross-correlation frequency resolved optical gating analysis of broadband continuum generation in photonic crystal fiber: simulations and experiments.* Optics Express, 10 (21), 1215–1221 (2002).

[127] P. Gaal, W. Kuehn, K. Reimann, et al. *Internal motions of a quasiparticle governing its ultrafast nonlinear response.* Nature, 450 (7173), 1210–1213 (2007).

[128] C. Kübler, H. Ehrke, R. Huber, et al. *Coherent structural dynamics and electronic correlations during an ultrafast insulator-to-metal phase transition in VO_2.* Physical Review Letters, 99 (11), 116401 (2007).

[129] C. Somma, K. Reimann, C. Flytzanis, et al. *High-field terahertz bulk photovoltaic effect in lithium niobate.* Physical Review Letters, 112 (14), 146602 (2014).

[130] A. Pashkin, A. Sell, T. Kampfrath, et al. *Electric and magnetic terahertz nonlinearities resolved on the sub-cycle scale.* New Journal of Physics, 15 (6), 065003 (2013).

[131] R. Huber, F. Tauser, A. Brodschelm, et al. *How many-particle interactions develop after ultrafast excitation of an electron-hole plasma.* Nature, 414 (6861), 286–289 (2001).

[132] A. Pashkin, M. Porer, M. Beyer, et al. *Femtosecond response of quasiparticles and phonons in superconducting $YBa_2Cu_3O_{7-\delta}$ studied by wideband terahertz spectroscopy.* Physical Review Letters, 105 (6), 067001 (2010).

[133] J. Kröll, J. Darmo, S. S. Dhillon, et al. *Phase-resolved measurements of stimulated emission in a laser.* Nature, 449 (7163), 698–701 (2007).

[134] C. Riek, D. V. Seletskiy, A. S. Moskalenko, et al. *Direct sampling of electric-field vacuum fluctuations.* Science, 350 (6259), 420–423 (2015).

[135] E. Matsubara, M. Nagai, and M. Ashida. *Ultrabroadband coherent electric field from far infrared to 200 THz using air plasma induced by 10 fs pulses.* Applied Physics Letters, 101 (1), 011105 (2012).

[136] B. Wolter, M. G. Pullen, M. Baudisch, et al. *Strong-field physics with mid-IR fields.* Physical Review X, 5 (2), 021034 (2015).

[137] K. D. Schultz, C. I. Blaga, R. Chirla, et al. *Strong field physics with long wavelength lasers.* Journal of Modern Optics, 54 (7), 1075–1085 (2007).

[138] S. Keiber, S. Sederberg, A. Schwarz, et al. *Electro-optic sampling of near-infrared waveforms.* Nature Photonics, 10 (3), 159–162 (2016).

[139] O. Gayer, Z. Sacks, E. Galun, et al. *Temperature and wavelength dependent refractive index equations for MgO-doped congruent and stoichiometric LiNbO3.* Applied Physics B, 91 (2), 343–348 (2008).

[140] C. Shannon. *Communication in the presence of noise.* Proceedings of the IRE, 37 (1), 10–21 (1949).

[141] M. Porer, J.-M. Ménard, and R. Huber. *Shot noise reduced terahertz detection via spectrally postfiltered electro-optic sampling.* Optics Letters, 39 (8), 2435–2438 (2014).

[142] G. P. Agrawal. *Fiber optic communication systems*. Wiley series in microwave and optical engineering. Wiley, New York [u.a.], 3. ed. edition (2002).

[143] S. Lavender. *Practical handbook of remote sensing*. Environmental science. CRC Press, Boca Raton ; London ; New York (2016).

[144] D. H. Auston. *Picosecond optoelectronic switching and gating in silicon*. Applied Physics Letters, 26 (3), 101–103 (1975).

[145] G. Mourou, C. V. Stancampiano, A. Antonetti, et al. *Picosecond microwave pulses generated with a subpicosecond laser-driven semiconductor switch*. Applied Physics Letters, 39 (4), 295–296 (1981).

[146] D. H. Auston, K. P. Cheung, and P. R. Smith. *Picosecond photoconducting Hertzian dipoles*. Applied Physics Letters, 45 (3), 284–286 (1984).

[147] N. Katzenellenbogen and D. Grischkowsky. *Efficient generation of 380 fs pulses of THz radiation by ultrafast laser pulse excitation of a biased metal-semiconductor interface*. Applied Physics Letters, 58 (3), 222–224 (1991).

[148] G. Kurizki, M. Shapiro, and P. Brumer. *Phase-coherent control of photocurrent directionality in semiconductors*. Physical Review B, 39 (5), 3435–3437 (1989).

[149] B. Y. Zel'Dovich and A. N. Chudinov. *Interference of fields with frequencies ω and 2ω in external photoelectric effect*. Soviet Journal of Experimental and Theoretical Physics Letters, 50, 439 (1989).

[150] D. Côté, N. Laman, and H. M. van Driel. *Rectification and shift currents in GaAs*. Applied Physics Letters, 80 (6), 905–907 (2002).

[151] F. Schwierz and J. J. Liou. *RF transistors: Recent developments and roadmap toward terahertz applications*. Solid-State Electronics, 51 (8), 1079–1091 (2007).

[152] R. Lai, X. B. Mei, W. R. Deal, et al. *Sub 50 nm InP HEMT device with F_{max} greater than 1 THz*. In *Electron Devices Meeting, 2007. IEDM 2007. IEEE International*, pp. 609–611 (2007).

[153] J. Lee, W. S. Yun, and N. Park. *Rectifying the optical-field-induced current in dielectrics: Petahertz diode*. Physical Review Letters, 116 (5), 057401 (2016).

[154] R. Flitsch and S. I. Raider. *Electron mean escape depths from x-ray photoelectron spectra of thermally oxidized silicon dioxide films on silicon*. Journal of Vacuum Science & Technology, 12 (1), 305–308 (1975).

[155] M. V. Fischetti, D. J. DiMaria, L. Dori, et al. *Ballistic electron transport in thin silicon dioxide films*. Physical Review B, 35 (9), 4404–4415 (1987).

[156] P. Martin, S. Guizard, P. Daguzan, et al. *Subpicosecond study of carrier trapping dynamics in wide-band-gap crystals.* Physical Review B, 55 (9), 5799–5810 (1997).

[157] F. Quéré, S. Guizard, and P. Martin. *Time-resolved study of laser-induced breakdown in dielectrics.* EPL (Europhysics Letters), 56 (1), 138 (2001).

[158] Z. A. Weinberg, G. W. Rubloff, and E. Bassous. *Transmission, photoconductivity, and the experimental band gap of thermally grown SiO_2 films.* Physical Review B, 19 (6), 3107–3117 (1979).

[159] I. H. Malitson. *Interspecimen comparison of the refractive index of fused silica.* JOSA, 55 (10), 1205–1209 (1965).

[160] Schott AG. *Schott - Optisches Glas, Datenblätter* (2014).

[161] R. DeSalvo, A. Said, D. Hagan, et al. *Infrared to ultraviolet measurements of two-photon absorption and n_2 in wide bandgap solids.* IEEE Journal of Quantum Electronics, 32 (8), 1324–1333 (1996).

[162] H. H. Li. *Refractive index of alkaline earth halides and its wavelength and temperature derivatives.* Journal of Physical and Chemical Reference Data, 9 (1), 161–290 (1980).

[163] Korth GmbH. *Datasheet Bariumfluorid* (2015).

[164] G. W. Rubloff. *Far-ultraviolet reflectance spectra and the electronic structure of ionic crystals.* Physical Review B, 5 (2), 662–684 (1972).

[165] Korth GmbH. *Datasheet Calciumfluorid* (2015).

[166] U. Schönberger and F. Aryasetiawan. *Bulk and surface electronic structures of MgO.* Physical Review B, 52 (12), 8788–8793 (1995).

[167] R. E. Stephens and I. H. Malitson. *Index of refraction of magnesium oxide.* Journal of Research of the National Bureau of Standards, 49 (4), 249–252 (1952).

[168] Mateck GmbH. *Datasheet Magnesiumoxid* (2015).

[169] Femto Messtechnik GmbH. *Datasheet: Variable gain low noise current amplifier DLPCA-200* (2015).

[170] J. Krüger, D. Dufft, R. Koter, et al. *Femtosecond laser-induced damage of gold films.* Applied Surface Science, 253 (19), 7815–7819 (2007).

[171] A. K. Varshneya. *Fundamentals of Inorganic Glasses.* Elsevier (2013).

[172] X. Li, T. Abe, and M. Esashi. *Deep reactive ion etching of Pyrex glass using SF6 plasma.* Sensors and Actuators A: Physical, 87 (3), 139–145 (2001).

[173] P. G. Huggard, C. J. Shaw, J. A. Cluff, et al. *Polarization-dependent efficiency of photoconducting THz transmitters and receivers.* Applied Physics Letters, 72 (17), 2069–2071 (1998).

[174] S. E. Ralph and D. Grischkowsky. *Trap-enhanced electric fields in semi-insulators: The role of electrical and optical carrier injection.* Applied Physics Letters, 59 (16), 1972–1974 (1991).

[175] S. Keiber, T. Paasch-Colberg, A. Schwarz, et al. *Investigation of laser-induced currents in large-band-gap dielectrics.* In K. Yamanouchi, S. Cundiff, R. d. Vivie-Riedle, et al. (Editors), *Ultrafast Phenomena XIX*, number 162 in Springer Proceedings in Physics, pp. 237–240. Springer International Publishing (2015).

[176] Y. Ma and M. Rohlfing. *Quasiparticle band structure and optical spectrum of CaF_2.* Physical Review B, 75 (20), 205114 (2007).

[177] E. Cadelano, J. Furthmüller, G. Cappellini, et al. *One- and two-particle effects in the electronic and optical spectra of barium fluoride.* Journal of Physics: Condensed Matter, 26 (12), 125501 (2014).

[178] P. Blaha, K. Schwarz, G. K. H. Madsen, et al. *WIEN2K, An Augmented Plane Wave + Local Orbitals Program for Calculating Crystal Properties.* Karlheinz Schwarz, Techn. Universität Wien, Austria (2001).

[179] S. E. Irvine and A. Y. Elezzabi. *Ponderomotive electron acceleration using surface plasmon waves excited with femtosecond laser pulses.* Applied Physics Letters, 86 (26), 264102 (2005).

[180] R. Bormann, M. Gulde, A. Weismann, et al. *Tip-enhanced strong-field photoemission.* Physical Review Letters, 105 (14), 147601 (2010).

[181] H. Shi, R. I. Eglitis, and G. Borstel. *Ab initio calculations of the BaF_2 bulk and surface F centres.* Journal of Physics: Condensed Matter, 18 (35), 8367 (2006).

[182] A. Nahata and T. F. Heinz. *Detection of freely propagating terahertz radiation by use of optical second-harmonic generation.* Optics Letters, 23 (1), 67–69 (1998).

[183] C. Manzoni, O. D. Mücke, G. Cirmi, et al. *Coherent pulse synthesis: towards sub-cycle optical waveforms.* Laser & Photonics Reviews, 9 (2), 129–171 (2015).

[184] S. Thunich, C. Ruppert, A. W. Holleitner, et al. *Field-resolved characterization of femtosecond electromagnetic pulses with 400 THz bandwidth.* Optics Letters, 36 (10), 1791 (2011).

[185] L. V. Keldysh and others. *Ionization in the field of a strong electromagnetic wave.* Sov. Phys. JETP, 20 (5), 1307–1314 (1965).

[186] W. Franz. *Einfluss eines elektrischen Feldes auf eine optische Absorptionskante.* Zeitschrift für Naturforschung A, 13 (6), 484–489 (2014).

[187] L. V. Keldysh. *Behavior of non-metallic crystals in strong electric fields.* Soviet Journal of Experimental and Theoretical Physics, 6, 763 (1958).

[188] P. Audebert, P. Daguzan, A. Dos Santos, et al. *Space-time observation of an electron gas in SiO_2.* Physical Review Letters, 73 (14), 1990–1993 (1994).

[189] S. Guizard, P. Martin, G. Petite, et al. *Time-resolved study of laser-induced colour centres in SiO_2.* Journal of Physics: Condensed Matter, 8 (9), 1281 (1996).

[190] R. Chang, S. Potnis, R. Ramos, et al. *Observing the Onset of Effective Mass.* Physical Review Letters, 112 (17), 170404 (2014).

[191] J. Tate, T. Auguste, H. G. Muller, et al. *Scaling of wave-packet dynamics in an intense midinfrared field.* Physical Review Letters, 98 (1), 013901 (2007).

[192] S. L. Cousin, F. Silva, S. Teichmann, et al. *High-flux table-top soft x-ray source driven by sub-2-cycle, CEP stable, 1.85-μm 1-kHz pulses for carbon K-edge spectroscopy.* Optics Letters, 39 (18), 5383–5386 (2014).

[193] M. Fieß, M. Schultze, E. Goulielmakis, et al. *Versatile apparatus for attosecond metrology and spectroscopy.* Review of Scientific Instruments, 81 (9), 093103–093103–8 (2010).

[194] L. Mach. *Ueber einen Interferenzrefraktor.* Zeitschrift für Instrumentenkunde, 11, 89–93 (1892).

[195] L. Zehnder. *Ein neuer Interferenzrefraktor.* Zeitschrift für Instrumentenkunde, 11, 275–285 (1891).

Acknowledgements

I want to use this opportunity to express my gratitude to all the friends and colleagues who have in one way or the other contributed to this dissertation and made my time at MPQ an unforgettable experience. The LAP team is too big to name everyone so this is my short list. My special thanks go to...

- Ferenc Krausz for giving me the opportunity to work with the LAP group and its great infrastructure, for his scientific vision and his unshakable belief that physics will cooperate.
- Nick Karpowicz for being a great boss, brilliant scientist, laser tamer, simulation magician, and in short the best team leader a PhD student could wish for.
- All the past, present, and honorary FENNEC group members I have had the pleasure to work with: Olga Raszkovskaya, Shawn Sederberg, Clemens Jakubeit, Tim Paasch-Colberg, Alexander Schwarz, and Hanieh Fattahi. Thanks for the great team spirit, mutual support, and fun times.
- Our temporary team members as well as collaborators in sample fabrication and theory: Amelia Wigianto, Francisco Nunes, Tailin Lin, Julian Harms, Peter Dombi, Viktoria Csajbok, Vlad Yakovlev, and Stanislav Kruchinin. I particularly appreciate the efforts of Özge Sağlam into fabricating our beautiful lithography samples.
- The whole AS/clean room team: Marcus Ossiander, Annka Sommer, Johann Riemensberger, Ayman Akil, Tobias Latka, Martin Schultze, Reinhard Kienberger, ... Kudos to keeping up the good spirit even when facing the daily madness in the lab.
- The coating team around Vladimir Pervak, Elena Fedulova, and Michael Trubetskov for helping us to keep our pulses short and our samples contacted.
- Everyone who ever helped out with replacements and advice in case of broken lab equipment and missing diagnostics, especially to Moritz Ueffing, Alexander Kessel, and Oleg Pronin.
- Our technicians and the MPQ workshop employees for their competent support especially during the planning and construction of AS4: Harald Haas, Anton Horn, Tobias Kleinhenz, Alois Böswald, Johannes Wulz as well as Michael Rogg and his team.

- The administrative staff who are pulling the strings behind the scenes, especially to the one and only Mrs. Wild.
- Jörn Wilhelm for making me smile, having my back, and being the awesomest boyfriend in the world.
- And finally: Danke Mama, ich vermisse dich.